TU Delft

Delft University of Technology

Induced superconductivity in antimony-based two-dimensional electron gases

Möhle, C.M.

DOI
10.4233/uuid:c4d83571-9445-44b7-b495-5d18ca66ef4f

Publication date
2023

Document Version
Final published version

Citation (APA)
Möhle, C. M. (2023). *Induced superconductivity in antimony-based two-dimensional electron gases*. [Dissertation (TU Delft), Delft University of Technology]. https://doi.org/10.4233/uuid:c4d83571-9445-44b7-b495-5d18ca66ef4f

Important note
To cite this publication, please use the final published version (if applicable).
Please check the document version above.

Copyright
Other than for strictly personal use, it is not permitted to download, forward or distribute the text or part of it, without the consent of the author(s) and/or copyright holder(s), unless the work is under an open content license such as Creative Commons.

Takedown policy
Please contact us and provide details if you believe this document breaches copyrights.
We will remove access to the work immediately and investigate your claim.

This work is downloaded from Delft University of Technology.
For technical reasons the number of authors shown on this cover page is limited to a maximum of 10.

INDUCED SUPERCONDUCTIVITY IN ANTIMONY-BASED TWO-DIMENSIONAL ELECTRON GASES

INDUCED SUPERCONDUCTIVITY IN ANTIMONY-BASED TWO-DIMENSIONAL ELECTRON GASES

Proefschrift

ter verkrijging van de graad van doctor
aan de Technische Universiteit Delft,
op gezag van de Rector Magnificus prof. dr. ir. T.H.J.J. van der Hagen,
voorzitter van het College voor Promoties,
in het openbaar te verdedigen op maandag 9 januari 2023 om 10:00 uur

door

Christian Mario MÖHLE

Master of Science in Physcis, Lund University, Sweden
born in Münster, Germany.

Dit proefschrift is goedgekeurd door de

promotor: Prof. dr. ir. L. P. Kouwenhoven
copromotor: Dr. S. Goswami

Samenstelling promotiecommissie:

Rector Magnificus,	voorzitter
Prof. dr. ir. L.P. Kouwenhoven,	Technische Universiteit Delft, promotor
Dr. S. Goswami,	Technische Universiteit Delft, copromotor

Onafhankelijke leden:

Prof. dr. Y.V. Nazarov,	Technische Universiteit Delft
Prof. dr. ir. L.M.K. Vandersypen,	Technische Universiteit Delft
Dr. T. van der Sar,	Technische Universiteit Delft
Prof. dr. K. Ensslin,	ETH Zürich, Zwitserland
Prof. J. Shabani,	New York University, Verenigde Staten van Amerika

Keywords: Two-dimensional electron gases, planar Josephson junctions, mesoscopic superconductivity
Printed by: Gildeprint
Cover: SQUID in a squid. Design by Anne Mulder.

Copyright © 2022 by C. M. Möhle

Casimir PhD Series, Delft-Leiden 2023-01

ISBN 978-90-8593-549-0

An electronic version of this dissertation is available at
`http://repository.tudelft.nl/`.

Contents

SUMMARY

Majorana zero modes (MZMs) are a topic of intense research as they constitute the main building block of topological qubits - a qubit type with potentially enhanced coherence time. A promising way to create these quantum states is to couple a one-dimensional (1D) semiconducting segment with spin-orbit interaction to a superconductor, in the presence of an external magnetic field. Growing the active semiconductor as a 2D layer and creating 1D structures by top-down processing might allow to realize complex multi-qubit devices in the future. This thesis explores antimony-based two-dimensional electron gases (2DEGs), known for their favorable material properties, as platforms for topological superconductivity.

First, the theoretical background is presented with a focus on Josephson junctions (JJs) and realizing phase-tunable MZMs therein. Besides, we introduce the materials that are used in this thesis and describe the main fabrication challenges for each platform.

In the first experimental chapter, we create JJs in high-quality InSb 2DEGs and observe supercurrents over micrometer-scale lengths. Under the application of an in-plane magnetic field, we observe revivals of the supercurrent, associated with $0-\pi$ transitions. We demonstrate that these transitions are tunable with the device length and the electron density, in quantitative agreement with the theory of ballistic π-JJs.

Then we switch material systems and study InSbAs surface 2DEGs with in-situ grown Al as the superconductor. We show that the bare semiconductor has strong spin-orbit coupling, a large g-factor and a small effective mass. Moreover, the clean semiconductor-superconductor interface leads to a hard induced gap in the semiconductor. Exploiting the flexibility of this hybrid material system, we realize three different device geometries that can be used to create MZMs.

The next chapter focuses on tunneling spectroscopy measurements at both ends of phase-biased JJs made in InSbAs/Al 2DEGs. The spectroscopy maps obtained from the two sides are strikingly different, consistent with measuring localized Andreev bound states (ABSs) in the vicinity of the respective tunnel barrier, taking into account the effect of the local superconducting phase difference that has equal magnitude but opposite sign at the two ends. The resulting superconducting phase shifts allow to estimate the relative positions of ABSs in the junctions.

In the last experimental chapter, we complement local spectroscopy measurements on phase-biased JJs with non-local conductance measurements. At finite in-plane magnetic fields, we observe zero-bias peaks in local spectroscopy (typically not end-to-end correlated), but find no clear evidence of a gap re-opening in the nonlocal conductances.

We conclude this thesis by a summary and discussion of the results. Moreover, we discuss optimizations for the material stack and provide ideas for future experiments that can be carried with the already existing InSbAs/Al 2DEGs.

SAMENVATTING

Majorana zero modes (MZM's) zijn een onderwerp van intensief onderzoek, aangezien ze de belangrijkste bouwsteen vormen van topologische qubits – een qubittype met een potentieel verbeterde coherentietijd. Een veelbelovende manier om deze kwantumtoestanden te creëren is door een eendimensionaal (1D) halfgeleidend segment met spin-baan interactie te koppelen aan een supergeleider, in de aanwezigheid van een extern magnetisch veld. Door de actieve halfgeleider als een 2D-laag te laten groeien en 1D-structuren te creëren door top-down bewerking kunnen in de toekomst mogelijk complexe multi-qubit-apparaten worden gerealiseerd. Dit proefschrift onderzoekt op antimoon gebaseerde tweedimensionale elektronengassen (2DEG's), bekend om hun gunstige materiaaleigenschappen, als platforms voor topologische supergeleiding.

Eerst wordt de theoretische achtergrond gepresenteerd met een focus op Josephson-juncties (JJ's) en het realiseren van in fase afstembare MZM's daarin. Daarnaast introduceren we de materialen die in dit proefschrift worden gebruikt en beschrijven we de belangrijkste fabricage-uitdagingen voor elk platform.

In het eerste experimentele hoofdstuk creëren we JJ's in InSb 2DEG's van hoge kwaliteit en observeren we superstromen over lengten op micrometerschaal. Als een magneetveld wordt aangelegd in het vlak zien we herstel van de superstroom, geassocieerd met $0-\pi$-overgangen. We laten zien dat deze overgangen afstembaar zijn met de apparaatlengte en de elektronendichtheid, in kwantitatieve overeenstemming met de theorie van ballistische π-JJ's.

Vervolgens veranderen we van materiaalsysteem en bestuderen we InSbAs-oppervlakte-2DEG's met in-situ gegroeid Al als supergeleider. We laten zien dat de halfgeleider een sterke spin-baan koppeling heeft, een grote g-factor en een kleine effectieve massa. Bovendien leidt de schone halfgeleider-supergeleider-interface tot een harde geïnduceerde energiekloof in de halfgeleider. Door gebruik te maken van de flexibiliteit van dit hybride materiaalsysteem realiseren we drie verschillende apparaatgeometrieën die kunnen worden gebruikt om MZM's te maken.

Het volgende hoofdstuk richt zich op tunneling-spectroscopiemetingen aan beide uiteinden van JJ's met een fase bias gemaakt in InSbAs/Al 2DEG's. De spectroscopiekaarten zijn aan beide zijden opvallend verschillend, consistent met het meten van gelokaliseerde Andreev-gebonden toestanden (ABS's) in de buurt van de respectieve tunnelbarrière, en rekening houdend met het effect van het lokale supergeleidende faseverschil. De resulterende supergeleidende faseverschuivingen maken het mogelijk om de relatieve posities van ABS'en in de juncties in te schatten.

In het laatste experimentele hoofdstuk vullen we lokale spectroscopiemetingen op JJ's met een fase bias aan met niet-lokale geleidingsmetingen. Bij eindige in het vlak uitgelijnde magnetische velden nemen we nul-bias-pieken waar in lokale spectroscopie (meestal niet end-to-end gecorreleerd), maar we vinden geen duidelijk bewijs van een

opening in de niet-lokale geleidingen.

We sluiten dit proefschrift af met een samenvatting en bespreking van de resultaten. Bovendien bespreken we optimalisaties voor de materiaalstapel en geven we ideeën voor toekomstige experimenten die kunnen worden uitgevoerd met de reeds bestaande InSbAs/Al 2DEG's.

1

INTRODUCTION

1

Digital electronics have transformed our lives. Thanks to devices such as laptops and smartphones many people are connected to each other and information is available non-stop. The fundamental building block of these devices is a transistor that can be thought of as a switch being in either the on or off state. This allows one to encode a classical bit of information. Shrinking the size of the transistors has made it possible to incorporate an increasing number of them in integrated circuits, boosting the performance of the electronic devices. As a matter of fact, the scaling followed a prediction from Gordon Moore originally made in 1965 and adjusted in 1975, stating that the number of transistors in an integrated circuit would double roughly every two years ('Moore's Law') [1, 2]. However, as the transistor dimensions continue to shrink (now approaching the atomic scale), the miniaturization becomes increasingly more difficult and expensive. In fact, the advances have slowed somewhat below the pace predicted by Moore's Law since about 2010, and an end of the scaling is clearly in sight [3, 4]. Despite the enormous progress, currently the even most powerful supercomputers in the world are unable to solve problems with a very high degree of complexity, for example modeling the behavior of individual atoms in a molecule. Therefore, the end of the transistor scaling is an unsatisfactory situation.

Numerous ideas exist to continue the performance scaling in the absence of Moore's Law. One approach is to harness the effects of quantum mechanics and to build a quantum computer. These machines are expected to be capable of solving certain complex problems that are intractable for classical computers [5–7]. Quantum computers use quantum bits (qubits) to store and process information [8]. As opposed to their classical counterparts, qubits can be in a superposition of the two basis states (on and off for the transistor). They can be implemented in a two-level quantum mechanical system such as the spin of an electron in a semiconductor or using two discrete energy levels in a superconducting circuit. One key challenge is that these qubits are susceptible to noise from the environment (charge or magnetic noise), leading to unwanted interactions and ultimately to a loss of the stored quantum information. This might be prevented by encoding the information redundantly in a block of multiple qubits, called a logical qubit. In this way, errors can be detected and corrected, provided certain conditions are fulfilled [9–11]. Progress in quantum error correction has sparked hope to realize a fault-tolerant universal quantum computer, but it comes at the price of a significantly increased qubit count [12, 13]. The exact overhead depends on the quality of the hardware and the algorithm to be run, but a recent estimate puts the number of physical qubits needed to realize a logical qubit above 1000 (with more than 20 million physical qubits required in total) [13].

An alternative approach attempting to prevent this large overhead is to build qubits that are intrinsically protected against noise. This is the idea behind the topological qubit, where quantum information is stored in pairs of spatially separated zero-energy states, so-called Majorana zero-modes (MZMs). MZMs occur naturally in p-wave superconductors, but since the existence of these in nature is unclear, they have to be engineered artificially. This can be done by coupling a one-dimensional semiconducting segment with spin-orbit interaction to a regular s-wave superconductor (abundant in nature),

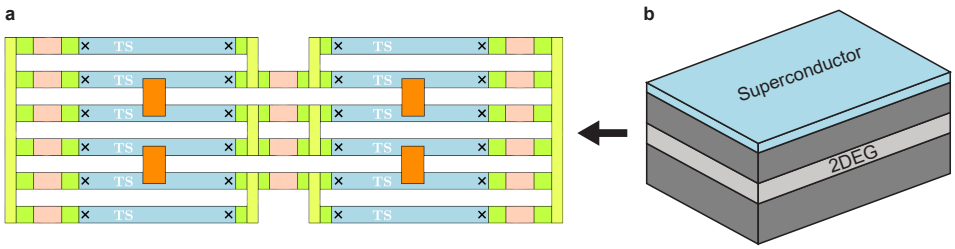

Figure 1.1: **a,** Proposal for a multi-qubit architecture consisting of numerous topological segments (TS). Each TS hosts two Majorana zero-modes, denoted by the black crosses. Figure adapted from [19]. **b,** Schematic of a two-dimensional electron gas (2DEG) coupled to a superconductor, which can be used to fabricate the multi-qubit device on the left.

in the presence of an external magnetic field [14, 15]. For this it is important that the semiconductor is nearly defect-free, also having strong spin-orbit coupling and a large effective g-factor, and that the semiconductor-superconductor interface is as clean as possible. The first platform that has been explored for proof-of-principle experiments were semiconducting-superconducting hybrid nanowires (thin, quasi-1D conduction channels). While important insights have been gained, the ability to create MZMs in these systems has not been demonstrated conclusively in experiments [16–18]. Moreover, realizing multi-qubit architectures requires complex devices with numerous well-aligned topological segments (see left panel in Fig. 1.1). Achieving this with single hybrid nanowires will be extremely challenging. Clearly, a more flexible and scalable platform is needed.

One such platform is a two-dimensional electron gas (2DEG), realized in a semiconductor heterostructure, that is coupled to a superconductor (see schematic in the right panel of Fig. 1.1). Arbitrary shapes can be patterned into the hybrid 2DEG by top-down processing. 2DEGs not only hold promise to realize multiple-qubit structures in the future, but can be used already now to explore alternative and potentially better device geometries to create MZMs. Among these are planar Josephson junctions (JJs), where a thin strip of superconductor is removed in between two wider superconducting banks [20, 21]. The phase difference between the two superconductors is expected to serve as an additional knob to tune into and out of the topological regime, and to create MZMs at a lower external magnetic field, which is beneficial for the operation of the MZM device. The front cover presents an artistic illustration of a planar phase-tunable JJ.

This thesis aims to explore new hybrid 2DEG platforms with improved material properties for the development of topological qubits in the future. A special emphasis is placed on investigating planar Josephson junctions as a potential candidate for the creation of MZMs.

Chapter 2 introduces the theoretical concepts that are relevant for the experiments, with

a focus on creating phase-tunable MZMs in planar Josephson junction. The 2DEG materials that are used in this thesis (InSb and InSbAs) are described in chapter 3, also explaining the main challenges for the device fabrication when using these materials. Chapter 4 explores planar JJs in InSb 2DEGs coupled to the ex-situ deposited superconductor NbTiN. In particular, we study the supercurrent through these junctions in the presence of an in-plane magnetic field. In chapter 5 we introduce InSbAs 2DEGs coupled to the in-situ grown superconductor Al, and realize prototypical MZM devices in this material system. Among these are planar phase-biased JJs, which are studied in detail in chapter 6, focusing on tunneling spectroscopy measurements at both ends of the junctions. In chapter 7 we additionally measure the nonlocal conductance in these junctions, which is expected to give information about the bulk of the junctions. Finally, in chapter 8, we summarize the important findings and present an outlook for future experiments.

REFERENCES

1. Moore, G. E. Cramming More Components onto Integrated Circuits. *Electronics* **38,** 48–53 (1965).
2. Moore, G. E. et al. *Progress in digital integrated electronics* in *Electron devices meeting* **21** (1975), 11–13.
3. Khan, H. N., Hounshell, D. A. & Fuchs, E. R. H. Science and research policy at the end of Moore's law. *Nature Electronics* **1,** 14–21 (2018).
4. Leiserson, C. E., Thompson, N. C., Emer, J. S., Kuszmaul, B. C., Lampson, B. W., Sanchez, D. & Schardl, T. B. There's plenty of room at the Top: What will drive computer performance after Moore's law? *Science* **368,** eaam9744 (2020).
5. Grover, L. K. Quantum Mechanics Helps in Searching for a Needle in a Haystack. *Phys. Rev. Lett.* **79,** 325–328 (1997).
6. Shor, P. W. Polynomial-Time Algorithms for Prime Factorization and Discrete Logarithms on a Quantum Computer. *SIAM Review* **41,** 303–332 (1999).
7. Harrow, A. W. & Montanaro, A. Quantum computational supremacy. *Nature* **549,** 203–209 (2017).
8. Nielsen, M. A. & Chuang, I. L. *Quantum Computation and Quantum Information: 10th Anniversary Edition* (Cambridge University Press, 2010).
9. Shor, P. W. Scheme for reducing decoherence in quantum computer memory. *Phys. Rev. A* **52,** R2493–R2496 (1995).
10. Steane, A. M. Error Correcting Codes in Quantum Theory. *Phys. Rev. Lett.* **77,** 793–797 (1996).
11. Gottesman, D. *An introduction to quantum error correction* (Proceedings of Symposia in Applied Mathematics, 2002).
12. Preskill, J. Quantum Computing in the NISQ era and beyond. *Quantum* **2,** 79 (2018).
13. Preskill, J. Quantum computing 40 years later. `https://arxiv.org/abs/2106.10522` (2021).
14. Lutchyn, R. M., Sau, J. D. & Das Sarma, S. Majorana Fermions and a Topological Phase Transition in Semiconductor-Superconductor Heterostructures. *Phys. Rev. Lett.* **105,** 077001 (2010).
15. Oreg, Y., Refael, G. & von Oppen, F. Helical Liquids and Majorana Bound States in Quantum Wires. *Phys. Rev. Lett.* **105,** 177002 (2010).
16. Aguado, R. Majorana quasiparticles in condensed matter. *La Rivista del Nuovo Cimento* **40,** 523–593 (2017).

17. Lutchyn, R. M., Bakkers, E. P. A. M., Kouwenhoven, L. P., Krogstrup, P., Marcus, C. M. & Oreg, Y. Majorana zero modes in superconductor–semiconductor heterostructures. *Nature Reviews Materials* **3,** 52–68 (2018).

18. Prada, E., San-Jose, P., de Moor, M. W. A., Geresdi, A., Lee, E. J. H., Klinovaja, J., Loss, D., Nygård, J., Aguado, R. & Kouwenhoven, L. P. From Andreev to Majorana bound states in hybrid superconductor–semiconductor nanowires. *Nature Reviews Physics* **2,** 575–594 (2020).

19. Plugge, S., Rasmussen, A., Egger, R. & Flensberg, K. Majorana box qubits. *New J. Phys.* **19,** 012001 (2017).

20. Hell, M., Leijnse, M. & Flensberg, K. Two-Dimensional Platform for Networks of Majorana Bound States. *Phys. Rev. Lett.* **118,** 107701 (2017).

21. Pientka, F., Keselman, A., Berg, E., Yacoby, A., Stern, A. & Halperin, B. I. Topological Superconductivity in a Planar Josephson Junction. *Phys. Rev. X* **7,** 021032 (2017).

2

THEORY

This chapter provides the theoretical background for the upcoming experiments. We start by reviewing the relevant physical phenomena in a two-dimensional electron gas (2DEG) realized in a semiconductor heterostructure. Then, superconductivity is discussed with a focus on Josephson junctions (JJs) and Andreev bound states. Lastly, we see describe how 2DEG-based JJs can be used to create phase-controllable Majorana zero-modes, and discuss important extensions for these proposals.

2.1. TWO-DIMENSIONAL ELECTRON GASES

2.1.1. FROM BULK CRYSTALS TO HETEROSTRUCTURES

2

In quantum mechanics, a particle is described by a wave function, Ψ, which can be obtained by solving the Schrödinger equation. For a stationary (time-independent) system, this equation is given by [1]:

$$H_0\Psi = E\Psi,$$

with H_0 being the Hamiltonian of the system and E its eigenenergies. Applying this equation to a semiconductor crystal allows one to calculate the bandstructure of it. For this, the periodic potential arising from the crystal, $V(\boldsymbol{R})$, has to be taken into account and enters the Hamiltonian. Expressing the electron wave function as Bloch functions consisting of a plane wave and a lattice periodic part, and using $\boldsymbol{k}\cdot\boldsymbol{p}$ perturbation theory, the energy of band n is found to be [2]:

$$E_n(\boldsymbol{K}) = E_n + \frac{\hbar^2\boldsymbol{K}^2}{2m_e} + \frac{\hbar^2}{m_e^2}\sum_{m,m\neq n}\frac{|\boldsymbol{K}\cdot\boldsymbol{P}_{mn}|^2}{E_n - E_m}. \tag{2.1}$$

Here, E_n is the band edge energy, $\hbar$ is the reduced Planck constant, $\boldsymbol{K} = (k_x, k_y, k_z)$ is the three-dimensional electron wave vector and m_e is the free electron mass. For the conduction band, which is populated by electrons, eq. 2.1 can be approximated by:

$$E_c(\boldsymbol{K}) = E_c + \frac{\hbar^2\boldsymbol{K}^2}{2m^*}, \tag{2.2}$$

with m^* being the effective electron mass. Recall that this is the dispersion relation of a free electron with a renormalized, material specific effective mass. Holes populate states in the valence band that is separated from the conduction band by an energy gap (band gap).

Growing semiconductors with different band gaps on top of each other in a so-called heterostructure allows to create a spatially varying potential (conduction band edge) along the growth direction, z. Specifically, a potential well might be realized (see Fig. 2.1a), restricting the motion of electrons in z. This leads to quantized eigenenergies for the motion in the z-direction, ε_i, while the free motion in x and y can be described by a parabolic dispersion relation (cf. eq. 2.2) [3]:

$$E_i(\boldsymbol{k}) = E_c + \varepsilon_i + \frac{\hbar^2\boldsymbol{k}^2}{2m^*},$$

with $\boldsymbol{k} = \left(k_x, k_y\right)$. Here, we have skipped over complications arising from the interfaces between the different semiconductor materials forming the barrier and the well, and have furthermore assumed that the electron wave function predominately resides in the well, picking up the effective mass of this material only. Such a strict confinement of the wavefunction can only be realized in an idealized well with infinitely high barriers, in which case $\varepsilon_i = \frac{\hbar^2}{2m^*}\left(\frac{i\pi}{d}\right)^2$, with i being an integer (quantum number) and d being the thickness of the well. The parabola for each i is called a subband (sketched in Fig. 2.1b),

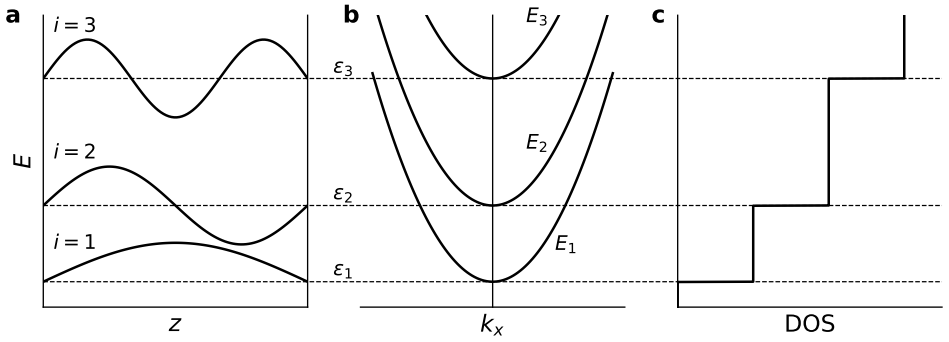

Figure 2.1: **a,** Potential well with infinitely high barriers. The three lowest bound state energies and the corresponding electron wave functions are indicated. **b,** Dispersion relation for the system with restricted motion in z and free motion in x and y. **c,** Total density of states (DOS) of the system. Each subband contributes a step of $m^*/\pi\hbar^2$.

having a constant density of states of $m^*/\pi\hbar^2$ (see Fig. 2.1c).

At zero temperature, the states are filled up to the electrochemical potential, μ. If μ lies within ε_1 and ε_2, only the states in the lowest subband are occupied and the electron motion is two-dimensional. The sheet electron density for one occupied subband can be calculated by integrating the product of the density of states and the Fermi-Dirac distribution function from the bottom of the subband, ε_1, to μ. In the low-temperature limit this results in [2]:

$$n = \frac{m^*}{\pi\hbar^2}(\mu - \varepsilon_1) = \frac{m^*}{\pi\hbar^2}E_\mathrm{F},$$

with E_F being the Fermi energy. The Fermi wave vector is given by: $k_\mathrm{F} = \sqrt{2m^*E_\mathrm{F}/\hbar^2} = \sqrt{2\pi n}$.

2.1.2. ZEEMAN EFFECT

So far we have neglected that the electrons posses a spin degree of freedom. The action of an external magnetic field, $\boldsymbol{B}$, on the electron spin is described by the Zeeman Hamiltonian [2]:

$$H_\mathrm{Z} = \frac{1}{2}g\mu_\mathrm{B}\boldsymbol{\sigma}\cdot\boldsymbol{B}. \tag{2.3}$$

Here, g is the electron g-factor, μ_B is the Bohr magneton and $\boldsymbol{\sigma}$ is a vector containing the Pauli matrices. The field aligns the spin either parallel or anti-parallel to it, leading to a Zeeman splitting of each subband into two spin branches with energies

$$E_\mathrm{Z} = \pm\frac{1}{2}g\mu_\mathrm{B}B.$$

The separation between the two branches, $\Delta E_Z = g\mu_B B$, is called the Zeeman energy.

2.1.3. SPIN-ORBIT COUPLING

The spin of an electron can couple to its orbital motion if the electron moves in an electric field. Naively, this is because the electron experiences in its own rest frame not only the electric field but also a magnetic field, which couples to the spin. The more rigorous description of this effect stems from a non-relativistic approximation of the Dirac equation, resulting in the Hamiltonian [2]:

$$H_{SO} = \frac{\hbar}{4m_e^2c^2}\left(\nabla V(\boldsymbol{r}) \times \hat{\boldsymbol{p}}\right)\cdot\boldsymbol{\sigma}, \tag{2.4}$$

where c is the speed of light and $\hat{\boldsymbol{p}}$ is the momentum operator. The gradient of the periodic crystal potential constitutes the electric field in which the electrons move.

Spin-orbit coupling (SOC) has important consequences for the band structure of bulk semiconductors, first realized in [4, 5]. Accounting for the SOC Hamiltonian in eq. 2.4 and using the $\boldsymbol{k}\cdot\boldsymbol{p}$ method it can be shown that SOC leads to a splitting of the threefold degenerate valence band edge in all diamond and zinc-blende semiconductors. The branch with conserved total angular momentum $j = 1/2$ is lowered in energy compared to the two branches with $j = 3/2$, forming the so-called spin-orbit split-off band [6]. Furthermore, in crystals without inversion symmetry, an additional SOC effect emerges, leading to the spin splitting of states at finite wave vector even in the absence of a magnetic field [7, 8]. SOC also impacts the Zeeman splitting when a magnetic field is applied. Due to SOC, the g-factor can differ significantly from the free electron g-factor ($g = 2$) and is rather described by an effective g-factor, g^* [9].

For a two-dimensional electron gas in a semiconductor heterostructure, two different types of SOC might occur: Rashba and Dresselhaus SOC [2]. The first results from a spatial asymmetry of the confinement potential (structure inversion asymmetry). The latter originates (as for bulk semiconductors) from a lack of inversion symmetry of the crystal lattice (bulk inversion asymmetry). This is, for example, the case in zinc-blende semiconductors like InAs or InSb. For heterostructures grown in the [001]-direction, the SOC Hamiltonian containing both contributions is given to the lowest order in $\boldsymbol{k}$ as [10]:

$$H_{SO} = \alpha\left(\sigma_x k_y - \sigma_y k_x\right) + \beta\left(\sigma_x k_x - \sigma_y k_y\right). \tag{2.5}$$

Here, α is the Rashba coefficient that depends on an average electric field in the growth direction, $\langle E_z\rangle$: $\alpha = \alpha_0\langle E_z\rangle$, with a material-specific constant α_0 [2]. A contribution to $\langle E_z\rangle$ comes from the asymmetric confinement potential but it can also by impacted by an external electric field. The Dresselhaus coefficient is given by $\beta = \beta_0\langle k_z^2\rangle$, where $\langle k_z^2\rangle$ is on the order of $(\pi/d)^2$ [2]. Therefore, the Dresselhaus contribution is stronger in thinner quantum wells.

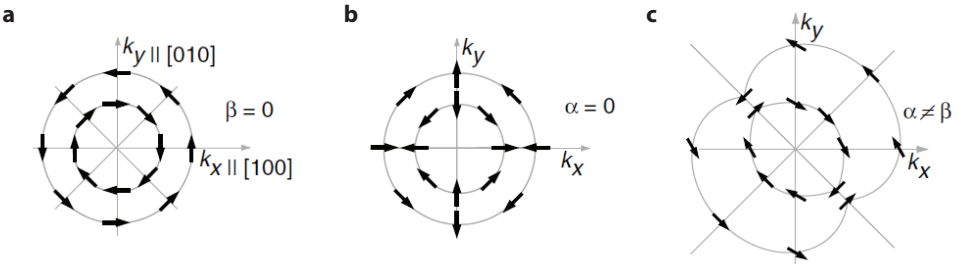

Figure 2.2: **a,** Contours of constant energy and spin orientations at the Fermi energy for Rashba SOC only. The spins are always aligned perpendicular to $\boldsymbol{k}$. **b,** The same as for **a** but with Dresselhaus SOC only. **c,** Fermi contours and spin texture for comparable but not equal Rashba and Dresselhaus SOC. This figure is taken from [10].

Equation 2.5 leads to a profound modification of the energy dispersion relation. In the case of Rashba (or Dresselhaus) SOC only, the subband splits into two parabolic spin branches with shifted minima in all $\boldsymbol{k}$-directions by $k_{\mathrm{SO}} = \pm m^*\alpha/\hbar^2$ ($\pm m^*\beta/\hbar^2$). The energy difference between the bottom of the two branches and the energy at $\boldsymbol{k} = 0$ is called E_{SO}. The energy shift at the Fermi level is called Δ_{SO} and is given by $2\alpha k_{\mathrm{F}}$ ($2\beta k_{\mathrm{F}}$).

The spin orientation can be found by rewriting equation 2.5 in the form $H_{\mathrm{SO}} = \boldsymbol{\sigma}\cdot\boldsymbol{B}_{\mathrm{eff}}(\boldsymbol{k})$. The effective magnetic field

$$\boldsymbol{B}_{\mathrm{eff}}(\boldsymbol{k}) = \begin{pmatrix} \alpha k_y + \beta k_x \\ -\alpha k_x - \beta k_y \\ 0 \end{pmatrix}$$

provides the local ($\boldsymbol{k}$-dependent) spin quantization axis. The contours of constant energy as well as the spin texture at the Fermi level are shown in Fig. 2.2 for different values of α and β.

2.2. SUPERCONDUCTIVITY AND JOSEPHSON JUNCTIONS

2.2.1. BASICS OF SUPERCONDUCTIVITY

In the previous section we considered a gas of non-interacting electrons, whose ground state corresponds to the complete filling of single electron energies up to the Fermi energy. When turning on a weak attractive interaction between electrons with energies around E_{F} (mediated by electron-phonon coupling), this state becomes unstable [11]. Electrons with opposite wave vector and spin form Cooper pairs, which are bosons, and they condense into a new ground state. The single particle excitations occupy states that are separated by an energy gap (pair potential) Δ from the condensate at E_{F}. These excitations, called Bogoliubov quasiparticles, have an electron and a hole component, u and v respectively, and are described by the Bogoliubov-de Gennes (BdG) equation making use of a mean field approximation [11]:

$$H_{\mathrm{BdG}}\begin{pmatrix}u\\v\end{pmatrix} = E\begin{pmatrix}u\\v\end{pmatrix}, \qquad H_{\mathrm{BdG}} = \begin{pmatrix}H & \Delta\\ \Delta^* & -H^*\end{pmatrix} \tag{2.6}$$

Here, H is the single-electron Hamiltonian. Equation 2.6 results in a particle-hole symmetric excitation spectrum. For every eigenvector with energy E there is a corresponding eigenvector with energy $-E$. Together they describe the same quasiparticle excitation.

This summarizes some of the most important findings of the Bardeen, Cooper and Schrieffer (BCS) theory that succeeded to describe superconductivity at a microscopic level [12]. 7 years earlier, Ginzburg and Landau (GL) developed a (macroscopic) theory, introducing a complex wave function (order parameter), $\Psi = |\Psi|\exp(i\theta)$, to describe the superconducting condensate [13]. In 1959, it was shown that the GL theory emerges as a limiting case from the BCS theory (valid near the critical temperature), and that Ψ is proportional to Δ [14].

2.2.2. JOSEPHSON TUNNEL JUNCTIONS

The importance of the phase, θ, in the GL wavefunction can be seen when considering two superconductors separated by a thin insulating layer. In 1962, Brian Josephson considered the quantum mechanical tunneling of electrons through the insulator and predicted that a dissipationless current (supercurrent) would flow, driven by the phase difference between the two superconductors, $\phi = \theta_{\mathrm{L}} - \theta_{\mathrm{R}}$ [15]:

$$I = I_{\mathrm{c}}\sin(\phi), \tag{2.7}$$

Here, I_{c} is the maximum supercurrent that is supported by the Josephson junction (JJ), called critical current. Subsequently, the DC Josephson effect (described by equation 2.7) was confirmed by a large amount of experiments [16]. Nowadays it is clear that the Josephson effect occurs more generally, whenever two superconductors are connected by a "weak link". Besides an insulator, this could be a metal or a semiconductor.

2.2.3. ANDREEV REFLECTION AND ANDREEV BOUND STATES

In a superconductor-semiconductor-superconductor JJ, the supercurrent transport is typically no longer due to tunneling, and a different mechanism has to be taken into account. When a right-moving electron in the semiconductor with an energy smaller than Δ is incident on the right semiconductor-superconductor interface (see Fig. 2.3a) it cannot enter the superconductor because no quasiparticle states exist below the energy gap. It also cannot undergo normal reflection assuming the absence of a potential barrier at the interface. However, the electron can combine with another electron to form a Cooper pair, which is then allowed to enter the superconductor. As a consequence, a hole with opposite wave vector and spin is left behind in the semiconductor, traveling back on the same path as the original electron. This process is called Andreev reflection [17].

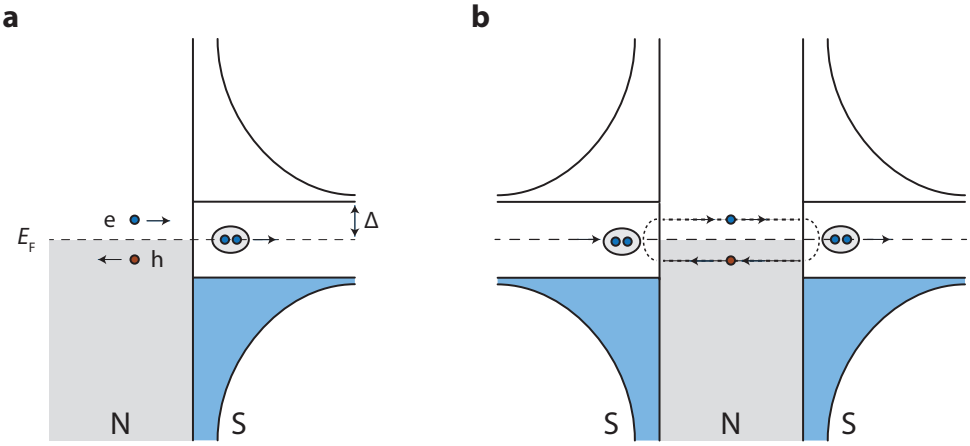

Figure 2.3: **a,** Schematic representation of Andreev reflection. At the semiconductor (N)-superconductor (S) interface, the incoming electron is retroreflected as a hole and a Cooper pair is transferred into the superconductor. **b,** In a S-N-S JJ, the hole impinging on the left interface undergoes Andreev reflection again and a so-called Andreev bound state forms if the phase coherence between the two superconductors is preserved.

Once the hole reaches the left superconductor it will undergo Andreev reflection again and will be transformed into an electron (see Fig. 2.3b). Then, effectively, a Cooper pair is transported through the JJ. If, during this process, the phase coherence between the two superconductors is preserved, a so-called Andreev bound state (ABS) forms. Using the BdG formalism for a one-dimensional JJ with a step-like pair potential increase and no barriers at the interfaces yields the following expression for the ABS energies (Andreev levels), $E(\phi)$ [18]:

$$2\frac{L}{\xi}\frac{E(\phi)}{\Delta} = 2\pi n + 2\arccos\left(\frac{E(\phi)}{\Delta}\right) \mp \phi, \tag{2.8}$$

where L is the length of the semiconductor, $\xi = \hbar v_F/\Delta$ is the superconducting coherence length, and $n = 0, 1, 2....$ We assumed no scattering in the semiconductor region ($L < l_e$), which is referred to as a ballistic JJ. In this case, the Thouless energy is defined as $E_{Th} = \hbar v_F/2L$, allowing the left-hand side of equation 2.8 to be expressed as $E(\phi)/E_{Th}$. The JJ might further be classified by comparing L with ξ. In the short junction limit ($L < \xi$), $E(\phi)/E_{Th}$ can be neglected, and the Andreev levels are:

$$E(\phi) = \pm\Delta\cos\left(\frac{\phi}{2}\right) \tag{2.9}$$

Both of these levels are spin-degenerate, amounting to four Andreev levels in total. Equation 2.9 can be generalized for a JJ with multiple channels and scattering in the semiconductor region (described by transmissions τ_i) [19], where each channel i contributes two spin-degenerate Andreev levels:

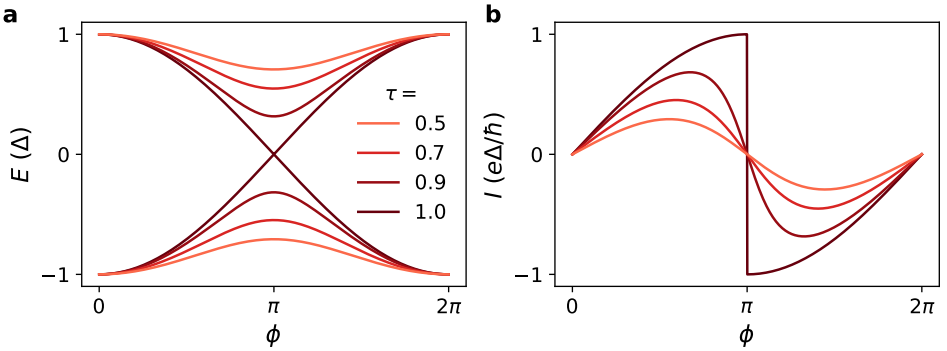

Figure 2.4: **a,** Andreev levels for a single-channel JJ with different transmissions. $\tau < 1$ leads to an avoided crossing at $\phi = \pi$. **b,** Corresponding CPRs. As the transmission is lowered the CPR changes from skewed to sinusoidal.

$$E_i(\phi) = \pm\Delta\sqrt{1-\tau_i \sin^2\left(\frac{\phi}{2}\right)} \tag{2.10}$$

The ground state energy of the JJ is obtained by summing over the negative Andreev levels:

$$E_0(\phi) = -\sum_i |E_i(\phi)|. \tag{2.11}$$

The ABSs carry a supercurrent, at zero temperature given by:

$$I(\phi) = \frac{2e}{\hbar}\frac{\mathrm{d}E_0(\phi)}{\mathrm{d}\phi} = -\frac{2e}{\hbar}\sum_i \frac{\mathrm{d}|E_i(\phi)|}{\mathrm{d}\phi} \tag{2.12}$$

Inserting equation 2.10 yields:

$$I(\phi) = \frac{e\Delta}{2\hbar}\sum_i \frac{\tau_i \sin(\phi)}{\sqrt{1-\tau_i \sin^2(\phi/2)}} \tag{2.13}$$

This expression links the supercurrent to the phase difference between the two superconductors, and is called current-phase relation (CPR). From the CPR the critical current can be extracted: $I_c = \max_\phi |I(\phi)|$. In the limit of low transmissions, the CPR approaches equation 2.7, with $I_c = e\Delta/(2\hbar)\sum_i \tau_i$.

The Andreev levels and the corresponding CPR for a single-channel JJ with varying transmission are plotted in Fig. 2.4. Normal scattering leads to the opening of an energy gap at $\phi = \pi$ with increasing gap size for decreasing transmission. The CPR transitions from skewed to sinusoidal for increasing scattering (decreasing transmission).

2.2.4. ANDREEV BOUND STATES IN THE PRESENCE OF A ZEEMAN FIELD AND SPIN-ORBIT COUPLING

In the previous discussion we assumed $\Delta << E_F$, which is known as the Andreev limit, and neglected the effects of spin-orbit interaction and a Zeeman field. Once E_F is lowered and becomes comparable to the spin-orbit energy and the Zeeman energy, these effects become relevant.

In this regard, we will review the most important findings of the numerical calculations presented in [20]. The system under investigation is a short, quasi-ballistic and few-channel JJ based on a semiconductor with Rashba SOC, subject to a Zeeman field ($E_Z, \Delta << E_F$). A device schematic is shown in Fig. 2.5a and b. In order to obtain the Andreev levels, the BdG equation (equation 2.6) is written in terms of a scattering matrix, which is obtained from a tight-binding model. The single-electron Hamiltonian in the BdG Hamiltonian is composed of $H = H_0 + H_{SO} + H_Z$, where H_0 contains a kinetic term as well as a confinement and an impurity potential. H_{SO} and H_Z are given by equation 2.5 and 2.3, respectively. The magnetic field, B_y, is applied along the y-axis, mostly parallel to the spin quantization axis for Rashba SOC and motion mainly along the x-axis. It splits the dispersion relation, causing an additional (average) phase shift between the electrons and holes that form the ABSs, $\theta_B = g^* \mu_B B_y L/(\hbar \overline{v}_F)$, where $\overline{v}_F$ is the inversion average Fermi velocity.

We consider a single conduction channel and no SOC first. In the absence of a magnetic field, the two Andreev levels are spin-degenerate as discussed above (see Fig. 2.5c). The ground-state energy is minimal at $\phi_0 = 0$. The application of a magnetic field causes spin-splitting of the Andreev levels, leading to zero energy crossings as the field is increased. At $\theta_B = \pi/2$, the ground-state energy switches to being minimal at $\phi_0 = \pi$, which is called a $0-\pi$ transition. The JJ remains in the π-state until $\theta_B = 3\pi/2$, where it switches back to the 0-state. Figure 2.5d shows the CPR for different θ_B. Since the Andreev levels obey $E(-\phi) = E(\phi)$ for all θ_B, the CPR satisfies $I(-\phi) = -I(\phi)$ and hence $I(\phi = 0) = 0$. The $0-\pi$ transitions are accompanied by cusps in the critical current, as shown in Fig. 2.5e.

Next, we review the single-channel case where SOC is present ($k_{SO}/k_F = 0.15$). Without applied magnetic field, the two Andreev levels are still twofold degenerate despite the SOC (see Fig. 2.5f), which is attributed to the short junction limit (in long and intermediate junctions, an Andreev level splitting is present at $\phi \neq 0, \pi$ [21, 22]). $E(-\phi) = E(\phi)$ holds, and the ground state energy is minimal at $\phi_0 = 0$. A magnetic field splits the two Andreev levels. The invariance of the levels against the ϕ-inversion is broken, leading to a finite supercurrent at $\phi = 0$ (anomalous supercurrent) and a ground state energy that is minimal at a phase ϕ_0 in between 0 and π, shown in Fig. 2.5g and h. ϕ_0 grows linearly with field until a π-jump happens ($0-\pi$ transition), followed by another gradual phase increase. Finally, the JJ transits back to a 0-like state. As before, the $0-\pi$ transitions lead to local minima in the critical current. Note that the $0-\pi$ transitions happen at somewhat larger magnetic fields compared to the situation without SOC.

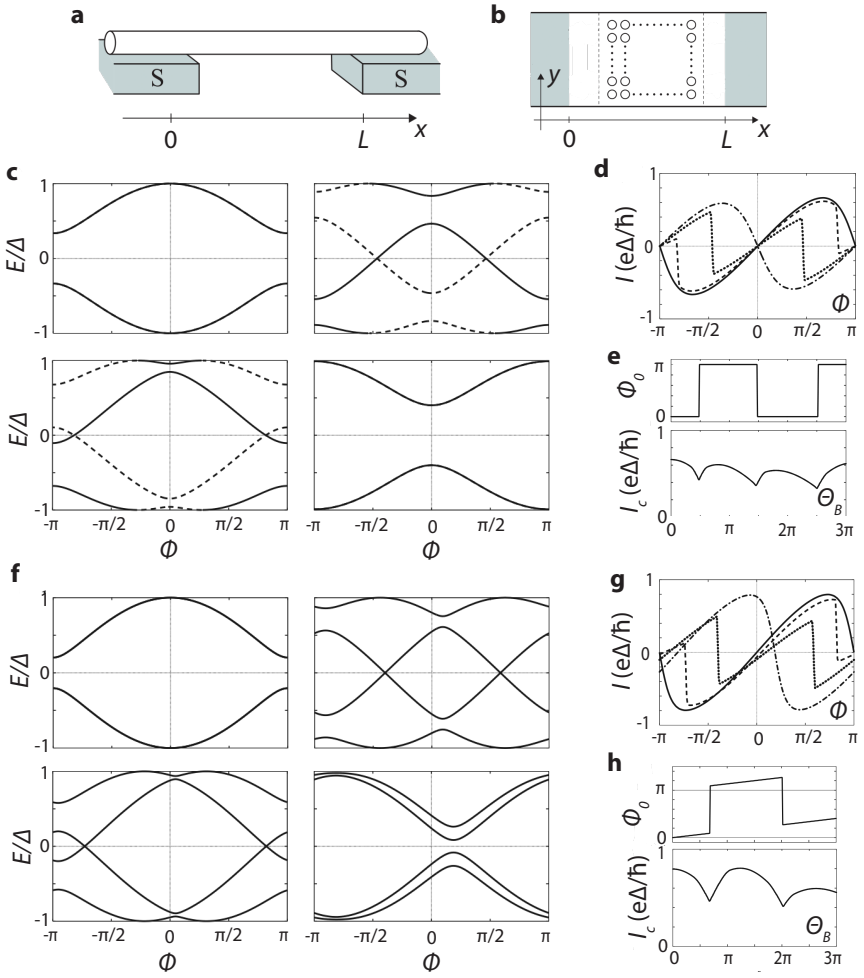

Figure 2.5: **a,** Schematic of the JJ. The scattering region inside the semiconductor is indicated in **b**, having a scattering strength $l_e/L = 1$. A magnetic field is applied along the y-direction, causing a phase shift $\theta_B \propto B_y$. **c,** Andreev levels for a single-channel JJ in the absence of SOC. $\theta_B = 0, 0.27\pi, 0.53\pi$ and π in the top-left, bottom-left, top-right and bottom-right image. **d,** CPRs for $\theta_B = 0$ (solid), 0.27π (broken), 0.53π (dotted), π (dotted broken). **e,** Phase that minimizes the ground state energy (top panel), and critical current (bottom panel) as a function of θ_B. At $\theta_B = (n+1/2)\pi$, transitions to the π (0) state happen, accompanied by minima in the critical current. **f,** Andreev levels for a single-channel JJ in the presence of SOC, $k_{SO}/k_F = 0.15$. $\theta_B = 0, 0.35\pi, 0.7\pi$ and 1.4π in the top-left, bottom-left, top-right and bottom-right image. **g,** CPRs for $\theta_B = 0$ (solid), 0.35π (broken), 0.7π (dotted), 1.4π (dotted broken). A finite B_y leads to an anomalous phase shift. **h,** Phase that minimizes the ground state energy (top panel), and critical current (bottom panel) as a function of θ_B. Figures adapted from [20].

Qualitatively similar results are obtained when considering more conduction channels (two or four), both in the absence and presence of SOC, despite the fact that the channels mix due to impurity scattering (and SOC). The amount of channels is determined by the ration between the Fermi wave length and the width of the semiconductor. Calculations for an extended, planar JJ based on a Rashba 2DEG confirm the occurrence of $0-\pi$ transitions for multiple-channel systems (using a quasi-classical approximation). Here, magnetic field rotations are also considered. When SOC is absent, the $0-\pi$ transitions happen at the same field values irrespective of the field direction. In the presence of SOC, the SOC effects are relatively weak when the magnetic field is in the y-direction (mostly parallel to the SOC field for motion mainly along x), whereas they are stronger when the magnetic field points in the other two directions [23]. In the following section, we will also focus on $0-\pi$ transitions in planar JJs based on a Rashba 2DEG, and will see that they are in fact accompanied by a topological phase transition.

2.3. TOPOLOGICAL SUPERCONDUCTIVITY IN A PLANAR JOSEPHSON JUNCTION

2.3.1. INITIAL PROPOSALS

In 2017 it was realized that Majorana zero modes, that arise as end states in a one-dimensional topological superconductor, can be created in the normal region of a 2DEG-based planar JJ [24, 25]. Figure 2.6a shows a schematic of such a device, where a 2DEG with Rashba SOC is contacted by two s-wave superconductors. The superconductors have a phase difference of ϕ, and a magnetic field, B, is applied in the x-direction.

In [25], two experimental configurations are described. In the first one (see Fig. 2.6b), the phase difference is controlled externally, which can be realized by threading a magnetic flux through a loop that connects the two superconductors. Strikingly, at $\phi = \pi$ the system enters the topological regime (light blue) for small magnetic fields (Zeeman energies). This is in stark contrast to the more commonly researched hybrid nanowire proposals [26, 27], where a large magnetic field is required to enter the topological regime. At $\phi = 0$, the JJ remains in the trivial regime (white) except for isolated magnetic field values. Therefore, the phase difference serves as a switch that controls the topology of the JJ.

In the second configuration, the in-plane magnetic field is applied without controlling the phase externally (see Fig. 2.6c). Upon increasing the magnetic field, the phase that minimizes the ground state energy, ϕ_0, abruptly jumps from 0 to π ($0-\pi$ transition), and eventually back to 0. Interestingly, the JJ is in the trivial regime for $\phi_0 = 0$, whereas it is in the topological regime for $\phi_0 = \pi$. Thus, the JJ self-tunes into (and out of) the topological regime, accompanied by an oscillating critical current with local minima at the transition points. We will look at these two configurations in more detail now.

PHASE-BIAS

Following [25], the BdG Hamiltonian in the Nambu basis describing the JJ is given by:

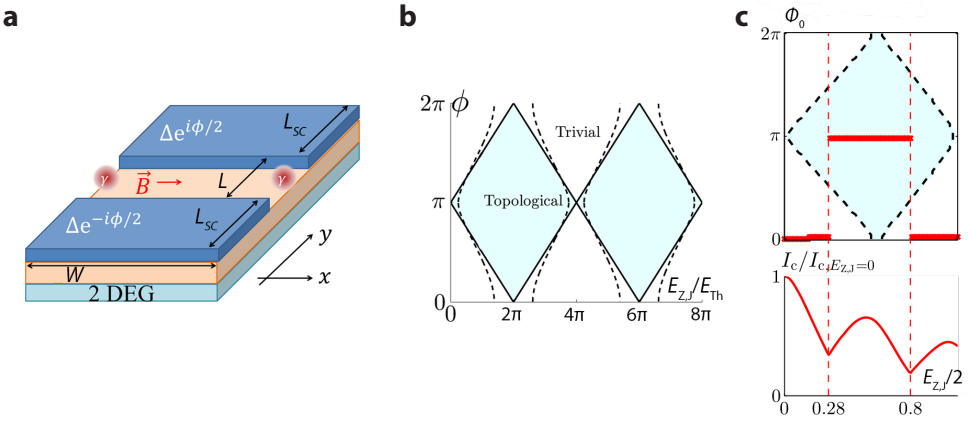

Figure 2.6: **a,** Schematic of the planar JJ using a 2DEG (light blue) with Rashba SOC. The two superconductors (dark blue) have a phase difference of ϕ. When tuning the magnetic field in the x-direction (and ϕ) to the correct value(s), MZMs emerge at the ends of the narrow normal region (red circles). **b,** Phase diagram when controlling ϕ externally. At $\phi = \pi$, the topological regime (light blue) is reached at an extremely small magnetic field. When considering normal scattering at the semiconductor-superconductor interfaces ($\tau = 0.75$), the boundaries separating the trivial and topological regimes change to the dashed lines. The ϕ-dependence weakens and trivial (topological) regions emerge at $\phi = \pi$ (0). **c,** Without phase control, the system self-tunes into the topological regime by minimizing its ground-state energy (top panel). The $0-\pi$ transitions are accompanied by local minima in the critical current (bottom panel). Both quantities are obtained from a numerical calculation (parameters specified in [25]). All figures are adapted from [25].

$$H_{\mathrm{BdG}} = \left(\frac{\hbar^2 \left(k_x^2 - \partial_y^2\right)}{2m^*} - \mu + \frac{m^* \alpha^2}{2\hbar^2} \right) \tau_z + \alpha \left(k_x \sigma_y + i \partial_y \sigma_x\right) \tau_z + E_{\mathrm{Z}}(y) \sigma_x / 2 + \Delta(y) \tau_+ + \Delta^*(y) \tau_- \tag{2.14}$$

A different Zeeman energy, $E_{\mathrm{Z}}(y)$, is considered in the 2DEG regions that are covered with the superconducting leads and in the normal region. We will neglect the Zeeman effect underneath the leads, assuming a small effective g-factor in these regions, and only focus on the Zeeman effect in the normal region: $E_{\mathrm{Z}}(y) = E_{\mathrm{Z,J}} = g^* \mu_{\mathrm{B}} B$. The superconducting pairing in the normal region is given by:

$$\Delta(y) = \Delta \exp\left[i\{\mathrm{sgn}(y)\}\phi/2\right] \Theta(|y| - L/2).$$

The Pauli matrices σ and τ act on the spin and particle-hole degree of freedom, respectively, and $\tau_\pm = (\tau_x \pm i\tau_y)/2$.

The topological invariant, determining whether the JJ is in the trivial or topological regime, is given by the ground state parity of the BdG Hamiltonian in equation 2.14 at $k_x = 0$. As

we have seen before, at $k_x = 0$, the spin-orbit field points in the same direction as the Zeeman field (x-direction), and the Rashba SOC can be gauged away, leading to an effective Hamiltonian:

$$H_{\text{eff}} = \left(-\partial_y^2/(2m^*) - \mu\right)\tau_z + E_{\text{Z,J}}(y)\sigma_x/2 + \Delta(y)\tau_+ + \Delta^*(y)\tau_-$$

Assuming $\mu >> \Delta$, $E_{\text{Z,J}}$ and no normal reflection at the semiconductor-superconductor interfaces, the bound state spectrum can be derived as:

$$\arccos(E/\Delta) = \frac{1}{2}\frac{E}{E_{\text{Th}}} - \frac{1}{4}\frac{E_{\text{Z,J}}}{E_{\text{Th}}} \pm \frac{\phi}{2} + n\pi, \tag{2.15}$$

with the ballistic Thouless energy $E_{\text{Th}} = \hbar v_{\text{F}}/2L$. Note that this is the same expression as in equation 2.8 with an additional phase shift due to the Zeeman field, $\theta_B = E_{\text{Z,J}}/(2E_{\text{Th}}) = g^*\mu_{\text{B}}BL/(\hbar v_F)$.

At zero magnetic field, the Andreev levels are spin-degenerate. Therefore, the ground state parity is even for all values of ϕ. A Zeeman field splits the degeneracy and causes non-degenerate Andreev levels to cross zero energy as the phase is varied (see top panels in Fig. 2.8 for a plot of the Andreev levels in the short junction limit). At these crossings, the ground state parity changes. Thus, setting $E = 0$ in equation 2.15 yields the boundaries of the topological phase diagram:

$$\frac{1}{4}\frac{E_{\text{Z,J}}}{E_{\text{Th}}} \pm \frac{\phi}{2} = \frac{\pi}{2} + \pi n$$

This expression causes the alternating trivial and topological regimes with a diamond shape, plotted in Fig. 2.6 b. Scattering in the semiconductor region or at the semiconductor-superconductor interfaces leads to deviations from this ideal behavior, where trivial (topological) regions form at $\phi = \pi$ (0), see dashed lines in the same figure for the new boundaries.

Driving the system into the topological regime results in the formation of Majorana zero modes at the ends of the junction's normal region and a re-opening of the bulk gap (topological gap). The size of topological gap determines the localization of the Majorana wave functions is therefore an important quantity. It is given by the Andreev level with the lowest energy, taking into account all k_x:

$$\Delta_{\text{top}}(\phi) = \min_{k_x}\left(\left|E(k_x, \phi)\right|\right)$$

A numerical calculation of the size of the topological gap for a short junction is shown in Fig. 2.7. The diamond-shaped phase boundaries are visible in dark brown, indicating the vanishing topological gap. Inside the topological regime, Δ_{top} reaches values up to 0.3Δ. As shown in the right panel, the topological gap at $\phi = \pi$ is sizable for a large range of Zeeman fields, with little dependence on the chemical potential.

The MZMs may be detected by measuring the local density of states at the ends of the JJ via tunneling spectroscopy, while the topological gap can be extracted from nonlocal

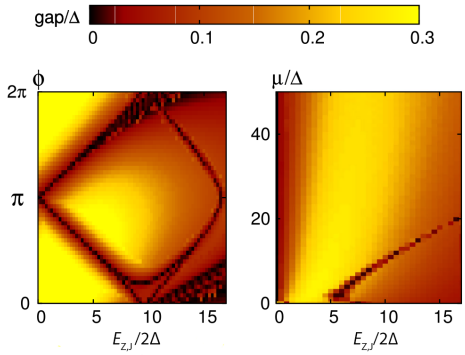

Figure 2.7: (Left panel) Induced gap as a function of phase and Zeeman energy for $m^*\alpha^2/\hbar^2 = 9\Delta$ and $\mu/\Delta = 20$. Inside the diamond-shaped topological regime, the topological gap reaches 0.3Δ. (Right panel) Topological gap for varying chemical potential and Zeeman energy at $\phi = \pi$. This figure is adapted from [25].

conductance measurements. Chapter 6 deals with tunneling spectroscopy at zero Zeeman field, while both local and nonlocal conductance measurements at varying Zeeman fields are presented in chapter 7 (along with technical details about the nonlocal measurements).

SELF-TUNING

When the phase is not controlled externally, the JJ self-tunes into the topological regime upon increasing the Zeeman field, indicated by a $0-\pi$-transition. This can be understood qualitatively by considering a short, single-channel (with $k_x = 0$) JJ, where the Andreev levels are given by (see equation 2.15): $E = \pm\Delta\cos(E_{Z,J}/(4E_{Th}) \pm \phi/2)$, with $\theta_B = E_{Z,J}/(2E_{Th})$. This is plotted in the top panels of Fig. 2.8 for different $E_{Z,J}/E_{Th}$. The bottom panels contain the corresponding ground state energy and CPR, where the former is obtained by summing over both spin species with negative energies $E_0 = -(|E_+| + |E_-|)/2)$, and the latter is calculated according to equation 2.12.

At $E_{Z,J}/E_{Th} = 0$, the Andreev levels are spin-degenerate and the ground-state energy is minimal at $\phi_0 = 0$. At $E_{Z,J}/E_{Th} = \pi$, the ground-state energy switches to be minimal at $\phi_0 = \pi$. Note that this phase lies in the region with switched parity, indicating a topological phase transition. From the CPR plots it can be seen that the $0-\pi$ transition is accompanied by a minimum in the critical current. A tight-binding calculation of the phase that minimizes the ground state energy (considering all k_x), together with the critical current is shown in Fig. 2.6c (in the regime $E_{Z,J} \geq \alpha k_F$).

In chapter 4, $0-\pi$ transitions in ballistic JJs formed in an InSb 2DEG are investigated. Specifically, the expected tunabilty of these transitions with the experimentally controllable parameters (JJ length, electron density, applied magnetic field) will be demon-

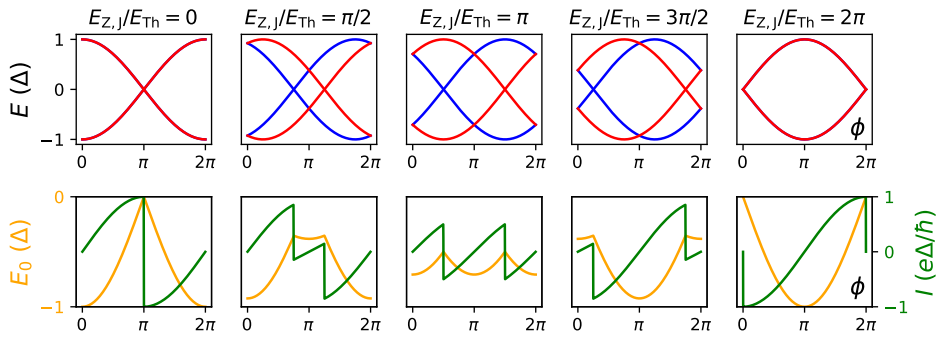

Figure 2.8: Andreev levels (top panel) and corresponding ground state energy and CPR (bottom panel) for a short, single-channel JJ at different $E_{Z,J}/E_{Th}$. A Zeeman field splits the two spin species (indicated in red and blue in the top panels). At $E_{Z,J}/E_{Th} = \pi$ a transition to the π-state occurs.

strated.

2.3.2. IMPORTANT EXTENSIONS

In the previous section we have already seen how normal scattering in the semiconductor or at the semiconductor-superconductor interfaces impacts the phase diagram when ϕ is controlled externally: it weakens the ϕ-dependence (see dashed lines in Fig. 2.6b).

An additional, but closely related effect is described in detail in [28]. Here, the same planar JJ geometry is considered, but with superconducting leads that are shorter than the superconducting coherence length, see left panel in Fig. 2.9a (previously $L_{sc} \to \infty$ was assumed). As a result, normal reflections now also occur at the interfaces of the leads with the vacuum, weakening the ϕ-dependence further as shown in the right panel of Fig. 2.9a. Experimentally however, narrow leads are relevant as they increase the Zeeman field compatibility [29, 30]. Hence, there is a tradeoff between phase tunability and Zeeman field compatibility.

Another modification of phase diagram arises when also accounting for Dresselhaus SOC (as opposed to Rashba SOC only). The numerical calculations in [31] show that in this case, trivial regions appear around $\phi = \pi$. This is demonstrated in Fig. 2.9b for $\alpha = 14.3\,\text{meV nm}$ and $\beta = 7.3\,\text{meV nm}$. Here, motion parallel to the S-N interfaces is considered (x-direction), in which case the Rashba SOC field points in the y-direction and the Dresselhaus SOC field is directed along x. Hence, the total SOC field (denoted by n_{SOC} in the schematic on the top right) tilts away from the y-direction. This has to be accounted for by rotating the Zeeman field appropriately such that it is still perpendicular to the total SOC field. Deviations from this condition lead to a reduction of the topological gap size with a vanishing topological gap if the Zeeman field is misoriented by more

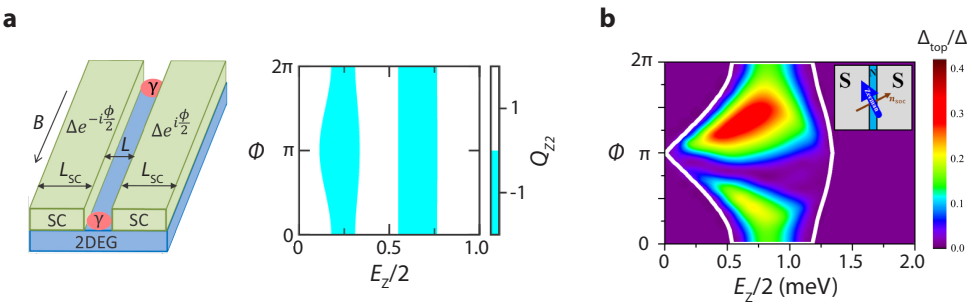

Figure 2.9: **a,** Schematic (left) and phase diagram (right) for a planar JJ with narrow superconducting leads, $L_{sc} < \xi$. The light blue regions in the phase diagram correspond to the topological regimes. Additional normal scattering occurs at the lead-vacuum interfaces, weakening the ϕ-dependence. Figures adapted from [28]. **b,** Phase diagram for a planar JJ with Rashba and Dresselhaus SOC ($\alpha = 14.3\,\text{meV nm}$, $\beta = 7.3\,\text{meV nm}$). A trivial region emerges around $\phi = \pi$. Figure adapted from [31].

than 10°.

Finally, we return to the size of the topological gap being the most important quantity in this system to optimize. While Fig. 2.7 and 2.9b indicate that the topological gap can reach values of up to a third of the size of the parent superconducting gap, the numerical calculations in [32] predict a significantly smaller topological gap of only $\sim 0.01\Delta$. It turns out that the limiting factor is mainly long semi-classical trajectories through the semiconductor without interruption by the superconductors, resulting in a small gap at large k_x. One way to suppress these trajectories is to introduce disorder into the semiconductor, thereby enforcing scattering towards the superconductors. It was shown that the right amount of disorder leads to an increased topological gap and more confined Majorana wave functions [33]. However, this is a double-edged sword since too much disorder reduces the gap size, and scattering is hard to control experimentally. Another approach is to change the geometry of the JJ to prevent long trajectories naturally, for example by using a zigzag shape [32]. This leads to an enhancement of the topological gap by roughly one order of magnitude (to approximately 0.1Δ) compared to the straight junction case.

REFERENCES

1. Griffiths, D. J. & Schroeter, D. F. *Introduction to Quantum Mechanics* 3rd ed. (Cambridge University Press, 2018).
2. Ihn, T. *Semiconductor Nanostructures: Quantum states and electronic transport* (Oxford University Press, United States of America, 2009).
3. Davies, J. H. *The Physics of Low-dimensional Semiconductors: An Introduction* (Cambridge University Press, United States of America, 1997).
4. Adams, E. N. Some Consequences of Possible Degeneracy of Energy Bands in Ge. *Phys. Rev.* **92,** 1063–1064 (1953).
5. Dresselhaus, G., Kip, A. F. & Kittel, C. Spin-Orbit Interaction and the Effective Masses of Holes in Germanium. *Phys. Rev.* **95,** 568–569 (1954).
6. Winkler, R. *Spin-Orbit Coupling Effects in Two-Dimensional Electron and Hole Systems* (Springer, Berlin, Heidelberg, 2003).
7. Parmenter, R. H. Symmetry Properties of the Energy Bands of the Zinc Blende Structure. *Phys. Rev.* **100,** 573–579 (1955).
8. Dresselhaus, G. Spin-Orbit Coupling Effects in Zinc Blende Structures. *Phys. Rev.* **100,** 580–586 (1955).
9. Roth, L. M., Lax, B. & Zwerdling, S. Theory of Optical Magneto-Absorption Effects in Semiconductors. *Phys. Rev.* **114,** 90–104 (1959).
10. Ganichev, S. D., Bel'kov, V. V., Golub, L. E., Ivchenko, E. L., Schneider, P., Giglberger, S., Eroms, J., De Boeck, J., Borghs, G., Wegscheider, W., Weiss, D. & Prettl, W. Experimental Separation of Rashba and Dresselhaus Spin Splittings in Semiconductor Quantum Wells. *Phys. Rev. Lett.* **92,** 256601 (2004).
11. De Gennes, P. G. & Pincus, P. A. *Superconductivity of Metals and Alloys* 1st ed. (CRC Press, 1999).
12. Bardeen, J., Cooper, L. N. & Schrieffer, J. R. Theory of Superconductivity. *Phys. Rev.* **108,** 1175–1204 (1957).
13. Ginzburg, V. L. & Landau, L. D. On the Theory of Superconductivity. *Zh. Eksp. Teor. Fiz.* **20** (1950).
14. Gor'kov, L. P. Microscopic derivation of the Ginzburg-Landau equations in the theory of superconductivity. *Zh. Eksperium. i Teor. Fiz.* **36** (1959).
15. Josephson, B. Possible new effects in superconductive tunnelling. *Physics Letters* **1,** 251–253 (1962).
16. Tinkham, M. *Introduction to Superconductivity* 2nd ed. (Dover Publications, 1996).

17. Annet, J. F. *Superconductivity, Superfluids and Condensates* 1st ed. (Oxford University Press, 2004).
18. Kulik, I. O. Macroscopic Quantization and the Proximity Effect in S-N-S Junctions. *Zh. Eksp. Teor. Fiz.* **57** (1969).
19. Beenakker, C. W. J. Universal limit of critical-current fluctuations in mesoscopic Josephson junctions. *Phys. Rev. Lett.* **67,** 3836–3839 (1991).
20. Yokoyama, T., Eto, M. & Nazarov, Y. V. Anomalous Josephson effect induced by spin-orbit interaction and Zeeman effect in semiconductor nanowires. *Phys. Rev. B* **89,** 195407 (2014).
21. Béri, B., Bardarson, J. H. & Beenakker, C. W. J. Splitting of Andreev levels in a Josephson junction by spin-orbit coupling. *Phys. Rev. B* **77,** 045311 (2008).
22. Chtchelkatchev, N. M. & Nazarov, Y. V. Andreev Quantum Dots for Spin Manipulation. *Phys. Rev. Lett.* **90,** 226806 (2003).
23. Bezuglyi, E. V., Rozhavsky, A. S., Vagner, I. D. & Wyder, P. Combined effect of Zeeman splitting and spin-orbit interaction on the Josephson current in a superconductor-two-dimensional electron gas-superconductor structure. *Phys. Rev. B* **66,** 052508 (2002).
24. Hell, M., Leijnse, M. & Flensberg, K. Two-Dimensional Platform for Networks of Majorana Bound States. *Phys. Rev. Lett.* **118,** 107701 (2017).
25. Pientka, F., Keselman, A., Berg, E., Yacoby, A., Stern, A. & Halperin, B. I. Topological Superconductivity in a Planar Josephson Junction. *Phys. Rev. X* **7,** 021032 (2017).
26. Lutchyn, R. M., Sau, J. D. & Das Sarma, S. Majorana Fermions and a Topological Phase Transition in Semiconductor-Superconductor Heterostructures. *Phys. Rev. Lett.* **105,** 077001 (2010).
27. Oreg, Y., Refael, G. & von Oppen, F. Helical Liquids and Majorana Bound States in Quantum Wires. *Phys. Rev. Lett.* **105,** 177002 (2010).
28. Setiawan, F., Stern, A. & Berg, E. Topological superconductivity in planar Josephson junctions: Narrowing down to the nanowire limit. *Phys. Rev. B* **99,** 220506 (2019).
29. Suominen, H. J., Kjaergaard, M., Hamilton, A. R., Shabani, J., Palmstrøm, C. J., Marcus, C. M. & Nichele, F. Zero-Energy Modes from Coalescing Andreev States in a Two-Dimensional Semiconductor-Superconductor Hybrid Platform. *Phys. Rev. Lett.* **119,** 176805 (2017).
30. Fornieri, A., Whiticar, A. M., Setiawan, F., Portolés, E., Drachmann, A. C. C., Keselman, A., Gronin, S., Thomas, C., Wang, T., Kallaher, R., Gardner, G. C., Berg, E., Manfra, M. J., Stern, A., Marcus, C. M. & Nichele, F. Evidence of topological superconductivity in planar Josephson junctions. *Nature* **569,** 89–92 (2019).
31. Scharf, B., Pientka, F., Ren, H., Yacoby, A. & Hankiewicz, E. M. Tuning topological superconductivity in phase-controlled Josephson junctions with Rashba and Dresselhaus spin-orbit coupling. *Phys. Rev. B* **99,** 214503 (2019).
32. Laeven, T., Nijholt, B., Wimmer, M. & Akhmerov, A. R. Enhanced Proximity Effect in Zigzag-Shaped Majorana Josephson Junctions. *Phys. Rev. Lett.* **125,** 086802 (2020).

33. Haim, A. & Stern, A. Benefits of Weak Disorder in One-Dimensional Topological Superconductors. *Phys. Rev. Lett.* **122,** 126801 (2019).

3

MATERIALS AND FABRICATION

This chapter introduces the 2DEG materials that are used in this thesis: InSb and InSbAs. Their material properties are discussed in light of realizing topological superconductivity. Moreover, the device fabrication using InSb and InSbAs/Al 2DEGs is described, focusing on the key challenges for both platforms. Detailed fabrication recipes can be found in the respective chapters.

3.1. 2DEG GROWTH AND MATERIALS

As we have seen in the previous chapter, realizing MZMs in planar JJs requires a 2DEG with Rashba spin-orbit interaction coupled to a superconductor. Ideally, the Rashba SOC should be strong to enhance the size of the topological gap, leading to well separated MZMs. Moreover, we have seen that a finite Zeeman field is required to drive the system in the topological regime. Therefore, the effective g-factor of the 2DEG should be as as large as possible to reduce the external magnetic field that is needed to induce the topological phase transition. Lastly, we noticed how scattering in the semiconductor or at the semiconductor-superconductor interfaces causes deviations from the ideal behavior, where the JJ enters the topological regime at a low Zeeman field when the phase difference is tuned to π. Hence, the disorder in the 2DEG should be low and the semiconductor-superconductor interface as clean as possible. All of this requires a careful choice of materials on the one hand, and the right growth techniques on the other hand.

High-quality 2DEGs can be grown by molecular beam epitaxy (MBE), where atom beams (containing the materials of interest) interact with a heated growth substrate in an ultra-high vacuum chamber. This technique allows to grow single-crystal layers with very good control over the chemical composition in the layer and the layer thickness (down to a single atomic layer) [1]. The confinement of electrons to two dimensions is typically realized by growing the 2DEG material of interest in between layers of larger bandgap semiconductors (called top and bottom barrier). In order to achieve high mobility 2DEGs, the different semiconductors must have almost identical lattice constants. Growing semiconductors with different lattice constants on top of each other results in strain and eventually in lattice dislocations when a critical layer thickness is exceeded. Preventing the dislocations from spreading to the active 2DEG region can be attempted by the growth of a buffer layer (either a thick strain-relaxed layer or a superlattice).

InAs is a popular 2DEG material that has also been explored quite extensively in the context of topological superconductivity. It was shown that the superconductor Al can be grown in situ (without breaking the vacuum) on top of the heterostructure, leading to a hard induced gap in the 2DEG [2–4]. This is an important achievement as the presence of subgap states is detrimental for the topological protection. To realize the hard induced gap, a thin top barrier (10 nm) was used such that the electron wave function can penetrate into the Al. The proximity to the surface, in turn, limits the electron mobility with typical values of 20 000 cm^2/Vs (measured in Hall bars with the Al removed) [4–7]. The linear Rashba spin-orbit parameter is found to be between 20 and 170 meVÅ [8] (280 meVÅ in [9]), and an effective g-factor of 10 is measured [9] (with the Al removed). Using the InAs/Al hybrid system, signatures of MZMs were reported [5–7, 10–14]. Their true topological origin however remains unclear. The main bottleneck of this material system is likely the disorder in the semiconductor, causing accidental zero-energy states and preventing the formation of an extended, uniform topological region.

In this thesis, two different Sb-based 2DEG materials are investigated: the binary semiconductor InSb and the ternary semiconductor InSbAs. A schematic of the InSb and InS-

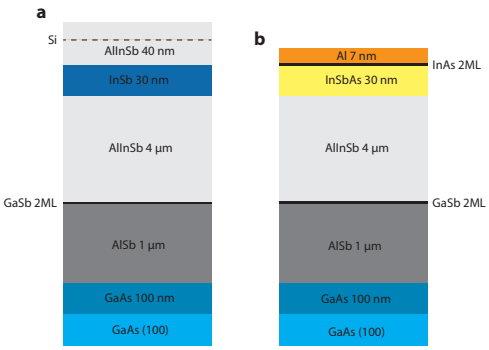

Figure 3.1: **a,** Layer stack of the InSb heterostructure. From bottom to top it consists of a semi-insulating GaAs substrate, a GaAs buffer layer, an AlSb nucleation layer, an InAlSb buffer layer that also serves as the bottom barrier for the quantum well, a 30 nm thick InSb layer and an InAlSb top barrier. A Si δ-doping layer is introduced 20 nm above the InSb layer to provide charge carriers. These 2DEGs can be proximitized by the ex situ deposited superconductor NbTiN as shown in chapter 4. **b,** Layer stack of the hybrid Al/InSbAs heterostructure used in chapter 5, 6 and 7. The thin Al layer is grown in situ (without breaking the vacuum) on top of the ternary semiconductor. The two monolayers (ML) of InAs are introduced to avoid an intermixing between Al and Sb [15].

bAs heterostructure, grown by MBE in the group of Prof. Michael Manfra at Purdue University, is shown in Fig. 3.1a and b, respectively. Compared to InAs, bulk InSb is known to have a larger electron mobility, stronger spin-orbit interaction and a significantly larger g-factor [16]. Measurements on buried 2DEGs (40 – 180 nm below the surface) report mobilities up to 300 000 cm^2/Vs [17], Rashba parameters between 30 meVÅ [18, 19] and 130 – 150 meVÅ [20, 21] (similar to InAs 2DEGs), and an effective g-factor of 25 – 50 [17, 19, 20, 22]. A disadvantage of InSb is that the device fabrication is more challenging (see chapter 3.2.1 for details). Particularly, there exist no systematic studies of induced superconductivity. In chapter 4, we overcome these issues and reliably induce superconductivity in InSb 2DEGs by coupling them to the ex situ deposited superconductor NbTiN.

Moving towards the realization of MZMs requires not only good semiconducting properties but also a clean semiconductor-superconductor interface. To this end, in situ grown Al on top of InSb 2DEGs is of great interest, similar to the achievements with InAs 2DEGs. Growing these hybrid 2DEGs, we find however that in situ grown Al does not proximitize InSb, even when grown directly on top of InSb (without top barrier). One possible reason for this is the band offset at the Al-InSb interface [23]. On the other hand, when incorporating small amounts of As in the semiconductor and thus forming the ternary semiconductor InSbAs, a strong proximity effect is observed as demonstrated in chapter 5.

Besides the feasibility of induced superconductivity, the ternary semiconductor InSbAs

has other advantageous properties. In fact, it has been realized a long time ago that the bandgap of InSbAs is tunable with the As concentration and that it can become the smallest direct gap among all III-V semiconductors, leading to applications in infrared emission and detection devices [24, 25]. The non-linear variation of the bandgap is often described by the bowing parameter (which assumes a perfectly random alloy), and different values for it are reported in literature. This spread might originate from strain effects that are believed to result in inaccuracies in determining the As concentration and in the formation of alloy ordering [25]. Interestingly, it was shown that in ordered InSbAs (particularly for CuPt ordering), the spin-orbit coupling can be enhanced significantly compared to InSb and InAs [26]. Furthermore, also in a randomly disordered alloy, such an enhancement remains in nanoscale devices (quantum dots or nanowires) [26]. Experimental evidence of increased spin-orbit coupling was found in InSbAs nanowires [27]. Calculations for InSbAs 2DEGs also predict such a tunabilty and further show that the effective g-factor for intermediate concentrations might be larger than the one for its binary constituents [28]. The material properties of ternary InSbAs/Al 2DEGs are studied chapter 5, while chapter 6 and 7 focus on planar JJs made in this material system.

Below we outline the device fabrication using InSb or InSbAs/Al 2DEGs, focusing on the key challenges for both of these material systems.

3.2. FABRICATION

3.2.1. PROCESSING OF INSB 2DEGS

The main challenge when processing InSb 2DEGs is to obtain good electrical contacts. It is well known that a Schottky barrier forms when contacting InSb with metals [29, 30]. Moreover, native oxides arise when exposing InSb to air [31]. The interface quality is particularly important when trying to induce superconductivity into InSb.

In order to contact InSb 2DEGs we tried several pre-treatment methods that aim to remove any oxides and locally dope the semiconductor. Among these were sulfur passivation and hydrofluoric acid dips. The downside of these methods is that they are ex situ and therefore oxides can grow back before the contact deposition. Using these methods we were not able to fabricate contacts reliably. In contrast, performing an in situ argon milling prior to the deposition of NbTiN in an ATC 1800-V sputtering system allowed us to create good contacts and even induce superconductivity into these 2DEGs. For optimizing the argon milling recipe, we monitored the contact resistivity extracted via the transmission line measurement technique for varying argon milling parameters (RF power, chamber pressure and milling time). We arrived at milling for 3 min using a power of 100 W and a pressure of 5 mTorr, resulting in contact resistivities below $100\,\Omega\cdot\mu$m.

Another consideration is the PMMA resist baking temperature. We found that the peak mobility, extracted from Hall bar measurements, drops by about 25 % when baking the samples at an elevated temperature of 175 °C compared to baking at 100 °C, see Fig. 3.2. The total baking time for the 175 °C device was 8 min, and 20 min for the 100 °C device.

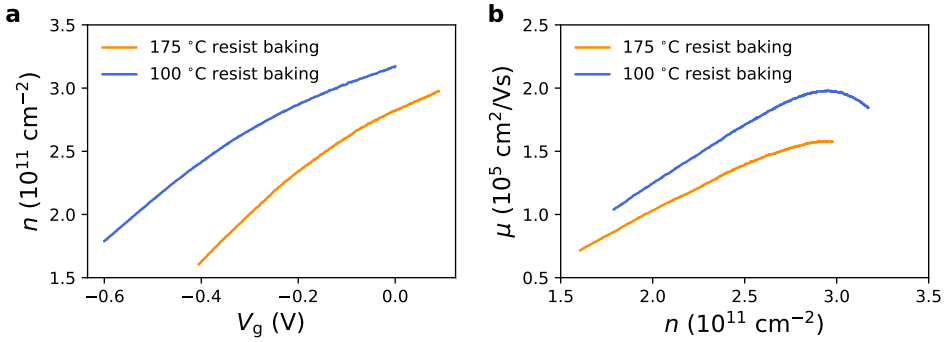

Figure 3.2: **a,** Electron density vs. gate voltage obtained from two gated Hall bars that were fabricated using different resist baking temperatures. Both devices were fabricated on chips from the same wafer (M06-13-17.1). **b,** Electron mobility vs. electron density. The peak mobility drops by about 25 % when using a baking temperature of 175 °C.

The full fabrication flow of devices such as Josephson junctions is described in detail in chapter 4. We will now turn to the processing of InSbAs/Al 2DEGs.

3.2.2. PROCESSING OF INSBAS/AL 2DEGS

The processing of InSbAs 2DEGs with in situ grown Al is challenging and requires several unconventional fabrication steps. This is because the Al can diffuse into the semiconductor through an exchange reaction, substituting In for Al, leading to a degradation of the interface and eventually to the consumption of the entire Al film. In order to avoid this as much as possible, two monolayers (ML) of InAs are grown between the Al and the InSbAs layer (see Fig. 3.1b) [15]. Figure 3.3 compares the surface evolution of an InSb/Al structure with and without InAs screening layer, demonstrating the enhanced durability when incorporating 2 ML of InAs. To minimize the interface degradation further, we perform most fabrication steps at room temperature (RT) since the exchange reaction is driven by temperature. Rather than baking the electron beam lithography resist on a hotplate to remove the solvent, we put the chip in a vacuum system for two hours. Moreover, we use cold acetone for metal liftoffs.

An important element for the intended planar JJ devices is to be able to perform tunneling spectroscopy at the junction's ends, which requires a stable dielectric. For this, a dedicated low-temperature atomic layer deposition (ALD) process in a new machine (Anric AT410) is developed. We optimize two recipes to deposit AlO_x at a temperature of 40 °C, one using water and the other one using ozone as the oxygen source. We adjust the parameters (amount of TMA and water/ozone precursor pulses, trapping time of precursors in the chamber, purge times) such that we are in the ALD saturation regime and have a complete removal of the precursor residues. We aim for a constant growth rate (GPC) around 1.0 Å/cycle and a uniform film thickness, measured across a 4-inch Si

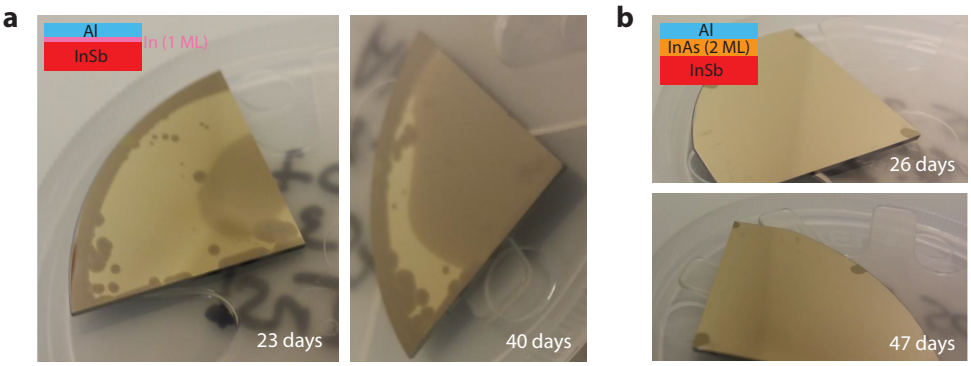

Figure 3.3: **a,** Optical images of an InSb/Al 2DEG, taken after the specified days after the growth. The wafer was stored in a nitrogen atmosphere at room temperature. Almost all Al is gone after 40 days. **b,** Surface evolution for a different wafer with 2 monolayers of InAs between the InSb and the Al. The Al is still intact after 47 days (same storage conditions). All images provided by Candice Thomas.

wafer. For the water recipe we arrive at a GPC very close to 1.0 Å/cycle with a thickness variation below 1 %, and for the ozone recipe we get a GPC of approximately 1.2 Å/cycle with a thickness variation below 5 %.

In Fig. 3.4 we compare the performance of the low-temperature ALD dielectric with a sputtered SiN_x dielectric (deposited at RT) when deposited on InSbAs devices. First, we check that the peak mobility of the 2DEG (extracted from gated Hall bars) remains unaffected, and find that this is indeed the case, see panel b. Note however that the nominal density decreases when using the AlO_x dielectric (panel a), suggesting a different band bending at the dielectric-semiconductor interface. Next, we confirm that the induced superconductivity remains in the 2DEG by measuring the supercurrent interference pattern in JJs. These JJs also have tunnel probes at the end of the junction (see schematic in panel c), allowing to measure the induced gap in the normal region of the JJ (panel d). Crucially, we obtain extremely clean tunneling spectroscopy maps when using the AlO_x dielectric, which is usually not the case for the SiN_x dielectric (cf. panel c). For more details about these measurements, we refer the reader to chapter 5, 6 and 7.

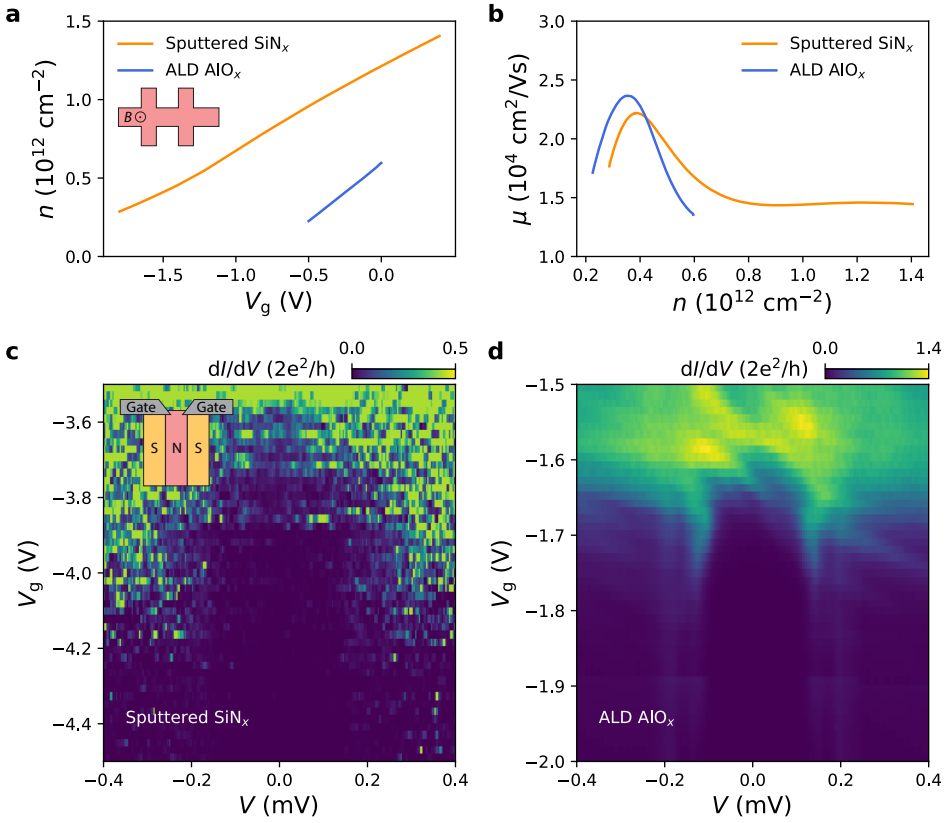

Figure 3.4: **a,** Electron density vs. gate voltage measured on two different gated Hall bars, one with a sputtered SiN_x dielectric and one with an ALD AlO_x dielectric. Both Hall bars were fabricated on a 2DEG with an As concentration of 13 %. **b,** Corresponding electron mobility vs. electron density. The peak mobilities are similar. **c,** Typical tunneling spectroscopy map obtained at the end of a Josephson junction when using sputtered SiN_x as the dielectric. When using the AlO_x dielectric instead, the spectroscopy maps are significantly cleaner, as shown in **d**.

REFERENCES

1. Sze, S. & Lee, M.-K. *Semiconductor Devices: Physics and Technology* (Wiley, Singapore, 2012).
2. Kjaergaard, M., Nichele, F., Suominen, H. J., Nowak, M. P., Wimmer, M., Akhmerov, A. R., Folk, J. A., Flensberg, K., Shabani, J., Palmstrøm, C. J. & Marcus, C. M. Quantized conductance doubling and hard gap in a two-dimensional semiconductor–superconductor heterostructure. *Nature Communications* **7,** 12841 (2016).
3. Kjaergaard, M., Suominen, H. J., Nowak, M. P., Akhmerov, A. R., Shabani, J., Palmstrøm, C. J., Nichele, F. & Marcus, C. M. Transparent Semiconductor-Superconductor Interface and Induced Gap in an Epitaxial Heterostructure Josephson Junction. *Phys. Rev. Applied* **7,** 034029 (2017).
4. Mayer, W., Yuan, J., Wickramasinghe, K. S., Nguyen, T., Dartiailh, M. C. & Shabani, J. Superconducting proximity effect in epitaxial Al-InAs heterostructures. *Applied Physics Letters* **114,** 103104 (2019).
5. Suominen, H. J., Kjaergaard, M., Hamilton, A. R., Shabani, J., Palmstrøm, C. J., Marcus, C. M. & Nichele, F. Zero-Energy Modes from Coalescing Andreev States in a Two-Dimensional Semiconductor-Superconductor Hybrid Platform. *Phys. Rev. Lett.* **119,** 176805 (2017).
6. Nichele, F., Drachmann, A. C. C., Whiticar, A. M., O'Farrell, E. C. T., Suominen, H. J., Fornieri, A., Wang, T., Gardner, G. C., Thomas, C., Hatke, A. T., Krogstrup, P., Manfra, M. J., Flensberg, K. & Marcus, C. M. Scaling of Majorana Zero-Bias Conductance Peaks. *Phys. Rev. Lett.* **119,** 136803 (2017).
7. Whiticar, A. M., Fornieri, A., O'Farrell, E. C. T., Drachmann, A. C. C., Wang, T., Thomas, C., Gronin, S., Kallaher, R., Gardner, G. C., Manfra, M. J., Marcus, C. M. & Nichele, F. Coherent transport through a Majorana island in an Aharonov–Bohm interferometer. *Nature Communications* **11,** 3212 (2020).
8. Wickramasinghe, K. S., Mayer, W., Yuan, J., Nguyen, T., Jiao, L., Manucharyan, V. & Shabani, J. Transport properties of near surface InAs two-dimensional heterostructures. *Applied Physics Letters* **113,** 262104 (2018).
9. Shabani, J., Kjaergaard, M., Suominen, H. J., Kim, Y., Nichele, F., Pakrouski, K., Stankevic, T., Lutchyn, R. M., Krogstrup, P., Feidenhans'l, R., Kraemer, S., Nayak, C., Troyer, M., Marcus, C. M. & Palmstrøm, C. J. Two-dimensional epitaxial superconductor-semiconductor heterostructures: A platform for topological superconducting networks. *Phys. Rev. B* **93,** 155402 (2016).

10. O'Farrell, E. C. T., Drachmann, A. C. C., Hell, M., Fornieri, A., Whiticar, A. M., Hansen, E. B., Gronin, S., Gardner, G. C., Thomas, C., Manfra, M. J., Flensberg, K., Marcus, C. M. & Nichele, F. Hybridization of Subgap States in One-Dimensional Superconductor-Semiconductor Coulomb Islands. *Phys. Rev. Lett.* **121,** 256803 (2018).

11. Fornieri, A., Whiticar, A. M., Setiawan, F., Portolés, E., Drachmann, A. C. C., Keselman, A., Gronin, S., Thomas, C., Wang, T., Kallaher, R., Gardner, G. C., Berg, E., Manfra, M. J., Stern, A., Marcus, C. M. & Nichele, F. Evidence of topological superconductivity in planar Josephson junctions. *Nature* **569,** 89–92 (2019).

12. Dartiailh, M. C., Mayer, W., Yuan, J., Wickramasinghe, K. S., Matos-Abiague, A., Žuti ć, I. & Shabani, J. Phase Signature of Topological Transition in Josephson Junctions. *Phys. Rev. Lett.* **126,** 036802 (2021).

13. Banerjee, A., Lesser, O., Rahman, M. A., Wang, H. .-., Li, M. .-., Kringhøj, A., Whiticar, A. M., Drachmann, A. C. C., Thomas, C., Wang, T., Manfra, M. J., Berg, E., Oreg, Y., Stern, A. & Marcus, C. M. Signatures of a topological phase transition in a planar Josephson junction. `https://arxiv.org/abs/2201.03453` (2022).

14. Banerjee, A., Lesser, O., Rahman, M. A., Thomas, C., Wang, T., Manfra, M. J., Berg, E., Oreg, Y., Stern, A. & Marcus, C. M. Local and Nonlocal Transport Spectroscopy in Planar Josephson Junctions. `https://arxiv.org/abs/2205.09419` (2022).

15. Thomas, C., Diaz, R. E., Dycus, J. H., Salmon, M. E., Daniel, R. E., Wang, T., Gardner, G. C. & Manfra, M. J. Toward durable Al-InSb hybrid heterostructures via epitaxy of 2ML interfacial InAs screening layers. *Phys. Rev. Materials* **3,** 124202 (2019).

16. Winkler, R. *Spin-Orbit Coupling Effects in Two-Dimensional Electron and Hole Systems* (Springer, Berlin, Heidelberg, 2003).

17. Lei, Z., Lehner, C. A., Rubi, K., Cheah, E., Karalic, M., Mittag, C., Alt, L., Scharnetzky, J., Märki, P., Zeitler, U., Wegscheider, W., Ihn, T. & Ensslin, K. Electronic *g* factor and magnetotransport in InSb quantum wells. *Phys. Rev. Research* **2,** 033213 (2020).

18. Kallaher, R. L., Heremans, J. J., Goel, N., Chung, S. J. & Santos, M. B. Spin-orbit interaction determined by antilocalization in an InSb quantum well. *Phys. Rev. B* **81,** 075303 (2010).

19. Lei, Z., Cheah, E., Rubi, K., Bal, M. E., Adam, C., Schott, R., Zeitler, U., Wegscheider, W., Ihn, T. & Ensslin, K. High-quality two-dimensional electron gas in undoped InSb quantum wells. *Phys. Rev. Research* **4,** 013039 (2022).

20. Khodaparast, G. A., Doezema, R. E., Chung, S. J., Goldammer, K. J. & Santos, M. B. Spectroscopy of Rashba spin splitting in InSb quantum wells. *Phys. Rev. B* **70,** 155322 (2004).

21. Gilbertson, A. M., Branford, W. R., Fearn, M., Buckle, L., Buckle, P. D., Ashley, T. & Cohen, L. F. Zero-field spin splitting and spin-dependent broadening in high-mobility InSb/$In_{1-x}Al_xSb$ asymmetric quantum well heterostructures. *Phys. Rev. B* **79,** 235333 (2009).

22. Qu, F., van Veen, J., de Vries, F. K., Beukman, A. J. A., Wimmer, M., Yi, W., Kiselev, A. A., Nguyen, B.-M., Sokolich, M., Manfra, M. J., Nichele, F., Marcus, C. M. & Kouwenhoven, L. P. Quantized Conductance and Large g-Factor Anisotropy in InSb Quantum Point Contacts. *Nano Lett.* **16,** 7509–7513 (2016).

23. Schuwalow, S., Schröter, N. B. M., Gukelberger, J., Thomas, C., Strocov, V., Gamble, J., Chikina, A., Caputo, M., Krieger, J., Gardner, G. C., Troyer, M., Aeppli, G., Manfra, M. J. & Krogstrup, P. Band Structure Extraction at Hybrid Narrow-Gap Semiconductor–Metal Interfaces. *Advanced Science* **8,** 2003087 (2021).

24. Vurgaftman, I., Meyer, J. R. & Ram-Mohan, L. R. Band parameters for III–V compound semiconductors and their alloys. *Journal of Applied Physics* **89,** 5815–5875 (2001).

25. Svensson, S. P., Sarney, W. L., Hier, H., Lin, Y., Wang, D., Donetsky, D., Shterengas, L., Kipshidze, G. & Belenky, G. Band gap of $InAs_{1-x}Sb_x$ with native lattice constant. *Phys. Rev. B* **86,** 245205 (2012).

26. Winkler, G. W., Wu, Q., Troyer, M., Krogstrup, P. & Soluyanov, A. A. Topological Phases in $InAs_{1-x}Sb_x$: From Novel Topological Semimetal to Majorana Wire. *Phys. Rev. Lett.* **117,** 076403 (2016).

27. Sestoft, J. E., Kanne, T., Gejl, A. N., von Soosten, M., Yodh, J. S., Sherman, D., Tarasinski, B., Wimmer, M., Johnson, E., Deng, M., Nygård, J., Jespersen, T. S., Marcus, C. M. & Krogstrup, P. Engineering hybrid epitaxial InAsSb/Al nanowires for stronger topological protection. *Phys. Rev. Materials* **2,** 044202 (2018).

28. Mayer, W., Schiela, W. F., Yuan, J., Hatefipour, M., Sarney, W. L., Svensson, S. P., Leff, A. C., Campos, T., Wickramasinghe, K. S., Dartiailh, M. C., Žutić, I. & Shabani, J. Superconducting Proximity Effect in InAsSb Surface Quantum Wells with In Situ Al Contacts. *ACS Applied Electronic Materials* **2,** 2351–2356 (2020).

29. Tiwari, S. & Frank, D. J. Empirical fit to band discontinuities and barrier heights in III–V alloy systems. *Applied Physics Letters* **60,** 630–632 (1992).

30. Fan, D., Kang, N., Ghalamestani, S. G., Dick, K. A. & Xu, H. Q. Schottky barrier and contact resistance of InSb nanowire field-effect transistors. **27,** 275204 (2016).

31. Smirnova, T., Golubenko, A., Zacharchuk, N., Belyi, V., Kokovin, G. & Valisheva, N. Phase composition of thin oxide films on InSb. *Thin Solid Films* **76,** 11–22 (1981).

4

BALLISTIC SUPERCONDUCTIVITY AND TUNABLE π-JUNCTIONS IN INSB QUANTUM WELLS

Chung Ting Ke*, Christian M. Moehle*, Folkert K. de Vries, Candice Thomas, Sara Metti, Charles R. Guinn, Ray Kallaher, Mario Lodari, Giordano Scappucci, Tiantian Wang, Rosa E. Diaz, Geoffrey C. Gardner, Michael J. Manfra, Srijit Goswami

Planar Josephson junctions (JJs) made in semiconductor quantum wells with large spin-orbit coupling are capable of hosting topological superconductivity. Indium antimonide (InSb) two-dimensional electron gases (2DEGs) are particularly suited for this due to their large Landé g-factor and high carrier mobility, however superconducting hybrids in these 2DEGs remain unexplored. Here we create JJs in high quality InSb 2DEGs and provide evidence of ballistic superconductivity over micron-scale lengths. A Zeeman field produces distinct revivals of the supercurrent in the junction, associated with a $0-\pi$ *transition. We show that these transitions can be controlled by device design, and tuned in-situ using gates. A comparison between experiments and the theory of ballistic* π*-Josephson junctions gives excellent quantitative agreement. Our results therefore establish InSb quantum wells as a promising new material platform to study the interplay between superconductivity, spin-orbit interaction and magnetism.*

This chapter has been published in Nature Communications 10, 3764 (2019).

*These authors contributed equally to this work.

4.1. INTRODUCTION

Two-dimensional electron gases (2DEGs) coupled to superconductors offer the opportunity to explore a variety of quantum phenomena. These include the study of novel Josephson effects [1], superconducting correlations in quantum (spin) Hall systems [2–7], hybrid superconducting qubits [8, 9] and emergent topological states in semiconductors with strong spin-orbit interaction (SOI) [10–13]. Topological superconductivity in such 2DEGs can be realized using planar Josephson junctions (JJs), where the combined effect of SOI and a Zeeman field is known to significantly alter the current-phase relation [14–16]. In particular, one expects a complete reversal of the supercurrent (i.e., a π-JJ) [17–19] when the Zeeman and Thouless energy of the system become comparable. It was shown recently that such a 0–π transition in a 2D system is in fact accompanied by a topological phase transition [12, 13, 20, 21]. This, combined with the promise of creating scalable topological networks [22–24], provides a strong motivation to study induced superconductivity in 2DEGs.

Key requirements for the semiconductor include low disorder, large SOI and a sizable Landé g-factor, combined with the ability to grow it on the wafer scale. InSb satisfies all of these requirements [25–28] and has emerged as a prime material candidate for engineering topological superconductivity, as evident from nanowire-based systems [29, 30]. However, despite significant progress in the growth of InSb 2DEGs [31, 32], material challenges have prevented a systematic study of the superconducting proximity effect in these systems.

Here, we overcome these issues and reliably create JJs, thus providing evidence of induced superconductivity in high quality InSb quantum wells. The JJs support supercurrent transport over several microns and display clear signatures of ballistic superconductivity. Furthermore, we exploit the large g-factor and gate tunability of the junctions to control the current-phase relation, and drive transitions between the 0 and π-states. This control over the free energy landscape allows us to construct a phase diagram identifying these 0 and π-regions, in agreement with theory.

4.2. INDUCED SUPERCONDUCTIVITY IN INSB 2DEGS

The JJs are fabricated in an InSb 2DEG wafer grown by molecular beam epitaxy, with a nominal electron density $n = 2.7 \cdot 10^{11}$ cm^{-2} and mobility $\mu \approx 150{,}000$ cm^{2}V^{-1}s^{-1}, which corresponds to a mean free path $l_e \approx 1.3$ μm. Figure 4.1a shows a cross-sectional illustration and scanning electron micrograph of a typical JJ. Following a wet etch of the 2DEG in selected areas, NbTiN is deposited to create side-contacts to the 2DEG, thus defining a JJ of width W and length L. Prior to sputtering NbTiN, an in-situ argon plasma cleaning of the exposed quantum well is performed in order to obtain good electrical contacts. A metal top-gate, deposited on a thin dielectric layer is used to modify the electron density in the JJ. Details of the device fabrication and wafer growth can be found in the Methods section.

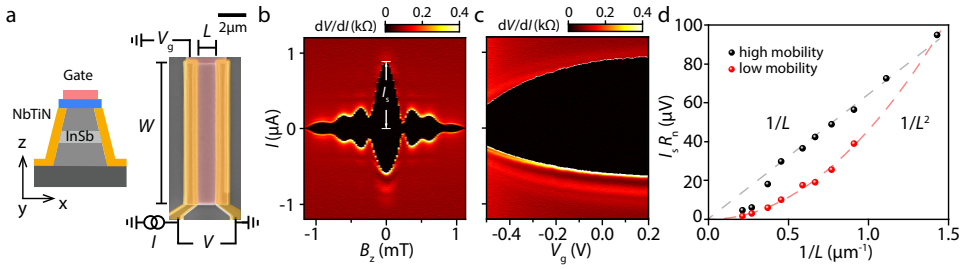

Figure 4.1: Ballistic superconductivity in InSb 2DEGs. **a,** Cross-sectional schematic and false-colored scanning electron micrograph (along with a measurement schematic) of a top-gated JJ of width W and length L. **b,** Differential resistance, $\mathrm{d}V/\mathrm{d}I$, versus perpendicular magnetic field, B_z, and current bias, I, displaying a Fraunhofer-like interference pattern for a JJ with $W = 9.7$ μm, $L = 1.1$ μm. White line indicates the magnitude of the switching current, I_s, at zero magnetic field. **c,** $\mathrm{d}V/\mathrm{d}I$ as a function of I and gate voltage, V_g, for the same JJ, showing gate control of I_s. **d,** Length dependence of $I_s R_n$ for JJs on a high mobility (black dots) and low mobility (red dots) wafer, obtained at $V_g = 0$ V. Dashed lines are $1/L$ and $1/L^2$ fits to the data, indicating ballistic and diffusive transport, respectively.

The junctions are measured using a quasi-four terminal current-biased circuit (Fig. 4.1a) at a temperature of 50 mK. We observe a clear supercurrent branch with zero differential resistance, $\mathrm{d}V/\mathrm{d}I$, followed by a jump to the resistive branch at switching current, I_s. In small perpendicular magnetic fields, B_z, Fraunhofer-like interference patterns are observed, as seen in Fig. 4.1b. The magnitude of supercurrent is controlled using the gate (Fig. 4.1c). Lowering the gate voltage, V_g, leads to a reduction of the electron density in the 2DEG and therefore to a suppression of I_s and an increase in the normal state resistance, R_n. In addition, we observe multiple Andreev reflections indicating an induced superconducting gap of 0.9 meV, and excess current measurements allow us to estimate transparencies in the range of 0.6-0.7 (representative data is provided in the Supplementary Note 2).

4.3. BALLISTIC SUPERCONDUCTIVITY

Studying JJs of varying lengths ($L = 0.7 - 4.7$ μm), we gain insight into the transport regime. These devices fall in the long junction limit, since their lengths exceed the induced superconducting coherence length of around 500 nm (see Supplementary Note 2). In this limit the product of the critical current, I_c, and R_n is proportional to the Thouless energy [33], $E_{Th} = \hbar v_F l_e / 2L^2$, where v_F is the Fermi velocity in the 2DEG. Thus, for ballistic (diffusive) transport where $l_e = L$ ($l_e < L$), we expect $I_c R_n$ to scale as $1/L$ ($1/L^2$). Figure 4.1d shows $I_s R_n$ [34] for a set of JJs. We find a $1/L$ scaling (black dots) indicative of ballistic superconductivity, with deviations only for the longer ($L \geq 2.7$ μm) junctions. Such a $1/L$ dependence was predicted decades ago [35] but has only recently been experimentally observed over micron-scale lengths in clean graphene-based JJs [36, 37].

To confirm the scaling arguments we also include data from a lower mobility wafer (see Supplementary Note 1) with $l_e \approx 0.5$ μm (red dots) and find a $1/L^2$ scaling, consistent with diffusive behavior. In the remainder of this work we focus on JJs fabricated on the high mobility wafer.

4.4. $0-\pi$ TRANSITIONS IN JOSEPHSON JUNCTIONS

Using these ballistic junctions, we now explore their response to a Zeeman field. The theory of JJs with large SOI subjected to a magnetic field has been discussed extensively [14, 17, 20]. Below we briefly describe the essential elements of the physical picture. At zero B the Fermi surfaces are split due to the Rashba SOI (solid lines of Fig. 4.2a inset). The magnetic field then splits the bands by the Zeeman energy, $E_Z = g\mu_B B$, leading to a shift in the Fermi surfaces by $\pm\delta k/2$. The depicted shift of the Fermi surfaces assumes that the spin-orbit energy dominates over the Zeeman energy, which is indeed the case for the measured JJs (see Supplementary Note 3 for a detailed discussion). Therefore, Cooper pairs (electrons with opposite momentum and spin) now possess a finite momentum, given by $\mathbf{k}_F \cdot \delta\mathbf{k} = E_Z(m^*/\hbar^2)$, where $\mathbf{k}_F$ is the Fermi momentum and m^* the effective mass. This translates to a phase acquired by the superconducting order parameter along the direction of current flow, $\Psi(\mathbf{r}) \propto \cos(\delta\mathbf{k}\cdot\mathbf{r})$ [38–40]. Depending on the length of the Cooper pair trajectories, $|\mathbf{r}|$, the order parameter is either positive or negative, corresponding to the ground state of the JJ being at 0 or π superconducting phase difference, respectively. This oscillation of the order parameter results in a modulation of the critical current $I_c \propto |\Psi|$, where a minimum of I_c is expected whenever the order parameter switches sign [14, 15]. Taking only trajectories perpendicular to the contacts ($\delta\mathbf{k} = \delta k\hat{\mathbf{x}}$, $\mathbf{k}_F = k_F\hat{\mathbf{x}}$), a JJ with length L will display minima in I_c when $L\delta k = (2N+1)\pi/2$, with $N = 0, 1, 2...$ The condition for the first minimum ($N = 0$) can be expressed as a resonance condition in terms of the Zeeman and ballistic Thouless energy as $E_Z = \pi E_{Th}$ giving:

$$g\mu_B B = \pi \frac{\hbar^2\sqrt{2\pi n}}{m^* 2L}. \tag{4.1}$$

The $0-\pi$ transition therefore depends on three experimentally accessible parameters: 1) applied magnetic field, 2) length of the JJ and 3) carrier density. In the following, we demonstrate independent control of each of these parameters, allowing for a complete study of the free energy landscape of the junctions.

4.5. MAGNETIC FIELD-DRIVEN $0-\pi$ TRANSITIONS

We start by varying B_y, while n (controllable by V_g) and L remain fixed. The orientation of the magnetic field reflects the Fermi surfaces described, and avoids unwanted geometric effects [41]. Figure 4.2a shows the expected oscillation of I_s with increasing B_y, displaying two distinct minima at $B_y = 470$ mT and $B_y = 1250$ mT (see Supplementary Note 4 for details about magnetic field alignment). This behavior is consistent with a

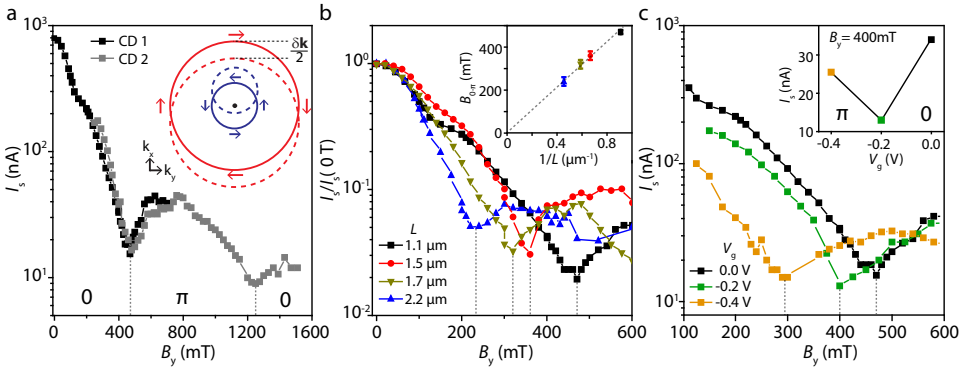

Figure 4.2: Magnetic field-driven 0–π transitions. **a,** Variation of the switching current, I_s, with in-plane magnetic field, B_y, at $V_g = 0$ V for the same JJ as in Fig. 4.1b,c. Two distinct revivals of I_s are visible at $B_y = 470$ mT and 1250 mT, associated with 0–π transitions. The data is from two cool downs (CDs). The momentum shift, $\delta k/2$, of the Fermi surfaces due to the Zeeman field is sketched in the inset. The solid (dashed) lines depict the situation at zero (finite) magnetic field, and the arrows represent the spin orientation. **b,** I_s as a function of B_y at $V_g = 0$ V for four JJs with different lengths. For better visibility, I_s is normalized with respect to I_s at $B_y = 0$ T. Dashed lines indicate $B_{0-\pi}$, the field at which the transition occcurs for each length. The inset shows a linear dependence of $B_{0-\pi}$ on $1/L$, in agreement with ballistic transport. **c,** I_s vs. B_y at three different V_g for the JJ with $L = 1.1$ μm. $B_{0-\pi}$ shifts to lower values of B_y with more negative gate voltages. I_s vs. V_g at $B_y = 400$ mT shows a non-monotonic behavior as displayed in the inset. The length and gate dependence of panel **b** and **c** are in qualitative agreement with Eq. 4.1.

magnetic field driven 0–π transition, as discussed above, where the first (second) minimum corresponds to a transition of the JJ state from 0 to π (π to 0). This interpretation is corroborated by the occurrence of the second minimum at a field value which is approximately three times larger than the first. Note that this is incompatible with a Fraunhofer interference pattern that might arise from the finite thickness of the 2DEG. Furthermore, taking into account the gate dependence of the transition and other geometric considerations (discussed in detail in the Supplementary Note 5) allows us to conclusively rule out such a mechanism for the supercurrent modulation.

Next, we investigate how the length of the JJ influences $B_{0-\pi}$, the magnetic field at which the transition occurs. Figure 4.2b presents the I_s oscillation for JJs with four different lengths, showing that $B_{0-\pi}$ is systematically reduced for increasing L. Plotting $B_{0-\pi}$ with respect to $1/L$ (inset of Fig. 4.2b), we find a linear dependence as expected from Eq. 4.1. The transition points are therefore determined by the ballistic E_{Th}, consistent with the conclusions from Fig. 4.1d. Finally, we check the dependence of the transition on the electron density. In Fig. 4.2c, we plot I_s versus B_y for different gate voltages using a JJ with $L = 1.1$ μm. As V_g is lowered, $B_{0-\pi}$ shifts to smaller values, again in qualitative agreement with Eq. 4.1. Interestingly, above a certain magnetic field the state of the JJ (0 or π)

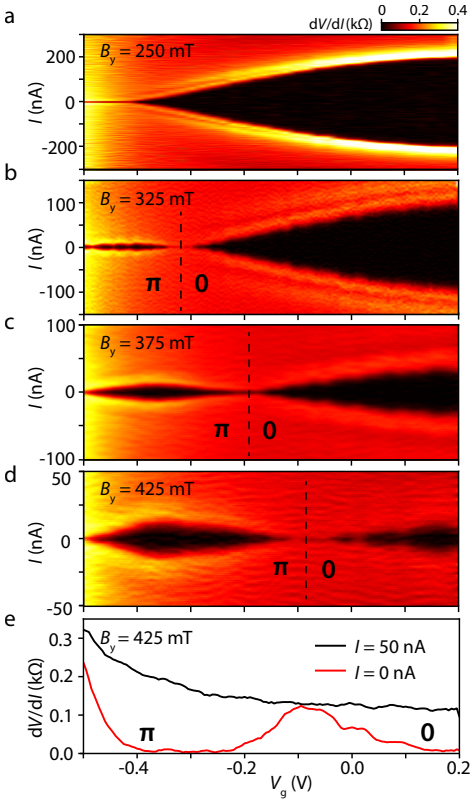

Figure 4.3: Gate-driven $0-\pi$ transitions. **a-d,** $\mathrm{d}V/\mathrm{d}I$ as a function of I and V_g for several B_y as indicated. From $B_y = 325$ mT onward, a gate-driven $0-\pi$ transition becomes evident, characterized by a re-emergence of I_s with decreasing V_g. As expected, the transition shifts to higher gate voltages with increasing B_y (see SI for sweeps at additional values of the magnetic field). **e,** Line-cuts through panel **d** at $I = 50$ nA (black) and $I = 0$ nA (red). The low bias trace reveals the $0-\pi$ transition whereas the high bias trace shows a monotonic behavior.

becomes gate-dependent. For example at $B_\mathrm{y} = 400$ mT, the junction changes from a 0-JJ ($V_\mathrm{g} = 0$ V) to a π-JJ ($V_\mathrm{g} = -0.4$ V), with a transition at $V_\mathrm{g} = -0.2$ V. This indicates the feasibility of tuning the JJ into the π-state using gate voltages, while the magnetic field remains fixed.

4.6. GATE-DRIVEN $0-\pi$ TRANSITIONS

These gate-driven transitions are demonstrated in Fig. 4.3a-d, which show a sequence of $I - V_\mathrm{g}$ plots for increasing in-plane magnetic fields. At $B_\mathrm{y} = 250$ mT, I_s displays a monotonic reduction with decreasing V_g. At a higher magnetic field, $B_\mathrm{y} = 325$ mT, I_s

reveals a markedly different behavior, whereby the supercurrent first decreases and then (at $V_g = -0.32$ V) shows a clear revival, indicative of a gate-driven $0-\pi$ transition, where the resonance condition ($E_Z = \pi E_{Th}$) is achieved by tuning the electron density. Increasing B_y further, continuously moves the transition point to higher gate voltages (larger density), perfectly in line with expectations for a $0-\pi$ transition. Figure 4.3e shows two line-cuts from Fig. 4.3d. At zero current bias, dV/dI shows a clear peak, indicative of a reentrance of the supercurrent due to the the $0-\pi$ transition. However, at high bias, dV/dI increases monotonically, similar to the response at zero magnetic field. This eliminates trivial interference effects as an explanation for the supercurrent modulation, where one would expect a correlation between the two curves [36, 42, 43].

4

4.7. CONSTRUCTION OF THE 0−π PHASE DIAGRAM

In contrast to the field-driven measurements (Fig. 4.2), controlling the transition with a gate avoids the need for time-consuming field alignment procedures, thus allowing us to efficiently explore a large parameter space in magnetic field and gate voltage. We now combine these results to construct a $0-\pi$ phase diagram of the JJ. The combination of a high quality 2DEG and relatively long devices results in well defined magnetoresistance oscillations, allowing us to directly extract the electron density in the junction. Figure 4.4a shows the Landau fan diagram in perpendicular magnetic fields, B_z, from which we identify the filling factors, $\nu = nh/eB_z$ (Fig. 4.4b), and thereby obtain the n vs. V_g curve (Fig. 4.4c). We then plot all the transition points in Fig. 4.4d. The axes represent the two important energy scales in the system ($B_y \propto E_Z$ and $\sqrt{n} \propto E_{Th}$), thereby highlighting the 0 and π regions in the phase space. Finally, we compare our results with the theory of ballistic JJs represented by Eq. 1. To do so, we independently extract the effective mass (see Supplementary Note 7), $m^* = (0.022 \pm 0.002)m_e$, and fit the data to a single free parameter, g_y (the in-plane g-factor), giving $g_y = 25 \pm 3$ in good agreement with previous measurements on similar InSb quantum wells [28].

4.8. CONCLUSION

Our work provides the first evidence of induced superconductivity in high quality InSb 2DEGs and demonstrates the creation of robust, gate-tunable π-Josephson junctions. We show that the $0-\pi$ transition can be driven both by magnetic fields and gate voltages. The significant region of phase space where the π-JJ is stable could prove advantageous in the study of topological superconductivity in planar JJs [12, 13, 20, 21]. Moreover, these large SOI 2DEGs, in conjunction with our magnetic field compatible superconducting electrodes and clear Landau quantization, would also be excellent candidates to realize topological junctions in the quantum Hall regime [7]. Finally, the ability to control the ground state between 0 and π states using gates is analogous to recent experimental results in ferromagnetic JJs [44], and could possibly serve as a semiconductor-based platform for novel superconducting logic applications [45]. We therefore establish InSb 2DEGs as a new, scalable platform for developing hybrid superconductor-semiconductor technologies.

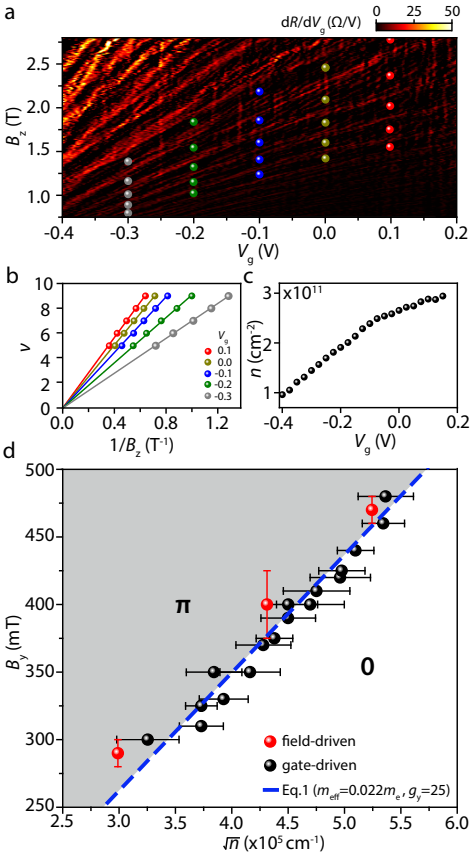

Figure 4.4: 0–π phase diagram. **a,** Landau fan diagram for the JJ with $L = 1.1\ \mu$m, showing the transresistance ($\mathrm{d}R/\mathrm{d}V_\mathrm{g}$) as a function of B_z and V_g. The symbols indicate positions of integer filling factors ν at specific values of V_g. **b,** Dependence of ν on $1/B_\mathrm{z}$ along with linear fits used to extract the electron density, $n(V_\mathrm{g})$, presented in **c**. **d,** Phase diagram of the 0–π transition as a function of $B_\mathrm{y} \propto E_\mathrm{Z}$ and $\sqrt{n} \propto E_\mathrm{Th}$, containing all data points obtained from both field-driven (red) and gate-driven (black) 0–π transitions. For the error analysis, see SI. We fit the data to Eq. 4.1 (blue line) with g_y as a fitting parameter.

4.9. METHODS

4.9.1. WAFER GROWTH

InSb-based 2DEGs were grown on semi-insulating GaAs (100) substrates by molecular beam epitaxy in a Veeco Gen 930 using ultra-high purity techniques and methods as described in Ref. [46]. The layer stack of the heterostructure is shown in Supplementary Fig. 1a. The growth has been initiated with a 100 nm thick GaAs buffer followed by a 1 μm thick AlSb nucleation layer. The metamorphic buffer is composed of a superlattice of 300 nm thick $In_{0.91}Al_{0.09}Sb$ and 200 nm thick $In_{0.75}Al_{0.25}Sb$ layers, repeated 3 times,

and directly followed by a 2 μm thick $In_{0.91}Al_{0.09}Sb$ layer. The active region consists of a 30 nm thick InSb quantum well and a 40 nm thick $In_{0.91}Al_{0.09}Sb$ top barrier. The Si δ-doping layer has been introduced at 20 nm from the quantum well and the surface. The $In_xAl_{1-x}Sb$ buffer, the InSb quantum well and the $In_xAl_{1-x}Sb$ setback were grown at a temperature of 440 °C under a p(1x3) surface reconstruction. The growth temperature was lowered to 340 °C, where the surface reconstruction changed to c(4x4), just before the δ-doping layer, to facilitate Si incorporation [47]. The scanning transmission electron micrograph of Supplementary Fig. 1b reveals the efficiency of the metamorphic buffer to filter the dislocations.

4.9.2. DEVICE FABRICATION

The devices are fabricated using electron beam lithography. First, mesa structures are defined by etching the InSb 2DEG in selected areas. We use a wet etch solution consisting of 560 ml deionized water, 9.6 g citric acid powder, 5 ml H_2O_2 and 7 ml H_3PO_4, and etch for 5 min, which results in an etch depth around 150 nm. This is followed by the deposition of superconducting contacts in an ATC 1800-V sputtering system. Before the deposition, we clean the InSb interfaces in an Ar plasma for 3 min (using a power of 100 W and a pressure of 5 mTorr). Subsequently, without breaking the vacuum, we sputter NbTi (30 s) and NbTiN (330 s) at a pressure of 2.5 mTorr, resulting in a layer thickness of approximately 200 nm. Next, a 45 nm thick layer of AlO_x dielectric is added by atomic layer deposition at 105 °C, followed by a top-gate consisting of 10 nm/170 nm of Ti/Au.

AUTHOR CONTRIBUTIONS

C. T. K. and **C. M. M.** fabricated and measured the devices. C. T., G. C. G. and M. J. M. designed and grew the semiconductor heterostructures. C. T., S. M., C. R. G., R. K., T. W., R. E. D., G. C. G., and M. J. M. characterized the materials. M. L. and G. S. provided the effective mass measurements. C. T. K., **C. M. M.**, F. K. d. V. and S. G. performed the data analysis. The manuscript was written by C. T. K., F. K. d. V., **C. M. M.**, and S. G., with input from all co-authors. S. G. supervised the project.

DATA AVAILABILITY

All data files are available at 4TU.ResearchData repository, DOI: 10.4121/uuid:5fab8273-8794-4cd7-96d4-ba8ec00a62cf

ACKNOWLEDGMENTS

We thank Ady Stern, Attila Geresdi and Michiel de Moor for useful discussions. The research at Delft was supported by the Dutch National Science Foundation (NWO) and a TKI grant of the Dutch topsectoren program. The work at Purdue was funded by Microsoft Quantum.

4.10. SUPPLEMENTARY MATERIAL

4.10.1. WAFER GROWTH AND CHARACTERIZATION

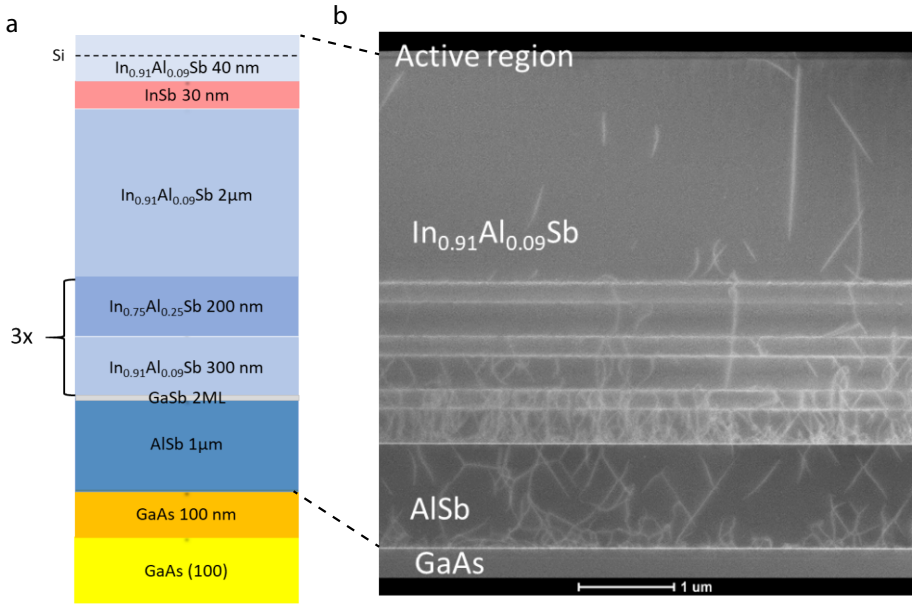

Figure 4.5: InSb quantum well. **a,** Layer stack of the InSb/GaAs heterostructure, where the layer constituents and thicknesses are indicated. **b,** Scanning transmission electron micrograph of the structure of Supplementary Fig. 1a obtained in High Angle Annular Dark Field Mode along the [110] zone axis.

The wafer is characterized by measuring the (quantum) Hall effect in a Hall bar geometry at $T = 300$ mK. From a linear fit to the transversal resistance in a magnetic field range up to 1 T, we extract an electron density $n = 2.71 \cdot 10^{11}$ cm^{-2}, and by using the longitudinal resistivity at zero field, we obtain a mobility $\mu = 146,400$ cm^{2}V^{-1}s^{-1} (see Supplementary Table I). We calculate the corresponding mean free path to be $l_e = 1.26$ μm. In Supplementary Table 1, we also include n, μ and l_e for the low mobility wafer, obtained from a quantum Hall measurement on this wafer. Data from the low mobility wafer is shown in Fig. 1d of the main text.

	High mobility wafer	Low mobility wafer
n (cm^{-2})	$2.71 \cdot 10^{11}$	$2.71 \cdot 10^{11}$
μ (cm^2/Vs)	146,400	61,500
l_e (μm)	1.26	0.53

Table 4.1: Electron density, mobility and mean free path for the high and low mobility wafer, obtained from quantum Hall measurements at $T = 300$ mK.

4.10.2. MULTIPLE ANDREEV REFLECTIONS AND EXCESS CURRENT

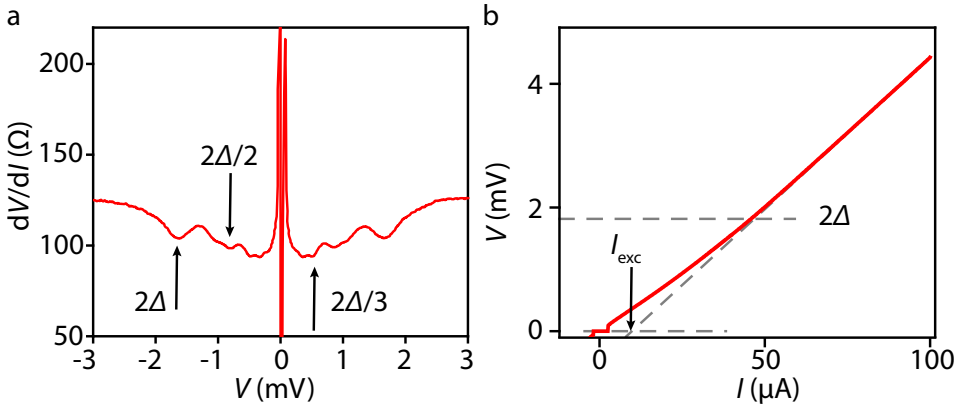

Figure 4.6: Josephson junction characterization. **a,** Differential resistance, $\mathrm{d}V/\mathrm{d}I$, as a function of bias voltage, V, showing multiple Andreev reflections. Three dips at $V = 2\Delta, 2\Delta/2$ and $2\Delta/3$ are highlighted. **b,** Voltage measured as a function of bias current. The excess current, I_{exc}, and $V = 2\Delta$ are indicated.

To further characterize the superconductivity in our JJs, we study multiple Andreev reflections (MAR) in a representative JJ, by measuring its differential resistance, $\mathrm{d}V/\mathrm{d}I$, as a function of applied bias voltage, V. In Supplementary Fig. 4.6a, we observe three dips in $\mathrm{d}V/\mathrm{d}I$, the first, at 2Δ, corresponding to the coherence peaks of the superconducting density of states, and two MAR peaks at $2\Delta/2$ and $2\Delta/3$. From these peaks we extract an induced superconducting gap $\Delta = 0.9$ meV. In addition, we estimate the transparancy of the same JJ by measuring its excess current, I_{exc}, and normal state resistance, R_{n}. This measurement is shown in Supplementary Fig. 4.6b, where we perform a linear fit in the high bias region of the $I - V$ curve ($V > 2\Delta$) and obtain $I_{\mathrm{exc}} = 9$ μA and $R_{\mathrm{n}} = 50$ Ω. Using the OBTK model [48], we find a value of 0.62 for the transparency of the JJ. These transparencies are moderate compared to, for example, hybrid devices made with epitaxial interfaces between Aluminum and InAs 2DEGs [49]. In fact, recent work has shown that high quality interfaces can even be made between Aluminum and InSb wires [30, 50, 51]. We expect that similar materials developments with InSb 2DEGs would enable strong

proximity coupling, an important requirement for exploring topological superconductivity in these systems.

4.10.3. WEAK ANTI-LOCALIZATION AND SPIN-ORBIT INTERACTION ENERGY

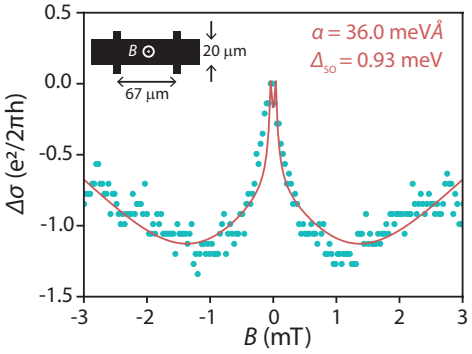

Figure 4.7: Weak anti-localization analysis. Measured longitudinal conductivity difference, $\Delta\sigma$, as a function of magnetic field, B, displaying a weak anti-localization peak around zero field. We fit (red) the data (cyan) using the ILP model and extract the SOI energy at the Fermi energy, Δ_{SO}, from which we calculate the Rashba spin-orbit parameter α. The inset shows a schematic of the Hall bar device, indicating its length and width, and the magnetic field direction.

To obtain an estimate of the typical energy scale associated with the spin-orbit interaction, we performed weak anti-localization (WAL) measurements. We use a Hall bar device (inset Supplementary Fig. 4.7) fabricated on the high mobility wafer (Supplementary Fig. 4.5), and apply magnetic field perpendicular to the Hall bar. The measurement in Supplementary Fig. 4.7 reveals the typical WAL peak around zero field. This peak is caused by suppression of coherent backscattering at small magnetic fields due to the spin-orbit interaction. As we expect the Dyakonov Perel scattering mechanism to be dominating in our high mobility wafer, we use the theory developed by Iordanskii, Lyanda-Geller and Pikus [52] to fit the data:

$$\frac{\Delta\sigma(B)}{e^2/2\pi h} = -\frac{1}{a} - \frac{2a_0+1+H_s}{a_1(a_0+H_s-2H_s)} - 2\ln H_{tr} - \Psi\left(1/2+H_\phi\right) - 3C + \sum_{n=1}^{\infty}\left[\frac{3}{n} - \frac{3a_n^2+2a_nH_s-1-2(2n+1)H_s}{(a_n+H_s)a_{n-1}a_{n+1}-2H_s[(2n+1)a_n-1]}\right],$$

where Ψ is the Digamma function, C the Euler constant, and

$$a_n = n+\frac{1}{2}+H_\phi+H_s \qquad H_{tr,\phi,s} = \frac{\hbar}{4eDB\tau_{tr,\phi,s}} \qquad \Delta_{SO} = \sqrt{\frac{2\hbar^2}{\tau_{tr}\tau_s}},$$

with $D = v_F l_e/2$, and $\tau_{tr,\phi,s}$ the scattering times for elastic, inelastic and spin-orbit scattering, respectively. We find a spin-orbit energy splitting at the Fermi level (Δ_{SO}) of 0.93 meV. The Rashba spin-orbit parameter of $\alpha = 36$ meVÅ is calculated following $\alpha = \Delta_{SO}/k_F$, where k_F is deduced from a classical Hall measurement. Finally, we compare Δ_{SO} to the Zeeman energy. For a Landé g-factor of 25, $\Delta_{SO} > E_Z$ up to 640 mT. We are therefore in the spin-orbit dominated regime for the $0-\pi$ transition.

4.10.4. MAGNETIC FIELD ALIGNMENT

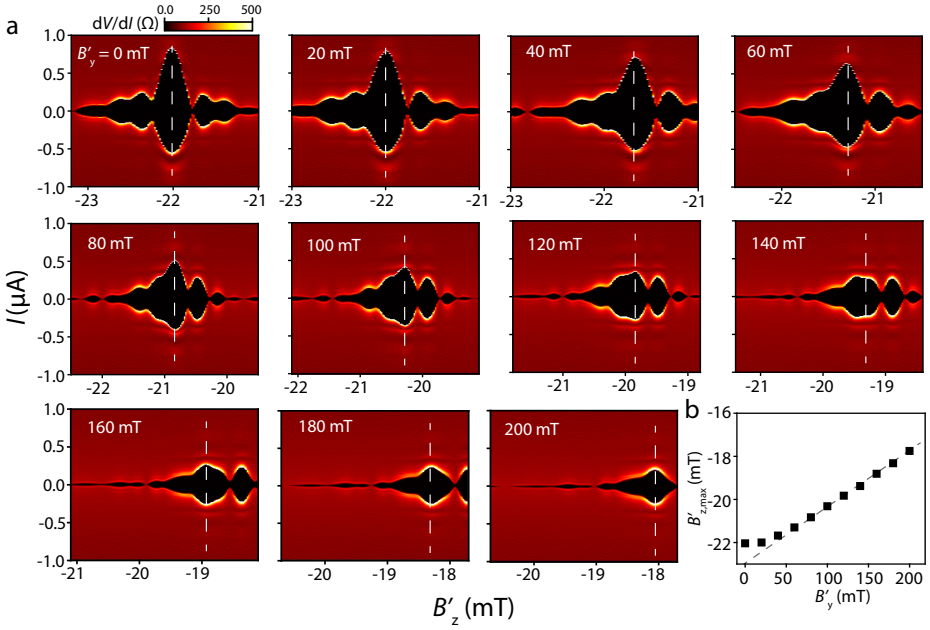

Figure 4.8: Field alignment. **a,** Differential resistance, dV/dI maps as a function of current bias, I, and out-of-plane magnetic field, B'_z, with increasing in-plane magnetic field, B'_y, in steps of 20 mT. We track the central lobe of the interference pattern, labeled by white dash lines, to obtain $B_{z,max}$. **b,** The $B'_{z,max}$ vs. B'_y dependence showing the small perpendicular component of B'_y.

To ensure we are sweeping the magnetic field in the plane of the JJs only, we characterize the misalignment of our vector magnet axes, B'_y and B'_z, used to apply the magnetic field in-plane and out-of-plane of the JJ, B_y and B_z. In Supplementary Fig. 4.8a we present a systematic measurement of the Fraunhofer interference pattern induced by B'_z with increasing B'_y. We track the magnetic field at which the central lobe reaches its maximum I_s, $B'_{z,max}$ and plot this for all B'_y in Supplementary Fig. 4.8b. The linear dependence observed, represents a small misalignment angle of $\theta = 1.4°$. We take this angle into account when sweeping the in-plane field, $B_y = \cos(\theta)B'_y + \sin(\theta)B'_z$, and disregard it for the

out-of-plane direction, $B_z = B'_z$.

At larger magnetic fields the patterns become asymmetric. This asymmetry has two possible origins which we expect to coexist in our samples. The first is the effect of magnetic vortices which nucleate in our type II superconductor (NbTiN) at moderate magnetic fields. The second has to do with terms in the Hamiltonian that break mirror symmetry of the potential in the JJ (e.g., small amounts of disorder at the interface) [53]. To ensure that these asymmetries do not influence our extraction of I_s or the magnetic field at which it revives, we performed two separate cooldowns (Fig. 2a in the main text) and confirmed that the results are in agreement. The large offset observed at zero in-plane magnetic field is a trivial offset from the magnet power supply which we have corrected for in Fig. 1c of the main text.

4

4.10.5. IN-PLANE INTERFERENCE CONSIDERATIONS

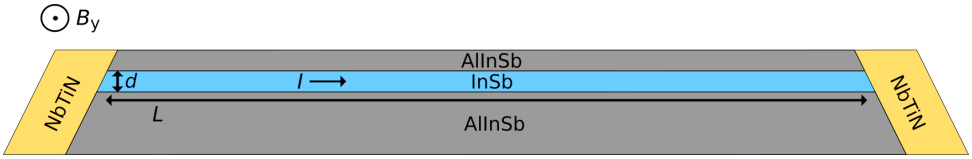

Figure 4.9: Schematic of quantum well. Cross-sectional illustration of the InSb quantum well for a JJ with $L = 1.1$ μm and $d = 30$ nm. The image is drawn to scale and the in-plane magnetic field direction, B_y is indicated.

We observe a switching current, I_s modulation in a JJ with $L = 1.1$ μm, with minima at 470 mT and 1250 mT, which are attributed to Zeeman induced $0-\pi$ transitions. One might be inclined to believe that this modulation is caused by an in-plane Fraunhofer interference effect, due to the finite thickness ($d = 30$ nm) of the InSb quantum well. The I_s minima of such a Fraunhofer pattern are expected to occur at $B_{node} = N\Phi_0/A$, where Φ_0 is the magnetic flux quantum, $A = d \cdot L$ is the cross-sectional 2DEG area and $N = 1, 2, 3, ...$ The second minimum should thus occur at twice the value of the first, which is not the case here. Moreover, based on the estimated cross-sectional area of the JJ (see Supplementary Fig. 4.9), one would expect the first node to be at 60 mT, inconsistent with the observation. In fact, it has been shown [54, 55] that a oscillatory interference pattern is not expected at all in such an SNS junction with $L \gg d$. Finally, for an in-plane interference effect one expects the B value at which the I_s minima occur to increase for more negative gate voltages, since the wavefunction is then squeezed and d effectively reduced. However, we observe the opposite behavior (i.e., the minima move to lower B), as expected for Zeeman-induced $0-\pi$ transitions. To conclude, we rule out an in-plane interference effect as a possible explanation for the supercurrent modulation.

We also performed measurements of the normal state resistance (R_n) as a function of in-plane magnetic field B_y to rule out possible magnetoresistance (MR) effects as a cause

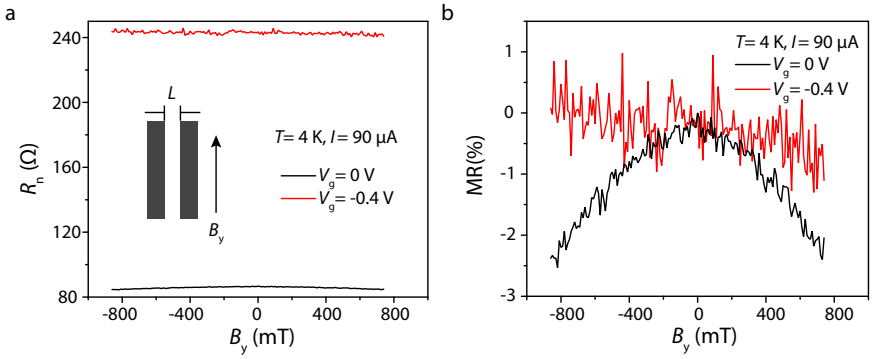

Figure 4.10: In-plane magnetoresistance. **a,** Normal state resistance (R_n) of JJ (L = 1.1 μm) as a function of B_y at two different gate voltages. **b,** Calculated MR (in %).

for the observed modulation in supercurrent (see Supplementary Fig. 4.10). To eliminate any remnant effects of superconductivity, the measurements are performed at high temperature (4 K) and high DC current bias (90 μA). We see a small MR (a few %) only at the highest density (V_g = 0 V), however there is no correlation with the supercurrent modulation (see Fig. 2 in main text), which changes by almost two orders of magnitude in the same magnetic field range.

4.10.6. ADDITIONAL GATE-DRIVEN $0-\pi$ TRANSITIONS AND ERROR ANALYSIS

Here, we present additional data of the gate-driven $0-\pi$ transitions in the JJ with L = 1.1 μm. The gate voltages of the $0-\pi$ transitions presented in the phase diagram are extracted from the plots in Supplementary Fig. 4.11. To systematically extract the value where gate-driven $0-\pi$ transition occurs and its error, we use a fit of the linetraces from Supplementary Fig. 4.11, at zero I. At the transition point, a peak in dV/dI indicates the $0-\pi$ transition. As an example, we show a single linetrace at 310 mT in Supplementary Fig. 4.12a, and extract the standard deviation, σ, based on a Gaussian fit of the peak. Subsequently, we used the gate to density mapping to convert σ to the error bar shown in the phase diagram. This fitting procedure is used for all magnetic fields (Supplementary Fig. 4.12b).

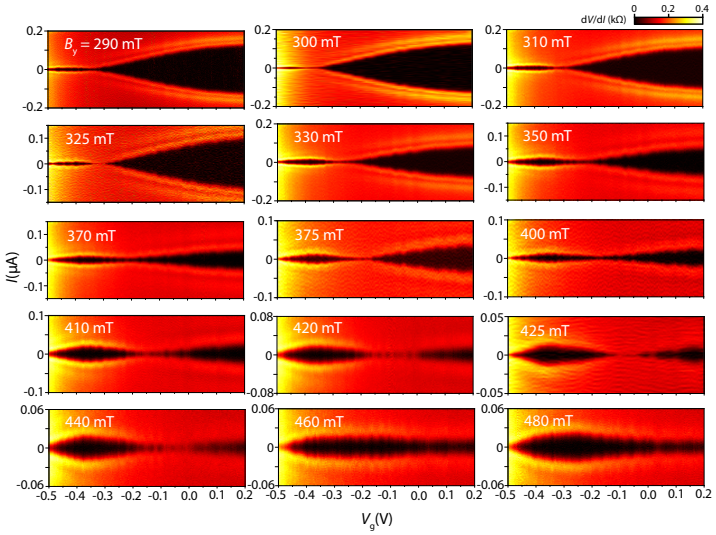

Figure 4.11: Additional gate-driven $0-\pi$ transitions. Differential resistance, $\mathrm{d}V/\mathrm{d}I$, as a function of current bias, I, and gate voltage, V_g, for the in-plane magnetic field values, B_y, indicated.

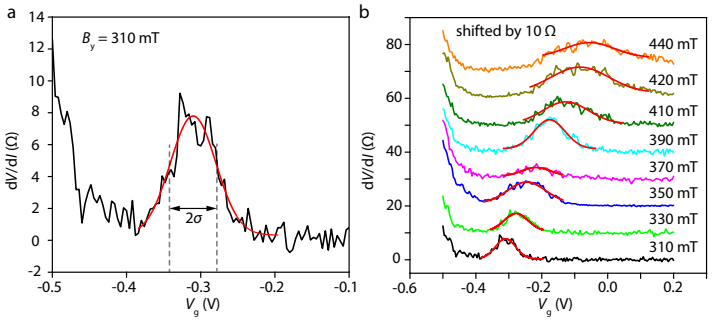

Figure 4.12: Transition point extraction and error analysis. **a-b,** Linetraces of the differential resistance, $\mathrm{d}V/\mathrm{d}I$, in the JJ with $L = 1.1$ μm as a function of gate voltage, V_g, for magnetic fields, B_y of 310 mT for **a**, and as indicated for **b**, respectively. The peaks observed are fitted with a Gaussian curve, to obtain the standard deviation, σ. In **b** the traces are shifted for clarity.

4.10.7. EFFECTIVE MASS MEASUREMENT

To extract the effective mass of the electrons in the InSb 2DEG, the temperature dependence of the Shubnikov-de Haas (SdH) oscillation amplitude is measured in a Hall bar geometry. Supplementary Figure 4.13a shows the magnetoresistance oscillations after the subtraction of a polynomial background, $\Delta\rho_{xx}$, as a function of filling factor, ν, for temperatures ranging from $T = 1.73$ K to $T = 10$ K. At a fixed filling factor, the effective

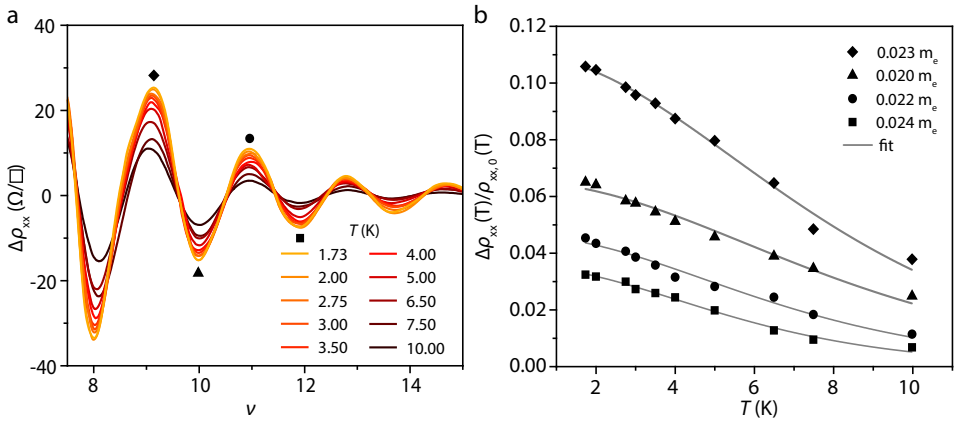

Figure 4.13: Temperature dependence of Shubnikov-de Haas oscillations and fitting for effective mass. **a,** Shubnikov-de Haas oscillation amplitude after polynomial background subtraction as a function of filling factor for temperatures $T = 1.73 - 10$ K. The symbols denote points that are used to extract the effective mass. **b,** Temperature dependence of the oscillation amplitude (symbols). The solid lines are fits to the data (using Eq. 4.2) in order to obtain the effective mass.

mass, m^*, can be obtained from a fit to the damping of the SdH oscillation amplitude with increasing temperature, using the expression

$$\frac{\Delta\rho_{xx}(T)}{\rho_{xx,0}(T)} \propto \frac{\alpha T}{\sinh(\alpha T)}, \tag{4.2}$$

where $\rho_{xx,0}(T)$ is the temperature-dependent low-field resistivity and $\alpha = \pi k_B m^* \nu/(\hbar^2 n)$. Supplementary Figure 4.13b shows such fits to the oscillation minima and maxima of $\nu = 10$ and $\nu = 12$, resulting in a mean effective mass of $m^* = (0.022 \pm 0.002) \cdot m_e$, with m_e being the free electron mass.

REFERENCES

1. Riwar, R. P., Houzet, M., Meyer, J. S. & Nazarov, Y. V. Multi-terminal Josephson junctions as topological matter. *Nat. Commun.* **7,** 11167 (2016).
2. Hart, S., Ren, H., Wagner, T., Leubner, P., Mühlbauer, M., Brüne, C., Buhmann, H., Molenkamp, L. W. & Yacoby, A. Induced superconductivity in the quantum spin Hall edge. *Nat. Phys.* **10,** 638–643 (2014).
3. Pribiag, V. S., Beukman, A. J. A., Qu, F., Cassidy, M. C., Charpentier, C., Wegscheider, W. & Kouwenhoven, L. P. Edge-mode Superconductivity in a Two-Dimensional Topological Insulator. *Nat. Nanotech.* **10,** 593–597 (2015).
4. Wan, Z., Kazakov, A., Manfra, M. J., Pfeiffer, L. N., West, K. W. & Rokhinson, L. P. Induced superconductivity in high-mobility two-dimensional electron gas in gallium arsenide heterostructures. *Nat. Commun.* **6,** 7426 (2015).
5. Amet, F., Ke, C. T., Borzenets, I. V., Wang, J., Watanabe, K., Taniguchi, T., Deacon, R. S., Yamamoto, M., Bomze, Y. V., Tarucha, S. & Finkelstein, G. Supercurrent in the quantum Hall regime. *Science* **352,** 966–969 (2016).
6. Lee, G.-H., Huang, K.-F., Efetov, D. K., Wei, D. S., Hart, S., Taniguchi, T., Watanabe, K., Yacoby, A. & Kim, P. Inducing superconducting correlation in quantum Hall edge states. *Nat. Phys.* **13,** 693–698 (2017).
7. Finocchiaro, F., Guinea, F. & San-Jose, P. Topological π Junctions from Crossed Andreev Reflection in the Quantum Hall Regime. *Phys. Rev. Lett.* **120,** 116801 (2018).
8. Casparis, L., Connolly, M. R., Kjaergaard, M., Pearson, N. J., Kringhøj, A., Larsen, T. W., Kuemmeth, F., Wang, T., Thomas, C., Gronin, S., Gardner, G. C., Manfra, M. J., Marcus, C. M. & Petersson, K. D. Superconducting gatemon qubit based on a proximitized two-dimensional electron gas. *Nat. Nanotech.* **13,** 915–919 (2018).
9. Wang, J. I.-J., Rodan-Legrain, D., Bretheau, L., Campbell, D. L., Kannan, B., Kim, D., Kjaergaard, M., Krantz, P., Samach, G. O., Yan, F., Yoder, J. L., Watanabe, K., Taniguchi, T., Orlando, T. P., Gustavsson, S., Jarillo-Herrero, P. & Oliver, W. D. Quantum coherent control of a hybrid superconducting circuit made with graphene-based van der Waals heterostructures. *Nat. Nanotech.* **14,** 120–125 (2019).
10. Rokhinson, L. P., Liu, X. & Furdyna, J. K. The fractional a.c. Josephson effect in a semiconductor–superconductor nanowire as a signature of Majorana particles. *Nat. Phys.* **8,** 795–799 (2012).
11. Nichele, F., Drachmann, A. C. C., Whiticar, A. M., O'Farrell, E. C. T., Suominen, H. J., Fornieri, A., Wang, T., Gardner, G. C., Thomas, C., Hatke, A. T., Krogstrup, P., Manfra, M. J., Flensberg, K. & Marcus, C. M. Scaling of Majorana Zero-Bias Conductance Peaks. *Phys. Rev. Lett.* **119,** 136803 (2017).

12. Ren, H., Pientka, F., Hart, S., Pierce, A. T., Kosowsky, M., Lunczer, L., Schlereth, R., Scharf, B., Hankiewicz, E. M., Molenkamp, L. W., Halperin, B. I. & Yacoby, A. Topological superconductivity in a phase-controlled Josephson junction. *Nature* **569,** 93–98 (2019).

13. Fornieri, A., Whiticar, A. M., Setiawan, F., Portolés, E., Drachmann, A. C. C., Keselman, A., Gronin, S., Thomas, C., Wang, T., Kallaher, R., Gardner, G. C., Berg, E., Manfra, M. J., Stern, A., Marcus, C. M. & Nichele, F. Evidence of topological superconductivity in planar Josephson junctions. *Nature* **569,** 89–92 (2019).

14. Bezuglyi, E. V., Rozhavsky, A. S., Vagner, I. D. & Wyder, P. Combined effect of Zeeman splitting and spin-orbit interaction on the Josephson current in a superconductor-two-dimensional electron gas-superconductor structure. *Phys. Rev. B* **66,** 052508 (2002).

15. Yokoyama, T., Eto, M. & Nazarov, Y. V. Anomalous Josephson effect induced by spin-orbit interaction and Zeeman effect in semiconductor nanowires. *Phys. Rev. B* **89,** 195407 (2014).

16. Szombati, D. B., Nadj-Perge, S., Car, D., Plissard, S. R., Bakkers, E. P. A. M. & Kouwenhoven, L. P. Josephson ϕ_0-junction in nanowire quantum dots. *Nature Physics* **12,** 568–572 (2016).

17. Hart, S., Ren, H., Kosowsky, M., Ben-Shach, G., Leubner, P., Brüne, C., Buhmann, H., Molenkamp, L. W., Halperin, B. I. & Yacoby, A. Controlled finite momentum pairing and spatially varying order parameter in proximitized HgTe quantum wells. *Nat. Phys.* **13,** 87 (2017).

18. Chen, A. Q., Park, M. J., Gill, S. T., Xiao, Y., Reig-i-Plessis, D., MacDougall, G. J., Gilbert, M. J. & Mason, N. Finite momentum Cooper pairing in three-dimensional topological insulator Josephson junctions. *Nat. Commun.* **9,** 3478 (2018).

19. Li, C., de Ronde, B., de Boer, J., Ridderbos, J., Zwanenburg, F., Huang, Y., Golubov, A. & Brinkman, A. Zeeman-Effect-Induced $0-\pi$ Transitions in Ballistic Dirac Semimetal Josephson Junctions. *Phys. Rev. Lett.* **123,** 026802 (2019).

20. Pientka, F., Keselman, A., Berg, E., Yacoby, A., Stern, A. & Halperin, B. I. Topological Superconductivity in a Planar Josephson Junction. *Phys. Rev. X* **7,** 021032 (2017).

21. Hell, M., Leijnse, M. & Flensberg, K. Two-Dimensional Platform for Networks of Majorana Bound States. *Phys. Rev. Lett.* **118,** 107701 (2017).

22. Nayak, C., Simon, S. H., Stern, A., Freedman, M. & Das Sarma, S. Non-Abelian anyons and topological quantum computation. *Rev. Mod. Phys.* **80,** 1083–1159 (2008).

23. Karzig, T., Knapp, C., Lutchyn, R. M., Bonderson, P., Hastings, M. B., Nayak, C., Alicea, J., Flensberg, K., Plugge, S., Oreg, Y., Marcus, C. M. & Freedman, M. H. Scalable designs for quasiparticle-poisoning-protected topological quantum computation with Majorana zero modes. *Phys. Rev. B* **95,** 235305 (2017).

24. Plugge, S., Rasmussen, A., Egger, R. & Flensberg, K. Majorana box qubits. *New J. Phys.* **19,** 012001 (2017).

25. Gilbertson, A. M., Branford, W. R., Fearn, M., Buckle, L., Buckle, P. D., Ashley, T. & Cohen, L. F. Zero-field spin splitting and spin-dependent broadening in high-mobility InSb/$In_{1-x}Al_xSb$ asymmetric quantum well heterostructures. *Phys. Rev. B* **79,** 235333 (2009).

26. Kallaher, R. L., Heremans, J. J., Goel, N., Chung, S. J. & Santos, M. B. Spin-orbit interaction determined by antilocalization in an InSb quantum well. *Phys. Rev. B* **81,** 075303 (2010).

27. Nedniyom, B., Nicholas, R. J., Emeny, M. T., Buckle, L., Gilbertson, A. M., Buckle, P. D. & Ashley, T. Giant enhanced g-factors in an InSb two-dimensional gas. *Phys. Rev. B* **80,** 125328 (2009).

28. Qu, F., van Veen, J., de Vries, F. K., Beukman, A. J. A., Wimmer, M., Yi, W., Kiselev, A. A., Nguyen, B.-M., Sokolich, M., Manfra, M. J., Nichele, F., Marcus, C. M. & Kouwenhoven, L. P. Quantized Conductance and Large g-Factor Anisotropy in InSb Quantum Point Contacts. *Nano Lett.* **16,** 7509–7513 (2016).

29. Mourik, V., Zuo, K., Frolov, S. M., Plissard, S. R., Bakkers, E. P. A. M. & Kouwenhoven, L. P. Signatures of Majorana fermions in hybrid superconductor-semiconductor nanowire devices. *Science* **336,** 1003–1007 (2012).

30. Zhang, H., Liu, C.-X., Gazibegovic, S., Xu, D., Logan, J. A., Wang, G., van Loo, N., Bommer, J. D. S., de Moor, M. W. A., Car, D., Op het Veld, R. L. M., van Veldhoven, P. J., Koelling, S., Verheijen, M. A., Pendharkar, M., Pennachio, D. J., Shojaei, B., Lee, J. S., Palmstrøm, C. J., Bakkers, E. P. A. M., Sarma, S. D. & Kouwenhoven, L. P. Quantized Majorana conductance. *Nature* **556,** 74–79 (2018).

31. Yi, W., A. Kiselev, A., Thorp, J., Noah, R., Nguyen, B.-M., Bui, S., D. Rajavel, R., Hussain, T., F. Gyure, M., Kratz, P., Qian, Q., Manfra, M., S. Pribiag, V., P. Kouwenhoven, L., Marcus, C. M. & Sokolich, M. Gate-tunable high mobility remote-doped InSb/$In_{1-x}Al_xSb$ quantum well heterostructures. *Appl. Phys. Lett.* **106,** 142103 (2015).

32. Masuda, T., Sekine, K., Nagase, K., Wickramasinghe, K. S., Mishima, T. D., Santos, M. B. & Hirayama, Y. Transport characteristics of InSb trench-type in-plane gate quantum point contact. *Appl. Phys. Lett.* **112,** 192103 (2018).

33. Altshuler, B. L. & Spivak, B. Z. Mesoscopic Fluctations in a Superconductor–Normal Metal–Superconductor Junction. *Sov. Phys. JETP* **65,** 343 (1987).

34. Strictly speaking we experimentally measure the switching current I_s, but expect it to be close to I_c, since the Josephson energy ($\approx 20\,K$) is significantly larger than the fridge temperature ($\approx 50\,mK$).

35. Ishii, C. Josephson Currents through Junctions with Normal Metal Barriers. *Prog. Theor. Phys.* **44,** 1525 (1970).

36. Ben Shalom, M., Zhu, M. J., Fal'ko, V. I., Mishchenko, A., Kretinin, A. V., Novoselov, K. S., Woods, C. R., Watanabe, K., Taniguchi, T., Geim, A. K. & Prance, J. R. Quantum oscillations of the critical current and high-field superconducting proximity in ballistic graphene. *Nat. Phys.* **12,** 318–322 (2016).

37. Borzenets, I. V., Amet, F., Ke, C. T., Draelos, A. W., Wei, M. T., Seredinski, A., Watanabe, K., Taniguchi, T., Bomze, Y. V., Yamamoto, M., Tarucha, S. & Finkelstein, G. Ballistic Graphene Josephson Junctions from the Short to the Long Junction Regimes. *Phys. Rev. Lett.* **117,** 237002 (2016).

38. Bulaevskii, L. N., Kuzii, V. V. & Sobyanin, A. A. Superconducting system with weak coupling to the current in the ground state. *JETP Lett.* **25,** 290 (1977).

39. Demler, E. A., Arnold, G. B. & Beasley, M. R. Superconducting proximity effects in magnetic metals. *Phys. Rev. B* **55,** 15174–15182 (1997).

40. Buzdin, A. I. Proximity effects in superconductor-ferromagnet heterostructures. *Rev. Mod. Phys.* **77,** 935–976 (2005).

41. Suominen, H. J., Danon, J., Kjaergaard, M., Flensberg, K., Shabani, J., Palmstrøm, C. J., Nichele, F. & Marcus, C. M. Anomalous Fraunhofer interference in epitaxial superconductor-semiconductor Josephson junctions. *Phys. Rev. B* **95,** 035307 (2017).

42. Calado, V. E., Goswami, S., Nanda, G., Diez, M., Akhmerov, A. R., Watanabe, K., Taniguchi, T., Klapwijk, T. M. & Vandersypen, L. M. K. Ballistic Josephson junctions in edge-contacted graphene. *Nat. Nanotech.* **10,** 761–764 (2015).

43. Allen, M. T., Shtanko, O., Fulga, I. C., Wang, J. I.-J., Nurgaliev, D., Watanabe, K., Taniguchi, T., Akhmerov, A. R., Jarillo-Herrero, P., Levitov, L. S. & Yacoby, A. Observation of Electron Coherence and Fabry–Perot Standing Waves at a Graphene Edge. *Nano Lett.* **17,** 7380–7386 (2017).

44. Gingrich, E. C., Niedzielski, B. M., Glick, J. A., Wang, Y., Miller, D. L., Loloee, R., Pratt Jr, W. P. & Birge, N. O. Controllable 0–π Josephson junctions containing a ferromagnetic spin valve. *Nat. Phys.* **12,** 564–567 (2016).

45. Terzioglu, E. & Beasley, M. R. Complementary Josephson junction devices and circuits: a possible new approach to superconducting electronics. *IEEE Trans. Appl. Supercond.* **8,** 48–53 (1998).

46. Gardner, G. C., Fallahi, S., Watson, J. D. & Manfra, M. J. Modified MBE hardware and techniques and role of gallium purity for attainment of two dimensional electron gas mobility >35×106cm2/Vs in AlGaAs/GaAs quantum wells grown by MBE. *J. Crys. Growth* **441,** 71–77 (2016).

47. Liu, W. K., Goldammer, K. J. & Santos, M. B. Effect of substrate temperature on Si compensation in δ-doped InSb and AlxIn1-xSb grown by molecular beam epitaxy. *J. Appl. Phys.* **84,** 205–208 (1998).

48. Flensberg, K., Hansen, J. B. & Octavio, M. Subharmonic energy-gap structure in superconducting weak links. *Phys. Rev. B* **38,** 8707–8711 (1988).

49. Kjaergaard, M., Suominen, H. J., Nowak, M. P., Akhmerov, A. R., Shabani, J., Palmstrøm, C. J., Nichele, F. & Marcus, C. M. Transparent Semiconductor-Superconductor Interface and Induced Gap in an Epitaxial Heterostructure Josephson Junction. *Phys. Rev. Applied* **7,** 034029 (2017).

50. Zhang, H., Gül, Ö., Conesa-Boj, S., Nowak, M. P., Wimmer, M., Zuo, K., Mourik, V., de Vries, F. K., van Veen, J., de Moor, M. W. A., Bommer, J. D. S., van Woerkom, D. J., Car, D., Plissard, S. R., Bakkers, E. P. A. M., Quintero-Pérez, M., Cassidy, M. C., Koelling, S., Goswami, S., Watanabe, K., Taniguchi, T. & Kouwenhoven, L. P. Ballistic superconductivity in semiconductor nanowires. *Nat. Commun.* **8,** 16025 (2017).

51. Gill, S. T., Damasco, J., Janicek, B. E., Durkin, M. S., Humbert, V., Gazibegovic, S., Car, D., Bakkers, E. P. A. M., Huang, P. Y. & Mason, N. Selective-Area Superconductor Epitaxy to Ballistic Semiconductor Nanowires. *Nano Lett.* **18,** 6121–6128 (2018).

52. Iordanskii, S. V., Lyanda-Geller, Y. B. & Pikus, G. E. Weak-Localization in Quantum-Wells With Spin-Orbit Interaction. *Zh. Eksp. Teor. Fiz.* **60,** 199–203 (1994).

53. Rasmussen, A., Danon, J., Suominen, H., Nichele, F., Kjaergaard, M. & Flensberg, K. Effects of spin-orbit coupling and spatial symmetries on the Josephson current in SNS junctions. *Phys. Rev. B* **93,** 155406 (2016).

54. Monaco, R., Aaroe, M., Mygind, J. & Koshelets, V. P. Static properties of small Josephson tunnel junctions in an oblique magnetic field. *Phys. Rev. B* **79,** 144521 (2009).

55. Chiodi, F., Ferrier, M., Guéron, S., Cuevas, J. C., Montambaux, G., Fortuna, F., Kasumov, A. & Bouchiat, H. Geometry-related magnetic interference patterns in long SNS Josephson junctions. *Phys. Rev. B* **86,** 064510 (2012).

5

InSbAs two-dimensional electron gases as a platform for topological superconductivity

Christian M. Moehle*, Chung Ting Ke*, Qingzhen Wang, Candice Thomas, Di Xiao, Saurabh Karwal, Mario Lodari, Vincent van de Kerkhof, Ruben Termaat, Geoffrey C. Gardner, Giordano Scappucci, Michael J. Manfra, Srijit Goswami

Topological superconductivity can be engineered in semiconductors with strong spin-orbit interaction coupled to a superconductor. Experimental advances in this field have often been triggered by the development of new hybrid material systems. Among these, two-dimensional electron gases (2DEGs) are of particular interest due to their inherent design flexibility and scalability. Here we discuss results on a 2D platform based on a ternary 2DEG (InSbAs) coupled to in-situ grown Aluminum. The spin-orbit coupling in these 2DEGs can be tuned with the As concentration, reaching values up to 400 meVÅ*, thus exceeding typical values measured in its binary constituents. In addition to a large Landé g-factor ~ 55 (comparable to InSb), we show that the clean superconductor-semiconductor interface leads to a hard induced superconducting gap. Using this new platform we demonstrate the basic operation of phase-controllable Josephson junctions, superconducting islands and quasi-1D systems, prototypical device geometries used to study Majorana zero modes.*

This chapter has been published in Nano Letters 21, 9990-9996 (2021).

*These authors contributed equally to this work.

5.1. Introduction

Topological phases of matter are currently a subject of intense research. Following early theoretical proposals [1, 2], materials with large spin-orbit interaction (such as InAs and InSb) coupled to superconductors have emerged as a promising platform to engineer topological superconductivity in the form of Majorana zero modes (MZMs). In this context, one-dimensional nanowires have been studied extensively over the years [3–5]. More recently, several efforts have been focused on engineering MZMs in two-dimensional electron gases (2DEGs). Not only do 2DEGs provide a scalable platform for future development of topological qubits, but their inherent flexibility allows for the realization of more complex devices. The versatility of the 2DEG platform can be seen in the variety of experiments performed on quasi-1D structures [6], superconducting islands [7], multi-terminal Josephson junctions (JJs) [8], and phase-biased JJs [9, 10], all of which are promising architectures to create topological systems. Many of these studies have been performed on InAs 2DEGs where it is possible to create a pristine interface between the superconductor Aluminum (Al) and the 2DEG allowing for a strong superconducting proximity effect [11, 12].

The InSb 2DEG is another appealing platform, primarily due to its significantly larger g-factor and spin-orbit coupling. Whereas the former allows the hybrid system to enter the topological regime at a lower magnetic field, the latter is crucial in determining the topological gap that protects the MZMs. These 2DEGs have recently been proximitized by ex-situ superconductors [13], however there exist no reports of InSb-based hybrid systems with in-situ grown superconductors. This could be related to the band offset at the InSb-Al interface, which (unlike InAs) prevents an efficient accumulation of charge carriers and hence induced superconductivity [14]. It would thus be ideal to have a material system with the desirable properties of both InAs and InSb.

In this work we explore such a new hybrid material: ternary (InSbAs) 2DEGs coupled to in-situ grown Al. Using magneto-transport experiments we demonstrate a large g-factor (~ 55) and exceptionally strong spin-orbit coupling exceeding the values of either InAs or InSb. In addition, the pristine semiconductor-superconductor interface leads to a hard induced superconducting gap that is revealed by spectroscopy measurements. Furthermore, using these ternary 2DEGs we demonstrate the stable operation of prototypical devices studied in the context of MZMs: phase-controllable JJs, superconducting islands, and quasi-1D structures. Our results show that InSbAs/Al 2DEGs offer the combined advantages of their binary constituents and are therefore a promising platform to realize topological superconductivity.

5.2. Material growth

$InSb_{1-x}As_x$ 2DEGs with varying As concentration, x, are grown by molecular beam epitaxy (MBE) on undoped, semi-insulating GaAs (100) substrates (see Fig. 5.1a for a schematic of the layer stack). The growth starts with a 100 nm GaAs buffer layer, directly followed by a 1 μm thick AlSb nucleation layer [15] and a 4 μm thick $Al_{0.1}In_{0.9}Sb$ layer. The latter forms a closely matched pseudo-substrate for the $InSb_{1-x}As_x$ growth and the bottom

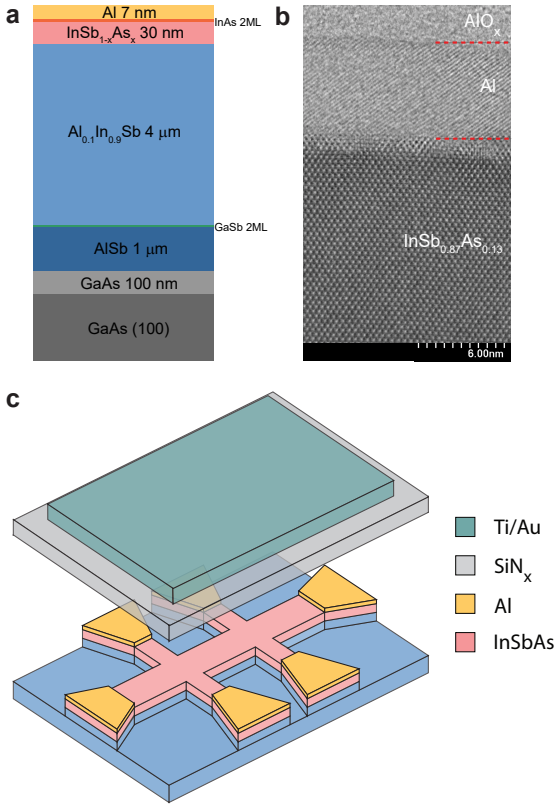

Figure 5.1: Hybrid Al/InSbAs heterostructures. **a,** Layer stack of the Al-$InSb_{1-x}As_x$ hybrid heterostructures. **b,** Bright-field scanning transmission electron micrograph of the Al-$InSb_{0.870}As_{0.130}$ interface along the [110] zone axis of the semiconductor. Red lines indicate the boundaries of the Aluminum. **c,** Schematic of a Hall bar that is used to extract the 2DEG properties.

barrier of the quantum well [16]. The As concentration in the $InSb_{1-x}As_x$ is controlled by the growth temperature and the As flux. In this study, heterostructures with $x = 0$, 0.053, 0.080, 0.130, 0.140 and 0.240 are grown. The semiconductor growth is terminated by the deposition of 2 monolayers (ML) InAs, serving as a screening layer to prevent intermixing between the semiconductor structure and the superconducting Al layer [17]. After the semiconductor growth, the heterostructures are transferred under ultra-high vacuum to a second MBE chamber to deposit 7 nm of Al, using methods described in [17]. Figure 5.1b displays a bright field scanning transmission electron micrograph focusing on the Al/$InSb_{1-x}As_x$ interface for $x = 0.130$. The interface appears sharp with a slight change of atomic contrast that is attributed to the relaxed InAs screening layer [17]. Further details about the growth process can be found in the Supplementary Information (SI).

5.3. Semiconducting properties

We characterize the semiconducting properties of the InSbAs 2DEGs by removing the Al in the active device area to fabricate Hall bars. After the Al removal, the 2DEG is etched in unwanted areas, followed by the deposition of a SiN_x dielectric layer. Lastly, a Ti/Au top-gate is evaporated and used to control the electron density in the 2DEG (see Fig. 5.1c for a schematic). We find peak mobilities of $20\,000-28\,000\,cm^2/Vs$ (see SI for mobility-density curves, and further details about the device fabrication).

To study the spin-orbit coupling in these 2DEGs, we measure the longitudinal conductivity, σ_{xx}, in perpendicular magnetic fields, $B_\perp$, at 300 mK using standard lock-in techniques. The simultaneously measured transversal Hall resistance allows us to deduce the density, n, in the 2DEG at every gate voltage, V_g. Figure 5.2a shows the magneto-conductivity correction, $\Delta\sigma_{xx}(B_\perp) = \sigma_{xx}(B_\perp) - \sigma_{xx}(0)$, at $V_g = 0$V for x = 0, 0.053, 0.130 and 0.240, where the individual curves are offsetted for clarity. We observe clear weak anti-localization (WAL) peaks that are caused by the suppression of coherent backscattering due to spin-orbit coupling. Since we expect the linear Rashba term to be the dominating spin-orbit contribution in these asymmetric quantum wells, we fit the WAL peaks with the Rashba-dominated Iordanskii, Lyanda-Geller, and Pikus (ILP) model [18, 19] (grey curves in Fig. 5.2a). This allows us to extract the spin-orbit length, $l_{so} = \sqrt{D\tau_{so}}$, where $D = v_F l_e/2$ is the diffusion constant. Here, τ_{so} is the spin-orbit scattering time, v_F the Fermi velocity and l_e the mean free path. The linear Rashba parameter is given by $\alpha = \Delta_{so}/2k_F$, where $\Delta_{so} = \sqrt{2\hbar^2/\tau_{so}\tau_e}$ is the spin-split energy, k_F the Fermi wave vector, and τ_e the elastic scattering time.

As shown in Fig. 5.2a, the ILP model fits the experimental data well. The resulting linear Rashba parameter for the four different As concentrations is plotted in the inset. It is striking that α increases monotonically with increasing As concentration. Compared to the value for pure InSb ($\alpha \approx 100$ meVÅ), it is noteworthy that for the higher As concentrations, the linear Rashba parameter is 3-4 times larger (300 − 400 meVÅ). We proceed by measuring WAL as a function of gate voltage (V_g) for the different As concentrations. In Fig. 5.2b and 5.2c we show l_{so} and α plotted against V_g (see SI for the same plots as a function of electron density). The trend of decreasing (increasing) l_{so} (α) with increasing As concentration persists also when comparing at other gate voltages. We note, however, that specifically for $x = 0.240$, the spin-orbit coupling becomes so large that l_{so} is smaller than l_e. This might lead to inaccuracies in the extracted fit parameters as the ILP model is valid when l_e is the smallest length scale.

The systematic increase in spin-orbit coupling with As concentration can arise from a combination of several effects. Firstly, bandstructure calculations of $InSb_{1-x}As_x$ show that the Rashba parameter is strongly influenced by the As concentration [20, 21], which has been observed in experiments on ternary nanowires [22]. Secondly, electric fields across the 2DEG can also influence the spin-orbit interaction. We note that even at $V_g = 0$V, α increases monotonically with x, suggesting that the external electric field from the applied gate voltage is not the primary source of the enhancement. However the internal field (generated at the 2DEG-gate dielectric interface) could be a strong

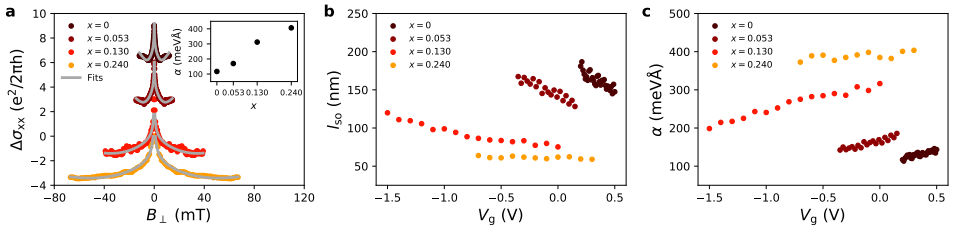

Figure 5.2: Large and tunable spin-orbit coupling. **a,** Magneto-conductivity correction at $V_g = 0$V for the different $InSb_{1-x}As_x$ 2DEGs. The $x = 0$ curve is measured at $V_g = 0.2$V due to a high resistance at $V_g = 0$V. The gray lines are ILP fits to the weak anti-localization data. In the inset the extracted linear Rashba coefficient is plotted for the four As concentrations, showing a monotonic increase with increasing As concentration. For the higher As concentrations, α is 3-4 times larger as compared to the value for pure InSb ($x = 0$). **b,** Spin-orbit length plotted against V_g. **c,** α as a function of V_g. l_{so} (α) decreases (increases) with increasing As concentration when comparing at a fixed gate voltage.

5

function of the As concentration. We indeed observe that the nominal density in the 2DEG (density at $V_g = 0$V) increases systematically with As concentration (see SI), indicating a stronger downward band bending at the dielectric-semiconductor interface resulting in an increased electric field. While from these studies it is difficult to disentangle the effects of the bulk semiconductor from the interfaces, similar experiments on deep InSbAs quantum wells would shed more light on the origins of the enhanced spin-orbit interaction.

Having established strong spin-orbit coupling in $InSb_{1-x}As_x$ 2DEGs, we proceed by measuring the perpendicular g-factor, g^*. By comparing the temperature dependence of Shubnikov-de Haas oscillations for an odd-even filling factor couple, an expression for g^* can be obtained [23]. For $x = 0$ we find $g^* = 47.8 \pm 2.8$. The same analysis is done for $x = 0.130$, where we obtain $g^* = 54.6 \pm 3.1$ (see SI for details about the data analysis, as well as effective mass measurements for the two As concentrations). This shows that besides strong spin-orbit coupling, InSbAs 2DEGs also possess a large g-factor that is comparable to the one of pure InSb.

5.4. INDUCED SUPERCONDUCTIVITY

Given that the semiconducting properties of InSbAs 2DEGs are favorable to realize topological phases, we now demonstrate that these 2DEGs also have excellent coupling to Al. To do so, we use devices as shown in the false-colored scanning electron micrograph (SEM) in Fig. 5.3a. This device can either be operated as a gate-tunable JJ (gray circuit) or a spectroscopy device (black circuit) to measure the local density of states. All devices are measured at a temperature of 30 mK.

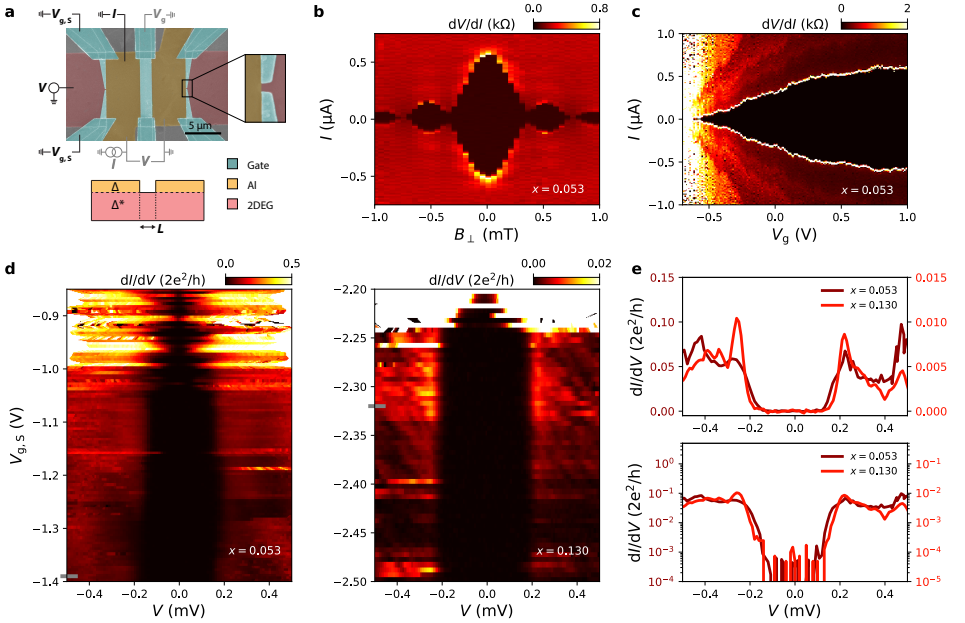

Figure 5.3: Hard induced superconducting gap. **a,** False-colored SEM of a combined JJ and tunneling spectroscopy device. A cross-sectional schematic the JJ part is shown in the bottom. All devices have a fixed JJ length of $L \approx 150\,\mathrm{nm}$. **b,** Differential resistance as a function of applied current bias and perpendicular magnetic field for the $x = 0.053$ JJ. The Fraunhofer interference pattern signifies a uniform current distribution in the JJ. **c,** Differential resistance as a function of applied current bias and gate voltage for the same JJ, showing that the switching current, I_S, can be fully suppressed. **d,** Differential conductance as a function of splitgate voltage and applied voltage bias for $x = 0.053$ and $x = 0.130$. The color scale has been saturated to increase the visibility of the tunneling regime. For both As concentrations, the induced superconducting gap is visible (region of suppressed conductance), stable over a large range in $V_{g,S}$. **e,** Linecuts at the indicated positions (gray markers) on linear and logarithmic scale. The size of the induced gap is similar for both As concentrations. The in-gap conductance is suppressed by 2-3 orders of magnitude as compared to the out-of gap conductance, indicating a hard induced gap.

It is important to note that we do not see any induced superconductivity for pure InSb, presumably due to an unfavorable band alignment at the Al-InSb interface. In stark contrast, all the InSbAs 2DEGs (irrespective of As concentration) have excellent coupling to the superconductor, where all JJs display supercurrents and pronounced multiple Andreev reflections (see SI). In Fig. 5.3b we show a representative Fraunhofer interference pattern for the JJ with $x = 0.053$, where the black regions correspond to zero resistance. The size of the switching current, I_S, can be controlled by the gate voltage, as demon-

strated in Fig. 5.3c for the same As concentration. Upon lowering V_g, I_s shrinks and correspondingly, the normal-state resistance of the JJ, R_n, increases.

Clean and transparent interfaces are crucial for the realization of MZMs as they allow the proximitized semiconductor to obtain a hard induced superconducting gap with a vanishing in-gap density of states. It is therefore important to measure the density of states in the proximitized 2DEG directly. To this end, we operate the devices shown in Fig. 5.3a as spectroscopy devices. We apply a voltage bias to the left normal contact, and measure the current flowing through the Al lead, while energizing the splitgates with a negative voltage, $V_{g,S}$, to create a barrier. In the tunneling regime the measured conductance is proportional to the density of states in the proximitized 2DEG. In Fig. 5.3d we present tunneling spectroscopy maps for $x = 0.053$ and $x = 0.130$. In both measurements we note the emergence of a region with suppressed conductance, reflecting the induced superconducting gap. The gaps persist over an extended range in $V_{g,S}$ with a slight dependence of the gap size on the out-of-gap conductance. In Fig. 5.3e we show two representative linecuts in the tunneling regime. We find that the size of the induced gap is similar for both As concentrations ($\Delta^* \approx 220\,\mu$eV). Turning to the linecuts on the logarithmic scale and comparing the out-of-gap conductance with the in-gap conductance, we see that the in-gap conductance is suppressed by 2-3 orders of magnitude for both As concentrations. This confirms the excellent Al-2DEG interface.

5.5. PROTOTYPICAL MAJORANA DEVICES

Using the InSbAs/Al hybrid platform we realize three prototypical device architectures used to study MZMs: phase-controllable JJs, superconducting islands and quasi-1D superconducting strips. Figure 5.4a shows false-colored SEMs of a JJ embedded in a superconducting loop. A perpendicular magnetic field, $B_\perp$, penetrating through the loop can be used to tune the phase difference across the JJ. Split gates are positioned at the top and bottom edge of the JJ to perform tunneling spectroscopy at both ends of the phase-controllable JJ. In Fig. 5.4b we show spectroscopy maps at the top (top panel) and bottom (bottom panel) of the JJ, with representative linecuts shown in Fig. 5.4c. In both cases we observe a clear flux-dependent modulation of the gap, consistent with the phase modulation expected for Andreev bound states. Such three-terminal devices are important to check for correlations between the two ends of the JJ, when tuned into the topological regime.

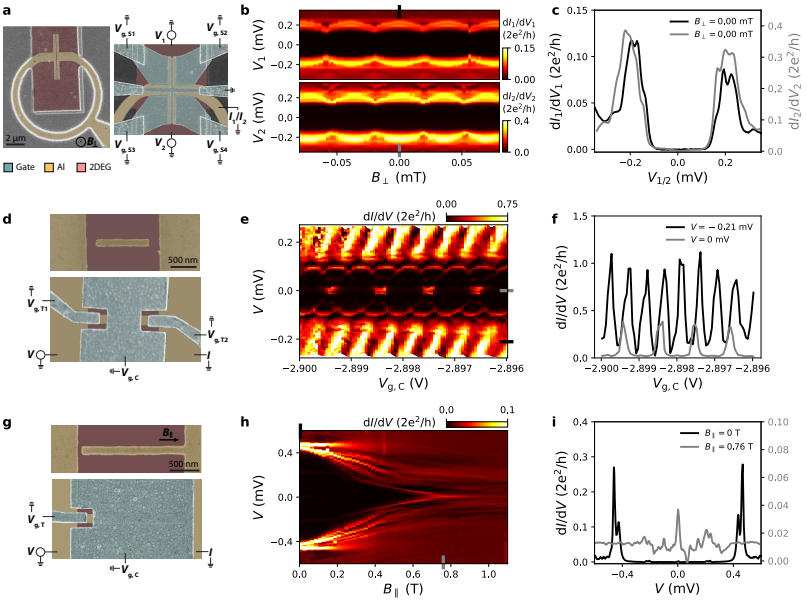

Figure 5.4: Prototypical Majorana devices. **a,** False-colored SEMs of a phase-biased JJ before (left) and after (right) gate deposition. The split gates at the top and bottom edge of the JJ are used to perform tunneling spectroscopy at both ends of the JJ. This device is fabricated on a 2DEG with $x = 0.080$. **b,** Differential conductance as a function of voltage bias applied to the top contact and perpendicular magnetic field while the bottom tunneling contact is floating (top panel). The bottom panel shows the tunneling spectroscopy map as a function of bottom voltage bias and perpendicular magnetic field (top tunneling contact floating). For both measurements the splitgates are fixed at $V_{g,S1} = -2.36\,\mathrm{V}$, $V_{g,S2} = -1.36\,\mathrm{V}$ and $V_{g,S3} = V_{g,S4} = -1.48\,\mathrm{V}$. **c,** Linecuts from **b** at the indicated positions. **d,** SEMs of a superconducting island before (top) and after (bottom) gate deposition, fabricated on a 2DEG with $x = 0.140$. The two tunnel gates are used to tune the transmission between the leads and the island. The central gate depletes the surrounding 2DEG and changes the charge occupancy of the island. **e,** Differential conductance at fixed tunnel gate voltages ($V_{g,T1} = -2.157\,\mathrm{V}$, $V_{g,T2} = -2.052\,\mathrm{V}$) as a function of applied voltage bias and central gate voltage. 2e-periodic Coulomb oscillations are visible at $V = 0\,\mathrm{mV}$ and 1e-periodic Coulomb oscillations at high biases. **f,** Linecuts from **e** at the indicated positions. **g,** SEMs of a quasi-1D grounded superconducting strip before (top) and after (bottom) gate deposition. The left gate is used to create a tunnel barrier between the bulk Al contact and the superconducting strip, and the central gate depletes the surrounding 2DEG. This device is fabricated on a 2DEG with $x = 0.140$. **h,** Differential conductance at fixed gate voltages ($V_{g,T} = -3.96\,\mathrm{V}$, $V_{g,C} = -4.40\,\mathrm{V}$) as a function of applied voltage bias and parallel magnetic field. **i,** Linecuts from **h** at the indicated positions.

A second approach to create MZMs is based on a floating narrow strip of superconductor, a superconducting island (see Fig. 5.4d). Here two tunnel gates are used to tune the transmission between the bulk Al contacts and the island. The central gate depletes the 2DEG in areas that are not covered with Al, and changes the charge occupancy on the island. In Fig. 5.4e we show a differential conductance map at fixed tunnel gate voltages, $V_{g,T}$, varying the applied voltage bias, V, and the central gate voltage, $V_{g,C}$. At $V = 0\,\mathrm{mV}$ (see also gray linecut in Fig. 5.4f) we observe Coulomb peaks that have twice the spacing as compared to the Coulomb peaks at high biases (black linecut in Fig. 5.4f). The Coulomb peaks at $V = 0\,\mathrm{mV}$ reflect 2e-periodic Cooper pair transport through the superconducting island, while at high biases, quasiparticles with 1e charge are allowed to tunnel through the island.

Another strategy to study MZMs employs a grounded narrow strip of superconductor (see Fig. 5.4g). The narrow gate is used to define a tunnel barrier between the bulk Al contact and the quasi-1D strip, and the central gate depletes the remaining exposed 2DEG. In Fig. 5.4h we present a tunneling spectroscopy map at fixed gate voltages as a function of applied voltage bias, V, and magnetic field, $B_\parallel$. $B_\parallel$ is oriented along the superconducting finger. Two representative linecuts are shown in Fig. 5.4i. Whereas at $B_\parallel = 0\,\mathrm{T}$ we observe a hard induced superconducting gap (note that the gap size is doubled due to the superconducting contact), a zero energy state emerges around $B_\parallel = 0.7\,\mathrm{T}$. While these results are promising, further experiments are required to comment on the origin of these states.

5.6. CONCLUSION

In conclusion, we have shown that InSbAs 2DEGs offer the combined advantages of the more commonly studied binary materials. In addition to a large g-factor, they have excellent coupling to in-situ grown Aluminum. Furthermore, the spin-orbit coupling in these ternary 2DEGs is significantly stronger than in either InAs or InSb. Using this hybrid system, we realize distinct device architectures that can be used to study topological superconductivity.

AUTHOR CONTRIBUTIONS

C. M. M. and C. T. K contributed equally, fabricated and measured the devices together with Q. W., S. K., V. vd K. and R. T. The MBE growth of the semiconductor heterostructures and the characterization of the materials was performed by C. T., D. X. and G. C. G. under the supervision of M. J. M. The effective mass and g-factor measurements were provided by M. L. and G. S. The manuscript was written by **C. M. M.**, C. T. K and S. G., with inputs from all co-authors. S. G. supervised the experimental work in Delft.

DATA AVAILABILITY

Raw data and analysis scripts for all presented figures are available at the 4TU.ResearchData repository, DOI: https://doi.org/10.4121/14565228

Acknowledgments
We thank Michael Wimmer and Michal P. Nowak for useful discussions. Moreover we would like to thank J.H. Dycus, M.E. Salmon and R.E. Daniel from Eurofins EAG Materials Science for the TEM studies. The research at Delft was supported by the Dutch National Science Foundation (NWO), the Early Research Programme of the Netherlands Organisation for Applied Scientific Research (TNO) and a TKI grant of the Dutch Topsectoren Program. The work at Purdue was funded by Microsoft Quantum.

5.7. Supplementary Material

5.7.1. Wafer growth

InSbAs quantum well heterostructures are grown in a Veeco Gen 930 molecular beam epitaxy (MBE) system equipped with valved crackers for As and Sb, and effusion cells for Ga, In, and Al. The growths are performed on GaAs (100) substrates with a 0.5° miscut toward the (111)B crystalline direction to minimize surface roughness [24]. The growth is initiated with a 100 nm thick GaAs buffer layer, directly followed by a 1 μm thick AlSb layer and a 4 μm thick $Al_{0.1}In_{0.9}Sb$ layer that also serves as bottom barrier for the InSbAs quantum wells. The AlSb and AlInSb layers help accommodate the large lattice mismatch between the GaAs substrate and InSbAs by forming a pseudo-substrate on which InSbAs can be coherently strained.

The growth rate for all the semiconducting layers is kept at roughly 0.5 ML/s, under group V element rich conditions. The incorporation of As and the resulting alloy content of the InSbAs quantum well is controlled by the growth temperature and the Sb/As flux ratio. The growth temperature is monitored by a BandiT spectrometer through blackbody radiation fitting. For the $x = 0.053$, 0.130 and 0.240 samples, the growth temperatures were 445 °C, 477 °C and 483 °C, respectively. While the Sb flux was kept around 4.2×10^{-7} Torr for all three samples to maintain group V overpressure, the As flux changed from 4.2×10^{-6} Torr ($x = 0.053$ and 0.130) to 1.1×10^{-5} Torr ($x = 0.240$). The semiconductor growth terminates under As rich conditions with the epitaxy of 2 ML InAs to prevent interdiffusion between the quantum well and the superconducting layer on top [17].

The heterostructures are then transferred under ultra-high vacuum to a Veeco 620 MBE system equipped with an Al effusion cell, and a quartz crystal monitor to determine the growth rate. Inside this MBE chamber, a moveable cryocooler is used to contact and cool the wafers down to liquid nitrogen temperature within a few hours [17]. After 6 hours of cooling, a 7 nm thin layer of Al is deposited on the semiconductor heterostructure with a typical growth rate of 0.3 Å/s. Immediately after the Al deposition, the samples are transferred into another chamber where they are oxidized for 15 min under an O_2 pressure of 5×10^{-5} Torr to stabilize the Al films [25].

High-resolution X-ray diffraction (HRXRD) measurements were performed to evaluate the As concentration, x, of the $InSb_{1-x}As_x$ quantum wells and reciprocal space maps were acquired to assess the strain of these layers. These measurements were performed

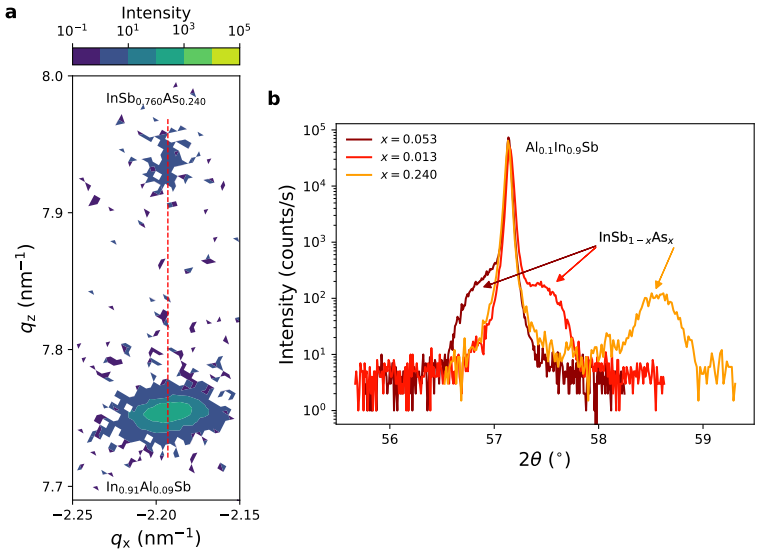

Figure 5.5: **a,** Asymmetric (115) reciprocal space map for the $InSb_{0.760}As_{0.240}$ quantum well heterostructure. **b,** High-resolution x-ray diffraction $2\theta - \omega$ scans obtained along (004) for the $InSb_{1-x}As_x$ quantum well heterostructures with different As concentrations.

using a X'pert PANalytical diffractometer with a copper X-ray tube operating at a wavelength $\lambda = 1.5406$ Å. Asymmetric (115) reciprocal space maps (averaged at 2 opposite azimuth angles $\phi = 0°$ and 180°) confirm that the $InSb_{1-x}As_x$ layers are coherently strained for the largest investigated composition $x = 0.240$, as shown in Fig. 5.5a, where the InSbAs peak is along the same red dashed vertical line as the 100 % relaxed AlInSb peak. Similar reciprocal space maps were obtained for the heterostructures with $x = 0.053$ and 0.130, confirming that InSbAs quantum wells are coherently and fully strained in the investigated composition range. $2\theta - \omega$ scans are presented in 5.5b. The peak positions of the coherently strained $InSb_{1-x}As_x$ layers give the As concentration for each sample, using the 4 micron fully relaxed $Al_{0.1}In_{0.9}Sb$ layer as the substrate in the analysis.

5.7.2. DEVICE FABRICATION

The processing of Sb-based 2DEGs in proximity to Aluminum is more challenging than InAs/Al systems. This is due to the potential intermixing of Al and Sb, which becomes more severe at elevated temperatures. We therefore need to ensure that all the processing steps (as described below) are performed at as low a temperature as possible. This includes room temperature "baking" of the resist for every lithography step, and low temperature atomic layer deposition.

The devices presented in the main text are fabricated using electron beam lithography. First, the Al and the 2DEG is etched in unwanted areas. The Al etch is performed in Transene D etchant at a temperature of 48.2 °C for 9 s. Subsequently, using the same PMMA mask, the 2DEG is etched in a wet etch solution consisting of 560 ml deionized water, 9.6 g citric acid powder, 5 ml H_2O_2 and 4 ml H_3PO_4. We etch for 2 min, resulting in an etch depth around 100 nm. A second Al etch is performed to define the normal regions using Transene D etchant at a temperature of 38.2 °C for 17 s. Next, a 60 nm thick SiN_x dielectric layer is sputtered for the Hall bars and the Josephson junction/spectroscopy devices. For the superconducting island and the quasi-1D superconducting strip we use a 40 nm thick AlO_x dielectric deposited by atomic layer deposition at 40 °C. Finally, top-gates are deposited by evaporating 10 nm/190 nm of Ti/Au.

5.7.3. Mobility and density

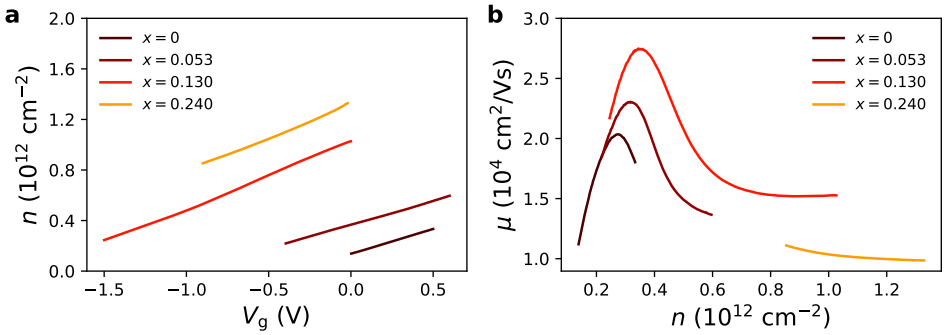

Figure 5.6: **a,** Electron density plotted against the gate voltage for all As concentrations. At a fixed gate voltage, the electron density increases monotonically with x. **b,** Electron mobility as a function of n.

The $InSb_{1-x}As_x$ 2DEGs are characterized by measuring the Hall effect in a gated Hall bar geometry at $T = 300$ mK. From a linear fit to the transversal resistance in a magnetic field range up to ±0.5 T, we extract the electron density, n, at every gate voltage, V_g. Figure 5.6a shows n plotted against V_g for all As concentrations, x. At a fixed gate voltage, the electron density increases systematically with x. The nominal density, $n(V_g = 0\,\text{V})$, increases from 0.15×10^{12} cm^{-2} for $x = 0$, to 1.35×10^{12} cm^{-2} for $x = 0.240$. This suggests that the incorporation of As causes an increasing negative band offset at the dielectric-2DEG interface.

Using the longitudinal resistivity, we calculate the mobility, μ, at every gate voltage. Figure 5.6b shows a plot of μ as a function of n for all As concentrations. We observe peak mobilities between 20 000 cm^2/Vs and 28 000 cm^2/Vs (the peak mobility for $x = 0.240$ could not be reached because of gate leakage). The peak mobilities occur around $n = 0.35 \times 10^{12}$ cm^{-2}, with a slight trend of moving towards higher densities for higher As

concentrations. We attribute the peak mobilities to the de-population of the second subband.

5.7.4. EFFECT OF ELECTRON DENSITY ON SPIN-ORBIT COUPLING

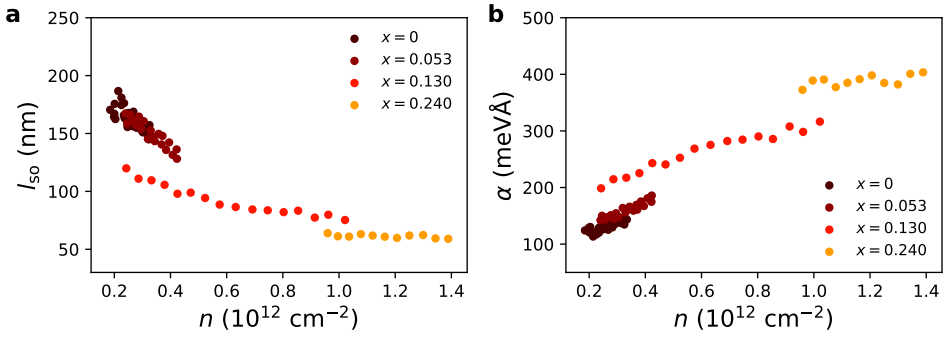

Figure 5.7: **a,** Spin-orbit length plotted against the electron density for all As concentrations. **b,** Linear Rashba parameter plotted against n. When comparing at the same density, l_{so} (α) decreases (increases) for increasing As concentration.

In Fig. 2 of the main text we show the spin-orbit length, l_{so}, and the linear Rashba paramter, α, plotted against the gate voltage for all As concentrations, x. In Fig. 5.7a and b we show l_{so} and α plotted against the electron density, n, respectively. When comparing at the same density, the overall trend of decreasing (increasing) l_{so} (α) with increasing As concentration persists.

5.7.5. EFFECTIVE MASS AND G-FACTOR

We extract the effective mass, m^*, of the electrons in the $InSb_{1-x}As_x$ 2DEGs by measuring the temperature dependence of the Shubnikov-de Haas (SdH) oscillations amplitude in gated Hall bars. Figure 5.8a shows the longitudinal resistivity, ρ_{xx}, as a function of perpendicular magnetic field, B, for $x = 0.130$ at a fixed density of $n = 3.41 \times 10^{11}$ cm^{-2}, close to peak mobility. The temperature ranges from $T = 4$ K to 40 K. The same measurement is also done for $x = 0$ at $n = 2.93 \times 10^{11}$ cm^{-2} (for $T = 1.7$ K to 17.3 K). After a polynomial background subtraction, the effective mass can be obtained from a fit to the thermal damping of the SdH oscillation amplitude, $\Delta\rho_{xx}$, normalized to the zero-field magnetoresistance value, $\rho_{xx,0}(T)$, at a fixed filling factor, ν, using [26]:

$$\frac{\Delta\rho_{xx}(T)}{\rho_{xx,0}(T)} \propto \frac{\alpha T}{\sinh(\alpha T)},$$

Here, $\alpha = \pi k_B m^* \nu/(\hbar^2 n)$, where k_B is the Boltzmann constant and $\hbar$ is the Planck constant. Figure 5.8b shows such fits for the $\nu = 6$ minima (circles) and maxima (rhombs)

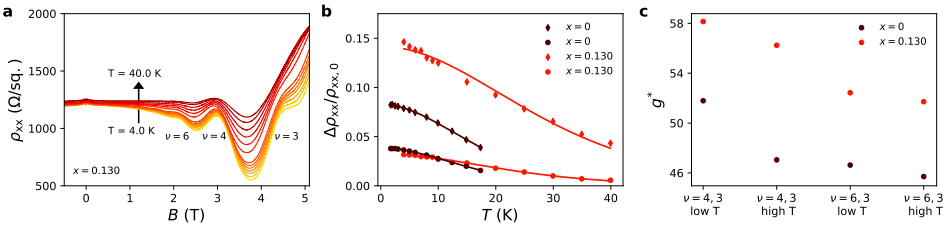

Figure 5.8: **a,** Shubnikov-de Haas oscillations for temperatures ranging from 4 K to 40 K for the $x = 0.130$ sample at a fixed density of $n = 3.41 \times 10^{11}$ cm^{-2} close to peak mobility. **b,** Temperature dependence of the oscillation amplitude for the $\nu = 6$ minima (circles) and maxima (rhombs) for $x = 0$ and $x = 0.130$. The solid lines are fits to the data in order to obtain the effective mass. **c,** g-factor, g^*, for $x = 0$ and $x = 0.130$ considering the even-odd filling factor couple $\nu = 4-3$ and $\nu = 6-3$. The fits are performed in a high and low temperature range.

5

for $x = 0$ and $x = 0.130$. The resulting effective mass is lower for the ternary sample, with a weighted mean value of $m^* = (0.0162 \pm 0.0004)\, m_0$, where m_0 is the free electron mass. The $x = 0$ sample shows a heavier effective mass of $m^* = (0.0180 \pm 0.0002)\, m_0$.

We proceed by extracting the g-factor, g^*, from the temperature dependence of the SdH oscillations, extending the temperature range from $T = 1.7$ K to 44.7 K. Using the method reported in [23], an expression for g^* can be obtained by combining the equations for the thermal activation energy of an even-odd filling factor couple. We consider the filling factor couples $\nu = 4-3$ and $\nu = 6-3$. Since we find different activation energies from the linear fit of $\ln(\rho_{xx})$ vs. $1/T$ depending on the temperature range, we report in Fig. 5.8c the extracted values for the low- and high-temperature ranges. The m^* values we found earlier are used in the g^* calculation. We find an average g-factor of $g^* = 47.8 \pm 2.8$ for $x = 0$, and $g^* = 54.6 \pm 3.1$ for $x = 0.130$.

5.7.6. Multiple Andreev reflections

In Fig. 3b and c of the main text we show a representative Fraunhofer interference pattern and a gate dependence of the switching current for a Josephson junction with $x = 0.053$. As demonstrated in Fig. 5.9, we observe pronounced subgap conductance modulations that are due to multiple Andreev reflections (MAR) for all As concentrations. The observation of higher order MAR shows that transport is phase-coherent across a length scale of several times the junction length.

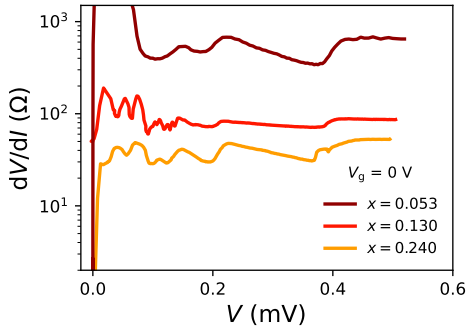

Figure 5.9: Differential resistance plotted against the voltage drop between the two Al leads for the JJs with $x = 0.053$, 0.130 and 0.240. All measurements are obtained at a JJ gate voltage of $V_g = 0$ V. The curve for $x = 0.130$ is offsetted for clarity. MAR up to several orders are observed for all As concentrations.

REFERENCES

1. Lutchyn, R. M., Sau, J. D. & Das Sarma, S. Majorana Fermions and a Topological Phase Transition in Semiconductor-Superconductor Heterostructures. *Phys. Rev. Lett.* **105,** 077001 (2010).
2. Oreg, Y., Refael, G. & von Oppen, F. Helical Liquids and Majorana Bound States in Quantum Wires. *Phys. Rev. Lett.* **105,** 177002 (2010).
3. Aguado, R. Majorana quasiparticles in condensed matter. *La Rivista del Nuovo Cimento* **40,** 523–593 (2017).
4. Lutchyn, R. M., Bakkers, E. P. A. M., Kouwenhoven, L. P., Krogstrup, P., Marcus, C. M. & Oreg, Y. Majorana zero modes in superconductor–semiconductor heterostructures. *Nature Reviews Materials* **3,** 52–68 (2018).
5. Prada, E., San-Jose, P., de Moor, M. W. A., Geresdi, A., Lee, E. J. H., Klinovaja, J., Loss, D., Nygård, J., Aguado, R. & Kouwenhoven, L. P. From Andreev to Majorana bound states in hybrid superconductor–semiconductor nanowires. *Nature Reviews Physics* **2,** 575–594 (2020).
6. Nichele, F., Drachmann, A. C. C., Whiticar, A. M., O'Farrell, E. C. T., Suominen, H. J., Fornieri, A., Wang, T., Gardner, G. C., Thomas, C., Hatke, A. T., Krogstrup, P., Manfra, M. J., Flensberg, K. & Marcus, C. M. Scaling of Majorana Zero-Bias Conductance Peaks. *Phys. Rev. Lett.* **119,** 136803 (2017).
7. O'Farrell, E. C. T., Drachmann, A. C. C., Hell, M., Fornieri, A., Whiticar, A. M., Hansen, E. B., Gronin, S., Gardner, G. C., Thomas, C., Manfra, M. J., Flensberg, K., Marcus, C. M. & Nichele, F. Hybridization of Subgap States in One-Dimensional Superconductor-Semiconductor Coulomb Islands. *Phys. Rev. Lett.* **121,** 256803 (2018).
8. Pankratova, N., Lee, H., Kuzmin, R., Wickramasinghe, K., Mayer, W., Yuan, J., Vavilov, M. G., Shabani, J. & Manucharyan, V. E. Multiterminal Josephson Effect. *Phys. Rev. X* **10,** 031051 (2020).
9. Fornieri, A., Whiticar, A. M., Setiawan, F., Portolés, E., Drachmann, A. C. C., Keselman, A., Gronin, S., Thomas, C., Wang, T., Kallaher, R., Gardner, G. C., Berg, E., Manfra, M. J., Stern, A., Marcus, C. M. & Nichele, F. Evidence of topological superconductivity in planar Josephson junctions. *Nature* **569,** 89–92 (2019).
10. Ren, H., Pientka, F., Hart, S., Pierce, A. T., Kosowsky, M., Lunczer, L., Schlereth, R., Scharf, B., Hankiewicz, E. M., Molenkamp, L. W., Halperin, B. I. & Yacoby, A. Topological superconductivity in a phase-controlled Josephson junction. *Nature* **569,** 93–98 (2019).

11. Shabani, J., Kjaergaard, M., Suominen, H. J., Kim, Y., Nichele, F., Pakrouski, K., Stankevic, T., Lutchyn, R. M., Krogstrup, P., Feidenhans'l, R., Kraemer, S., Nayak, C., Troyer, M., Marcus, C. M. & Palmstrøm, C. J. Two-dimensional epitaxial superconductor-semiconductor heterostructures: A platform for topological superconducting networks. *Phys. Rev. B* **93,** 155402 (2016).

12. Kjaergaard, M., Nichele, F., Suominen, H. J., Nowak, M. P., Wimmer, M., Akhmerov, A. R., Folk, J. A., Flensberg, K., Shabani, J., Palmstrøm, C. J. & Marcus, C. M. Quantized conductance doubling and hard gap in a two-dimensional semiconductor–superconductor heterostructure. *Nature Communications* **7,** 12841 (2016).

13. Ke, C. T., Moehle, C. M., de Vries, F. K., Thomas, C., Metti, S., Guinn, C. R., Kallaher, R., Lodari, M., Scappucci, G., Wang, T., Diaz, R. E., Gardner, G. C., Manfra, M. J. & Goswami, S. Ballistic superconductivity and tunable π–junctions in InSb quantum wells. *Nature Communications* **10,** 3764 (2019).

14. Schuwalow, S., Schröter, N. B. M., Gukelberger, J., Thomas, C., Strocov, V., Gamble, J., Chikina, A., Caputo, M., Krieger, J., Gardner, G. C., Troyer, M., Aeppli, G., Manfra, M. J. & Krogstrup, P. Band Structure Extraction at Hybrid Narrow-Gap Semiconductor–Metal Interfaces. *Advanced Science* **8,** 2003087 (2021).

15. Goldammer, K., Chung, S., Liu, W., Santos, M., Hicks, J., Raymond, S. & Murphy, S. High-mobility electron systems in remotely-doped InSb quantum wells. *Journal of Crystal Growth* **201-202,** 753–756 (1999).

16. Lehner, C. A., Tschirky, T., Ihn, T., Dietsche, W., Keller, J., Fält, S. & Wegscheider, W. Limiting scattering processes in high-mobility InSb quantum wells grown on GaSb buffer systems. *Phys. Rev. Materials* **2,** 054601 (2018).

17. Thomas, C., Diaz, R. E., Dycus, J. H., Salmon, M. E., Daniel, R. E., Wang, T., Gardner, G. C. & Manfra, M. J. Toward durable Al-InSb hybrid heterostructures via epitaxy of 2ML interfacial InAs screening layers. *Phys. Rev. Materials* **3,** 124202 (2019).

18. Iordanskii, S. V., Lyanda-Geller, Y. B. & Pikus, G. E. Weak-Localization in Quantum-Wells With Spin-Orbit Interaction. *Zh. Eksp. Teor. Fiz.* **60,** 199–203 (1994).

19. Knap, W., Skierbiszewski, C., Zduniak, A., Litwin-Staszewska, E., Bertho, D., Kobbi, F., Robert, J. L., Pikus, G. E., Pikus, F. G., Iordanskii, S. V., Mosser, V., Zekentes, K. & Lyanda-Geller, Y. B. Weak antilocalization and spin precession in quantum wells. *Phys. Rev. B* **53,** 3912–3924 (1996).

20. Winkler, G. W., Wu, Q., Troyer, M., Krogstrup, P. & Soluyanov, A. A. Topological Phases in $InAs_{1-x}Sb_x$: From Novel Topological Semimetal to Majorana Wire. *Phys. Rev. Lett.* **117,** 076403 (2016).

21. Mayer, W., Schiela, W. F., Yuan, J., Hatefipour, M., Sarney, W. L., Svensson, S. P., Leff, A. C., Campos, T., Wickramasinghe, K. S., Dartiailh, M. C., Žutić, I. & Shabani, J. Superconducting Proximity Effect in InAsSb Surface Quantum Wells with In Situ Al Contacts. *ACS Applied Electronic Materials* **2,** 2351–2356 (2020).

22. Sestoft, J. E., Kanne, T., Gejl, A. N., von Soosten, M., Yodh, J. S., Sherman, D., Tarasinski, B., Wimmer, M., Johnson, E., Deng, M., Nygård, J., Jespersen, T. S., Marcus, C. M. & Krogstrup, P. Engineering hybrid epitaxial InAsSb/Al nanowires for stronger topological protection. *Phys. Rev. Materials* **2,** 044202 (2018).

23. Drichko, I. L., Dmitriev, A. A., Malysh, V. A., Smirnov, I. Y., von Känel, H., Kummer, M., Chrastina, D. & Isella, G. Effective g factor of 2D holes in strained Ge quantum wells. *Journal of Applied Physics* **123,** 165703 (2018).

24. Shi, Y., Bergeron, E., Sfigakis, F., Baugh, J. & Wasilewski, Z. Hillock-free and atomically smooth InSb QWs grown on GaAs substrates by MBE. *Journal of Crystal Growth* **513,** 15–19 (2019).

25. Gazibegovic, S., Car, D., Zhang, H., Balk, S. C., Logan, J. A., de Moor, M. W. A., Cassidy, M. C., Schmits, R., Xu, D., Wang, G., Krogstrup, P., Op het Veld, R. L. M., Zuo, K., Vos, Y., Shen, J., Bouman, D., Shojaei, B., Pennachio, D., Lee, J. S., van Veldhoven, P. J., Koelling, S., Verheijen, M. A., Kouwenhoven, L. P., Palmstrøm, C. J. & Bakkers, E. P. A. M. Epitaxy of advanced nanowire quantum devices. *Nature* **548,** 434–438 (2017).

26. De Lange, W., Blom, F. A. P. & Wolter, J. H. Effective electron mass in GaAs/AlxGa1-xAs heterostructures under hydrostatic pressure. *Semiconductor Science and Technology* **8,** 341–343 (1993).

6

CONTROLLING ANDREEV BOUND STATES WITH THE MAGNETIC VECTOR POTENTIAL

Christian M. Moehle*, Prasanna K. Rout*, Nayan A. Jainandunsing, Dibyendu Kuiri, Chung Ting Ke, Di Xiao, Candice Thomas, Michael J. Manfra, Michał P. Nowak, Srijit Goswami

Tunneling spectroscopy measurements are often used to probe the energy spectrum of Andreev bound states (ABSs) in semiconductor-superconductor hybrids. Recently, this spectroscopy technique has been incorporated into planar Josephson junctions (JJs) formed in two-dimensional electron gases, a potential platform to engineer phase-controlled topological superconductivity. Here, we perform ABS spectroscopy at the two ends of planar JJs and study the effects of the magnetic vector potential on the ABS spectrum. We show that the local superconducting phase difference arising from the vector potential is equal in magnitude and opposite in sign at the two ends, in agreement with a model that assumes localized ABSs near the tunnel barriers. Complemented with microscopic simulations, our experiments demonstrate that the local phase difference can be used to estimate the relative position of localized ABSs separated by a few hundred nanometers.

This chapter has been published in Nano Letters 22, 8601–8607 (2022).

*These authors contributed equally to this work.

6.1. INTRODUCTION

Hybrid structures composed of superconductors and normal conductors host Andreev bound states (ABSs) [1–3]. These states are superpositions of electron-like and hole-like excitations, with energies lower than the superconducting gap. In recent years, superconductor-semiconductor hybrids have emerged as an appealing platform to manipulate these bound states. For example, controllable coupling between individual ABSs has led to the creation of Andreev molecules [4–7], and Josephson junctions (JJs) based on these hybrids have been combined with superconducting circuits to realize Andreev qubits [8, 9].

In JJs, the microscopic properties of ABSs determine global properties of the junction, such as its critical current [2]. The energy of ABSs is dependent on the phase difference between the superconducting leads, which can be tuned by the application of a magnetic flux through a superconducting loop connecting the leads. In planar JJs, the vector potential of the magnetic field leads to streams of positive and negative current, to the formation of Josephson vortices, and to the well-known Fraunhofer interference pattern in critical current [10–12]. It has been proposed that such planar JJs can host Majorana bound states [13–16], and that the location and coupling of these states can be controlled via the vector potential [17].

In order to investigate how the vector potential modifies ABSs in a JJ, one needs experimental techniques that provide information about the spatial extent and location of ABSs. Studies in junctions that simultaneously probe the spatial distribution and the energy spectrum of ABSs have mainly been performed using scanning probe techniques [18, 19], and more recently, via local tunnel probes in two-dimensional electron gases (2DEGs) [20, 21].

Here, we perform tunneling spectroscopy at both ends of planar JJs embedded in a superconducting loop, allowing us to probe the effects of the magnetic vector potential on the phase-dependence of the ABS energy. We directly show that the local superconducting phase difference originating from the vector potential has equal magnitude but opposite sign at the two ends of the JJ. This is manifested by a striking difference in the spectroscopy maps obtained from each side, in excellent agreement with a model that assumes tunnel coupling to a single ABS localized at each end. Microscopic numerical simulations confirm that such a localization of the ABSs is indeed expected, and that the tunneling current is only sensitive to ABSs located near the ends of the JJ. By modifying the potential landscape in the vicinity of the tunnel probe, we show that the local phase difference allows us to resolve multiple ABSs within a spatial extent of a few hundred nanometers, in qualitative agreement with simulations.

6.2. RESULTS

The JJs are fabricated using an $InSb_{0.92}As_{0.08}$ 2DEG with in-situ grown Al as the superconductor (details about the molecular beam epitaxy growth of the heterostructure can

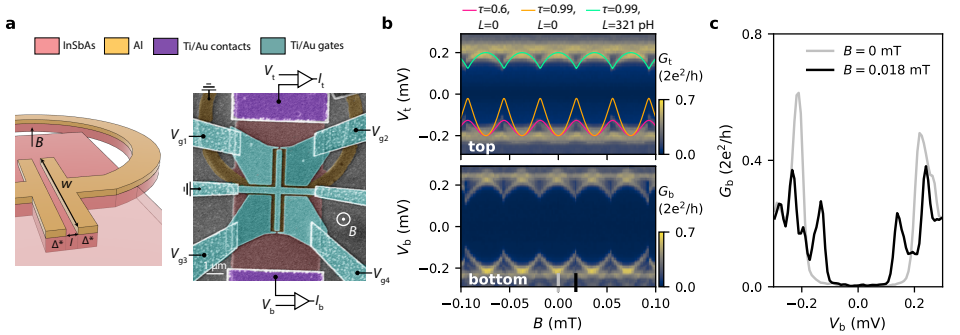

Figure 6.1: Tunneling spectroscopy at the two ends of a planar phase-biased JJ. **a,** Schematic (before the gate deposition) and false-colored SEM of Dev 1. **b,** Spectroscopy maps measured at the top ($V_{g1} = -0.39\,\mathrm{V}$, $V_{g2} = -0.74\,\mathrm{V}$, $V_{g3} = 0\,\mathrm{V}$, $V_{g4} = 0\,\mathrm{V}$) and bottom end of the JJ ($V_{g1} = 0\,\mathrm{V}$, $V_{g2} = 0\,\mathrm{V}$, $V_{g3} = -1.1\,\mathrm{V}$, $V_{g4} = -0.6\,\mathrm{V}$). The three curves in the top panel correspond to single-channel ABS spectra calculated for different combinations of transmission (τ) and loop inductance (L) as specified in the legend. **c,** Line cuts of the bottom spectroscopy map at the indicated positions in **b**.

6

be found in [22]). Figure 6.1a shows a schematic and a false-colored scanning electron micrograph (SEM) of such a device. To fabricate the devices, we first use a combination of Al and 2DEG etches to define the JJ and the superconducting loop. The exposed 2DEG on the top and bottom sides of the JJ is contacted by Ti/Au, and the Al loop is contacted by NbTiN, resulting in a three-terminal device. A globally deposited layer of AlO_x forms the gate dielectric. Lastly, split gates are evaporated on the top and bottom ends of the JJ, allowing us to define tunnel barriers, while also depleting the 2DEG around the junction. A central gate (kept grounded throughout this study) covers the normal section of the JJ. We study two JJs (Dev 1 and Dev 2), both with length $l = 80\,\mathrm{nm}$ and width $w = 5\,\mu\mathrm{m}$. More details about the device fabrication can be found in section 6.4.1. The devices are measured in a dilution refrigerator with a base temperature of 30 mK using standard lock-in techniques.

In Fig. 6.1b (top panel) we present a tunneling spectroscopy map for Dev 1 at the top end of the JJ. The conductance, $G_\mathrm{t} = \mathrm{d}I_\mathrm{t}/\mathrm{d}V_\mathrm{t}$, is measured as a function of voltage bias, V_t, and perpendicular magnetic field, B. The bottom panel shows the conductance measured at the bottom end, $G_\mathrm{b} = \mathrm{d}I_\mathrm{b}/\mathrm{d}V_\mathrm{b}$, with representative line cuts presented in Fig. 6.1c. In both maps we see a superconducting gap that is modulated by B, with an oscillation period equal to Φ_0/S, where $\Phi_0 = h/2e$ is the magnetic flux quantum and S is the area of the superconducting loop. This modulation indicates the presence of flux-periodic ABSs in the JJ. For a normal region much shorter than the superconducting coherence length, the relation between the ABS energy and the gauge-invariant phase difference between the two superconducting leads, φ, is given by [2]:

$$E_n(\varphi) = \pm\Delta^* \sqrt{1 - \tau_n \sin^2(\varphi/2)}, \tag{6.1}$$

where Δ^* is the induced gap in the 2DEG regions below the Al leads and τ_n is the transmission probability of the n^{th} conduction channel. The flux through the loop, $\Phi = BS$, and φ are related via $\varphi = 2\pi\Phi/\Phi_0$. The relatively small modulation depth observed in the experiment might suggest low-transmission ABSs [see the field evolution of a single ABS with $\tau = 0.6$ (pink) and $\tau = 0.99$ (orange) in Fig. 6.1b]. However, when looking more closely at the energy minima, we find that they display pronounced cusps, not expected from Eq. 6.1. These cusps are indicative of phase slips that occur when the superconducting loop has a sizeable inductance, L, whereby the standard linear flux-phase relation no longer holds. We independently estimate $L = 321$ pH (see section 6.4.2) and use the appropriate flux-phase conversion (see section 6.4.6) to find that the measured ABS spectrum is consistent with a large transparency of $\tau = 0.99$ (light green line in Fig. 6.1b). We further confirm this by performing spectroscopy at higher B, as will be discussed later. This highlights the fact that the inductance, which can be significant in thin film superconductors, strongly affects the ABS spectra observed in experiments.

Thus far we have assumed that the superconducting phase difference is constant along the width of the JJ (see Fig. 6.2a for a top-view schematic of the junction). However, the vector potential of the magnetic field creates a phase gradient, $\phi'(y)$, and the total gauge-invariant phase difference is given by $\varphi(y) = \phi + \phi'(y)$, where ϕ is the phase difference that can be tuned by the flux through the loop. The position-dependent local phase difference can be expressed as [10, 23]:

$$\phi'(y) = -2\pi \frac{fBly}{\Phi_0}, \tag{6.2}$$

where f is a flux focusing factor that increases the effective magnetic flux in the JJ (see section 6.4.3 and [24]). This expression for φ is valid for JJs with a width much smaller than the Josephson penetration length, which is the case for our junctions (see section 6.4.4). The magnetic vector potential leads to the formation of localized ABSs with a well defined supercurrent direction (see section 6.4.7 for numerical simulations). Fig. 6.2b shows a plot of the expected local phase difference for Dev 1 at $B = 1$ mT, demonstrating that the phase difference experienced by an ABS located at the top and bottom end of the JJ will be significantly different. Therefore, for localized ABSs (as depicted in Fig. 6.2a), one expects observable differences in the field evolution of their energies. This is more clearly illustrated in Fig. 6.2c, where we plot the ABS energy, E, as a function of B. As B increases, the maxima for the top and bottom ABS shift relative to each other. This is a direct consequence of Eq. 6.2, whereby ABSs located at opposite ends of the JJ are sensitive to the local phase difference with equal magnitude but opposite sign.

With an understanding of the effect of the magnetic vector potential on the ABS spectrum, we now turn to spectroscopy measurements over a significantly larger field range (Fig. 6.3). Figure 6.3a and b show the top and bottom spectroscopy maps, respectively. We first look at the high field regime (Fig. 6.3a2 and b2), where the ABS oscillation amplitude has increased significantly (compare to 6.1b). This is caused by the Fraunhofer-like reduction of the critical current, I_c, thereby reducing the so-called screening parameter, $\beta \propto LI_c$. The lower β results in a linear flux-phase relation, making it possible to probe

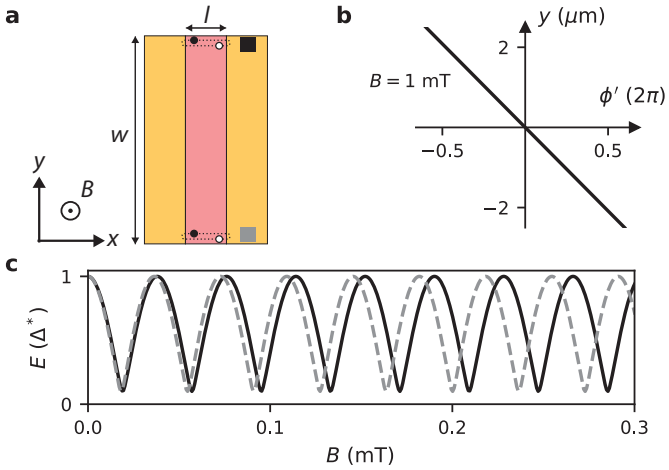

Figure 6.2: Effect of the magnetic vector potential. **a,** Top-view schematic of the JJ in Dev 1. Two ABSs located at the top and bottom end are indicated. **b,** Calculated local phase difference arising from the vector potential at $B = 1\,\mathrm{mT}$ ($f = 6.2$). **c,** Magnetic field evolution for the ABS located at the top (black) and bottom (grey), showing a relative shift due to the local phase difference.

6

the complete phase-dependence of the ABS (see section 6.4.6 for more details). The fact that the ABS energy reaches very close to zero confirms that the ABSs we are probing have extremely high transparency.

In the intermediate field range (see Fig. 6.3a1 and b1) we find that the cusps near the ABS minima develop into sharp jumps, resulting in a highly asymmetric and skewed shape away from $B = 0$. The skewness is not only reversed for positive and negative fields, but also for the top and bottom end of the JJ. Furthermore, we find that the ABS energy maxima shift in opposite directions in the top and bottom spectroscopy map, as expected for bound states localized at the edges. This is a strong indication that each probe is sensitive only to a region of limited spatial extent in its vicinity, and that it is in general difficult to reliably estimate bulk junction properties from a local spectroscopy measurement [25].

To explain these findings we introduce a model that takes into account the combined effects of the inductance and vector potential, and assumes that each tunnel probe couples only to a single localized ABS with $\tau = 0.99$ (a full description of the model can be found in section 6.4.6). The resulting ABS spectra are shown as light blue lines plotted on the spectroscopy maps of Fig. 6.3a and b. We find an excellent agreement between the model and the experiments in the entire magnetic field range. We show in section 6.4.6 that the observed reversal of the skewness can only occur when both the vector potential and the loop inductance are taken into account. Therefore, the loop inductance serves

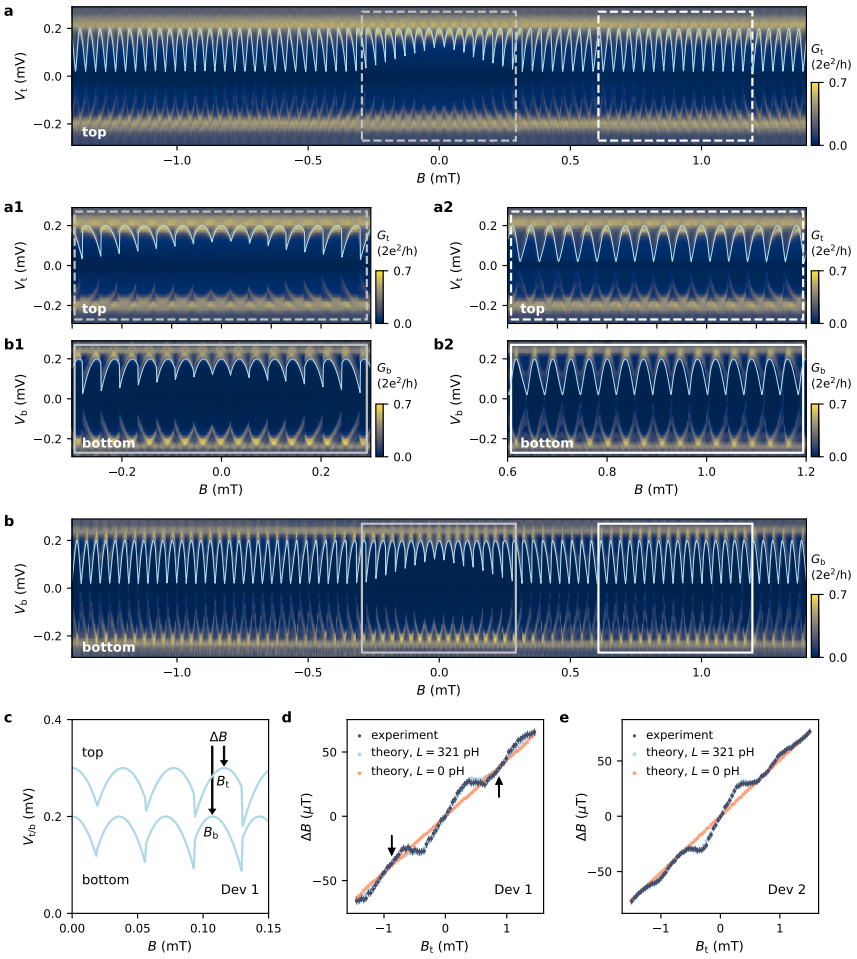

Figure 6.3: Tunneling spectroscopy over a large magnetic field range. **a,** Spectroscopy map at the top end of Dev 1 ($V_{g1} = -0.39\,\mathrm{V}$, $V_{g2} = -0.74\,\mathrm{V}$, $V_{g3} = 0\,\mathrm{V}$, $V_{g4} = 0\,\mathrm{V}$), with zoomed-in views presented in **a1** and **a2**. **b,** Spectroscopy map at the bottom end ($V_{g1} = 0\,\mathrm{V}$, $V_{g2} = 0\,\mathrm{V}$, $V_{g3} = -1.1\,\mathrm{V}$, $V_{g4} = -0.6\,\mathrm{V}$) with zoom-in views in **b1** and **b2**. The model (light blue lines) assumes coupling to a single ABS ($\tau = 0.99$), taking into account the local phase difference in the JJ and the loop inductance ($L = 321\,\mathrm{pH}$). **c,** Model curves for the top and bottom end plotted together (offsetted vertically for clarity). The ABS maxima on the top (B_t) and bottom (B_t) are shifted. **d-e,** $\Delta B = B_t - B_b$ as a function of B_t for Dev 1 and Dev 2 (dark blue circles). We also include the ΔB values from the toy model with $L = 321\,\mathrm{pH}$ (light blue circles), and $L = 0$ (red circles). The arrows indicate the position of the first Fraunhofer node.

as an extremely useful tool to clearly see the effects of a spatially varying phase difference along the JJ.

In order to systematically analyze the difference between the energy spectra of the top and bottom ABS, we introduce the quantity $\Delta B = B_t - B_b$ (see Fig. 6.3c). In Fig. 6.3d, we plot ΔB as a function of B_t for experiment (dark blue circles) and theory (light blue circles). Both show a non-linear dependence, which can be well accounted for by the variation of I_c (and hence β). It is interesting to note that while our device geometry makes it impossible to directly measure I_c of the JJ, the nodes in the Fraunhofer pattern can still be identified by regions where $\beta \approx 0$ (see arrows), and therefore the experiment/theory plots with finite L approach the theory curve with $L = 0$ (red circles). All of these findings are reproduced in Dev 2 (see spectroscopy maps in section 6.4.5 and the ΔB analysis in Fig. 6.3e).

Although our toy model is effective in capturing the most important features observed in experiments, it relies on the assumption that the tunnel probes couple to a single localized ABS in the vicinity of the barriers. In the following, we use numerical simulations to show that the tunneling current is indeed dominated by edge-located ABSs, and that the phase shifts for these states agree with the experiments. For the simulations, we consider a planar JJ composed of two semi-infinite superconducting leads and a normal region that is connected to two normal leads through tunneling barriers. We calculate the conductance from the top (bottom) normal lead, G_t (G_b), by tracing the quasiparticles entering and leaving the top (bottom) lead. In the simulation, we include the effect of a perpendicular magnetic field and disorder, which results in a finite mean free path, l_e. A superconducting phase difference, ϕ, is imposed between the superconducting terminals (more details about the model can be found in section 6.4.7).

We first consider a ballistic JJ with infinite mean free path. In Fig. 6.4a and b, we show the conductance calculated from the top and bottom, respectively, at $B = 1\,\mathrm{mT}$. In both maps, the main resonance is shifted by an equal amount in ϕ, but in opposite directions. This shift agrees very well with our toy model (black lines), where we assumed tunnel-coupling to a single ABS localized at the top/bottom end of JJ. The presence of localized ABSs is clearly seen by inspecting the supercurrent distribution calculated at the energy/phase values denoted by the colored circles in Fig. 6.4a. We find that the top probe is only sensitive to the ABSs located in the vicinity of the top barrier (see Fig. 6.4c).

To make a connection with the experiments, we also consider a semiconductor with $l_e = 150\,\mathrm{nm}$, a good estimate for the mean free path in our 2DEGs [22]. The top and bottom conductances are shown in 6.4d and e, respectively. As in the ballistic case, we again find a predominant sensitivity to edge-located ABSs, and a relative shift of the ABS maxima. However, we also note two important differences. Firstly, unlike the ballistic case, the ABS spectra at the top and bottom are now drastically different from each other. This is not surprising, given the fact that the ABSs can be sensitive to the particular disorder configuration present at each end. Secondly, the main resonance splits into more clearly distinguishable ABSs. These ABSs are also localized close to the top/bottom end of JJ,

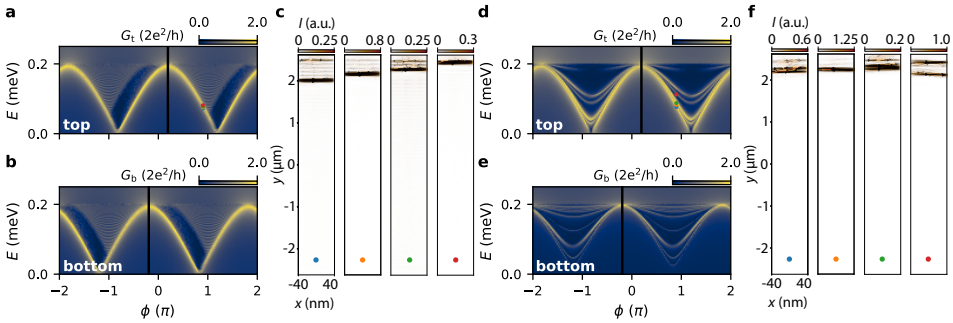

Figure 6.4: Numerical simulation of the tunneling conductance for a ballistic and disordered JJ. **a-b,** Conductance maps at $B = 1\,\mathrm{mT}$ for a ballistic JJ probed from the top and bottom. The black lines correspond to the phase shifts expected from the toy model. **c,** Supercurrent distribution in the normal region of the JJ obtained for the E and ϕ values denoted with the circles in **a**. **d-e,** Conductance maps at $B = 1\,\mathrm{mT}$ for a disordered JJ ($l_e = 150\,\mathrm{nm}$) probed from the top and bottom. **f,** Supercurrent distributions for the E and ϕ values denoted with the circles in **d**.

6

as seen in Fig. 6.4f. The specific location of these states is sensitive to the local potential landscape. However, we expect them to acquire different relative phase shifts depending on their precise location in the JJ.

This spatially dependent phase shift in the vicinity of the tunnel probe can also be experimentally observed. Figure 6.5a presents spectroscopy measurements on the top end of Dev 2, where the split gate settings have been modified to locally alter the disorder landscape. At $B = 0$ (central panel), distinct ABSs are hardly visible (see also black line cut in Fig. 6.5b). However, when increasing the magnetic field (left and right panel), the localized ABSs acquire different phase shifts making it possible to resolve them more clearly (see also gray line cut in Fig. 6.5b). Reversing the field direction leads to ABSs shifted in the opposite direction, as expected for spatially separated ABSs. A similar pattern of ABSs located at different positions close to the edge of the junction and experiencing different phase shifts is obtained in the numerical calculation shown in Fig. 6.5c and d. This demonstrates that the effect of the vector potential (and resulting local phase difference) can indeed be used to estimate the location of the ABSs in the JJ. Around $B = 2.09\,\mathrm{mT}$, the maxima of the two states (indicated by the brown and pink circles) are shifted by $\approx 5\,\mu\mathrm{T}$. This shift can be translated into an estimate of their spatial separation by using the spectroscopy results at the two extreme ends of the JJ (Fig. S4 and Fig. 6.3e), where we find $\Delta B = 106\,\mu\mathrm{T}$ at $B = 2.09\,\mathrm{mT}$ for ABSs separated by $5\,\mu\mathrm{m}$. Using this, we can estimate the spatial separation of the two states indicated by the brown and pink circles to be approximately 250 nm.

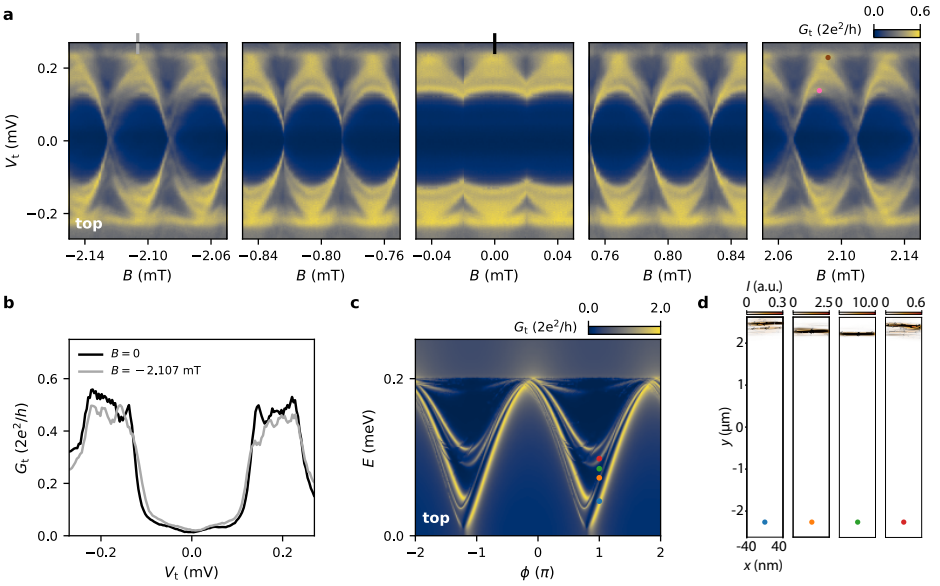

Figure 6.5: Probing spatially separated ABSs. **a,** Tunneling spectroscopy maps at the top end of Dev 2 ($V_{g1} = -1.90\,\mathrm{V}$, $V_{g2} = -1.40\,\mathrm{V}$, $V_{g3} = -2.10\,\mathrm{V}$, $V_{g4} = -1.43\,\mathrm{V}$). The ABSs that are initially hardly resolvable around $B = 0$ are better resolved at larger B, where localized ABSs acquire different phase shifts depending on their location in the JJ. **b,** Line cuts at two indicated positions in **a** showing this improvement in resolution. **c,** Simulated tunneling conductance map for a disordered JJ ($l_e = 150\,\mathrm{nm}$) at $B = 10\,\mathrm{mT}$ probed from the top. **d,** Supercurrent distributions for the E and ϕ values marked by circles in **c**, showing how localized ABSs at different positions correspond to ABS spectra that are shifted in ϕ.

6.3. CONCLUSION

In conclusion, we employed local tunneling spectroscopy at two ends of planar phase-biased JJs to study the influence of the magnetic vector potential on the ABS spectrum. The combined effect of inductance and a spatially varying local phase difference results in striking differences in the tunneling spectra measured at the two edges of these junctions. Supporting our experiments with a theoretical toy model and microscopic numerical simulations, we showed that our results are consistent with the measurement of ABSs localized at the ends of the JJ, in the vicinity of the tunnel barriers. Finally, we showed that the effects of the vector potential are not only observable for ABSs separated by microns, but can also be used to estimate the relative locations of ABSs separated by a few hundred nanometers. Our results provide insights into the effects of a spatially varying phase difference on the ABS spectrum in extended JJs, and are relevant for ongoing efforts on investigating topological superconductivity in planar JJs.

Additional Note: During the preparation of this manuscript, we became aware of a related work on tunneling spectroscopy in planar JJs [26].

DATA AVAILABILITY

Raw data and analysis scripts for all presented figures are available at the 4TU.ResearchData repository: https://doi.org/10.4121/20059364.

AUTHOR CONTRIBUTIONS

C.M.M. and C.T.K. fabricated the devices. **C.M.M.**, P.K.R. and N.A.J. performed the measurements and analyzed the data. S.G. supervised the experimental work. The numerical simulations were performed by D.K. under the supervision of M.P.N. who also provided the toy model. The semiconductor heterostructure was grown by D.X. and C.T. under the supervision of M.J.M. The manuscript was written by **C.M.M.**, P.K.R., D.K., M.P.N. and S.G. with input from all authors.

ACKNOWLEDGMENTS

We thank T. Dvir, G. Wang and C. Prosko for fruitful discussions. The research at Delft was supported by the Dutch National Science Foundation (NWO), the Early Research Programme of the Netherlands Organisation for Applied Scientific Research (TNO) and a TKI grant of the Dutch Topsectoren Program. The work at Purdue was funded by Microsoft Quantum. The research at Krakow was supported by National Science Centre (NCN) agreement number UMO-2020/38/E/ST3/00418.

6.4. SUPPLEMENTARY MATERIAL

6.4.1. DEVICE FABRICATION

The two phase-biased JJs (Dev 1, Dev 2) and the DC SQUID are fabricated using electron beam lithography. Due to a possible intermixing of Al and Sb we perform all fabrication steps at room temperature unless stated otherwise. The device fabrication starts by etching the Al and the 2DEG in unwanted areas. The Al etch is performed in Transene D etchant at a temperature of 48.2 °C for 9 s resulting a etching thickness of 100 nm. Afterwards, using the same PMMA mask, the 2DEG is etched in a solution of 560 ml deionized water, 9.6 g citric acid powder, 5 ml H_2O_2 and 4 ml H_3PO_4, using an etching time of 90 s. To define the JJs, we perform a second Al etch, carried out in 38.2 °C Transene D for 16 s. This is followed by sputtering a 60 nm thick layer of SiN_x that partly covers the superconducting loop, isolating it from the intended 2DEG contact inside the loop. Next, we contact the exposed 2DEG region on the top and bottom side of the JJ by Ti/Au. Prior to the evaporation of 10 nm Ti and 190 nm Au, a gentle Ar etching is performed in the loadlock of the evaporator to remove any oxides that might have formed on the 2DEG. Afterwards, we contact the superconducting loop by sputtering 150 nm of NbTiN (before the sputter process an in-situ Ar etch is performed to remove the oxide on the Al). As the gate dielectric, we deposit a global layer (40 nm thick) of AlO_x by atomic layer deposition at 40 °C. The gates are formed in two steps: First, the fine structures (split gates and central gate) are deposited by evaporating 10 nm of Ti and 40 nm of Au. In the second step,

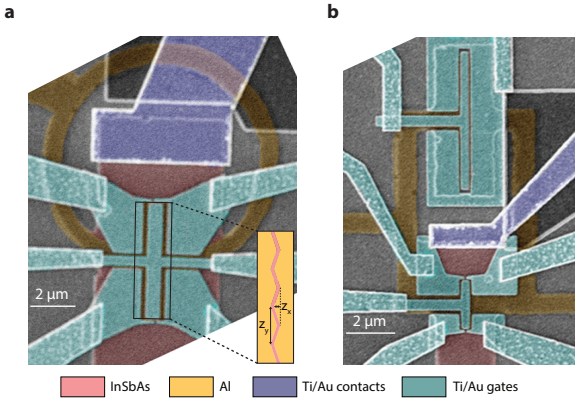

Figure 6.6: **a,** SEM of Dev 2 having a zigzag-shaped normal region with a length of $l = 80\,\text{nm}$ and width of $w = 5\,\mu\text{m}$. **b,** SEM of the DC SQUID. The device JJ (on the bottom) has dimensions $l = 120\,\text{nm}$ and $w = 2\,\mu\text{m}$. The reference JJ (on the top) has dimensions $l = 80\,\text{nm}$ and $w = 5\,\mu\text{m}$.

10 nm Ti and 100 nm Au are evaporated to define the gate leads.

A schematic and false-colored SEM of Dev 1 is shown in Fig. 1a of the main text. In Fig. 6.6a we present a SEM of Dev 2, which is similar to Dev 1. The main difference is that the normal region of the JJ is slightly zigzag-shaped ($z_x = 0.24\,\mu\text{m}$, $z_y = 1.43\,\mu\text{m}$). This was originally introduced into this device to potentially suppress long quasiparticle trajectories and thereby increase the size of the topological gap [27]. The superconducting leads of Dev 1 and Dev 2 have a length of 500 nm. Figure 6.6b shows a SEM of the DC SQUID, consisting of two JJs (device JJ and reference JJ) in the superconducting loop. The device JJ has a superconducting lead length of 300 nm. Two additional gates are deposited, one covering the normal region of the reference JJ and one covering the 2DEG region around this junction (always kept at -2.5 V to deplete the 2DEG there).

6.4.2. ESTIMATION OF LOOP INDUCTANCE

In order to extract the inductance of the SQUID loop, we measure the SQUID interference pattern for different reference JJ gate voltages, $V_{\text{g,ref}}$. Figure 6.7a-l shows the obtained differential resistance maps as a function of applied current bias, I, and perpendicular magnetic field, B. Panel a-l corresponds to $V_{\text{g,ref}}$ = 0, -0.4, -0.8, -0.9, -1, -1.1, -1.2, -1.25, -1.3, -1.35, -1.4, and -1.45 V, respectively. The device JJ gate is grounded in all measurements. With the colored circles we mark the positions where the total critical current is maximum. For a given SQUID oscillation, the field at which the maximum occurs is different for positive and negative current bias: $\Delta B = B^+ - B^-$. The corresponding flux difference is given by: $\Delta\Phi = 2(L_{\text{ref}} I_{\text{c,ref}} - L_{\text{dev}} I_{\text{c,dev}})$ [28]. Here, $I_{\text{c,ref}}$ and $I_{\text{c,dev}}$ are the critical current of the reference and device junction, respectively. The inductances of the two SQUID arms are L_{ref} and L_{dev}. The above expression can be rewrit-

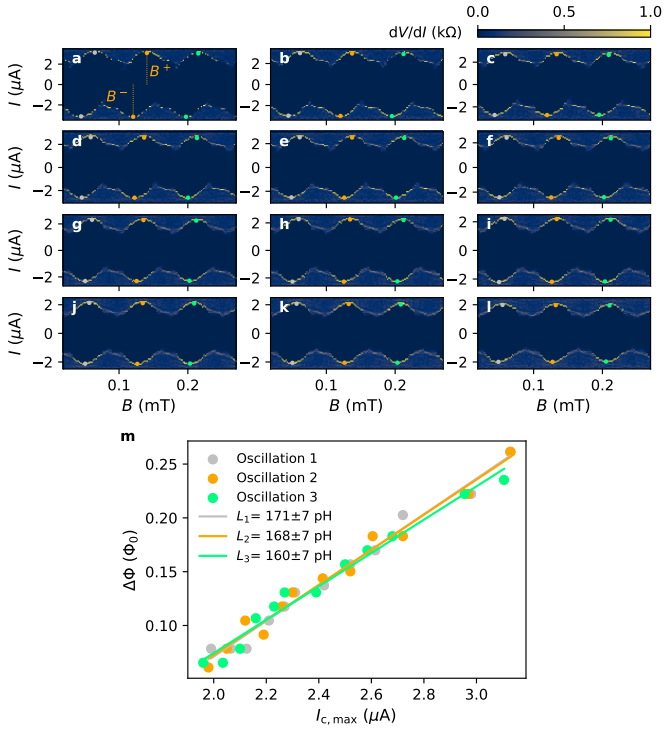

Figure 6.7: Differential resistance, $\mathrm{d}V/\mathrm{d}I$, as a function of applied current bias, I, and perpendicular magnetic field, B. Panel **a-l** corresponds to reference gate voltage $V_{\mathrm{g,ref}}$ = 0, -0.4, -0.8, -0.9, -1, -1.1, -1.2, -1.25, -1.3, -1.35, -1.4, and -1.45 V, respectively. No voltage is applied to the device junction gate. The colored circles mark the positions of maximum total critical current. **m,** $\Delta\Phi$ plotted against $I_{\mathrm{c,max}}$ for the three oscillations shown in **a-l**. The extracted ΔB is normalized with respect to the oscillation period, giving $\Delta\Phi$ in units of the magnetic flux quantum, Φ_0. The average value of the maximum critical current on the positive and negative current bias sides gives $I_{\mathrm{c,max}}$.

ten as: $\Delta\Phi = 2L_{\mathrm{ref}}I_{\mathrm{c,max}} - 2LI_{\mathrm{c,dev}}$, using the relations for the maximum critical current, $I_{\mathrm{c,max}} = I_{\mathrm{c,ref}} + I_{\mathrm{c,dev}}$, and the total loop inductance, $L = L_{\mathrm{ref}} + L_{\mathrm{dev}}$.

In Fig. 6.7m we plot the extracted $\Delta\Phi$ as a function of $I_{\mathrm{c,max}}$ for the three oscillations indicated in Fig. 6.7a-l. The linear fits yield L_{ref} = 166 pH as the average value. Since the width and the thickness of the superconducting loop is the same for all three devices, the inductance should only depend on the length of the superconducting loop. Under this assumption the loop inductance of the phase-biased JJs can be estimated to be $L_{\mathrm{ref}}l_{\mathrm{PBJJ}}/l_{\mathrm{ref}} = 321$ pH, where $l_{\mathrm{ref}} = 15.3\,\mu$m is the length of SQUID reference arm and $l_{\mathrm{PBJJ}} = 29.6\,\mu$m is the loop length of Dev 1 and 2.

6.4.3. FLUX FOCUSING IN PLANAR JJ

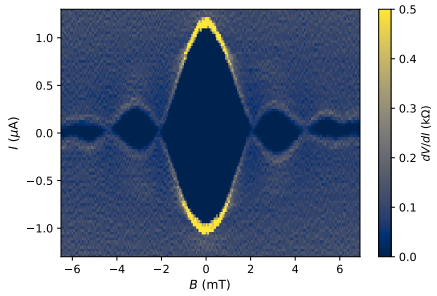

Figure 6.8: Differential resistance, $\mathrm{d}V/\mathrm{d}I$, as a function of applied current, I, and perpendicular magnetic field, B for the device JJ of the DC SQUID.

The Fraunhofer interference pattern periodicity, B_0, in a JJ is determined by the geometrical area, A, enclosed between two superconducting leads, i.e. $B_0 = \Phi_0/A$. However, in the presence of flux focusing, the periodicity is reduced from the theoretical value [24]. To estimate the effect of flux focusing we measure the differential resistance, $\mathrm{d}V/\mathrm{d}I$, as a function of applied current, I, and perpendicular magnetic field, B, for the device JJ of the DC SQUID (see Fig. 6.8). For this measurement, the reference JJ is pinched off by applying a voltage of $-2.5\,\mathrm{V}$ to the top gate. We observe the first node at $2.1\,\mathrm{mT}$ instead of the expected Fraunhofer periodicity of $B_0 = 8.6\,\mathrm{mT}$. This gives a dimensionless flux focusing factor, f, of 4.1 for this junction.

To explain our spectroscopy maps measured at the top and bottom ends of Dev 1 and Dev 2 we introduce a toy model with flux focusing in Sec. 6.4.6. Although the above extracted f gives an estimate of the focusing factor, the exact value can vary from junction to junction. The best agreement between the experimental spectroscopy maps and the toy model is be achieved with $f = 6.2$ for Dev 1 and 7.2 for Dev 2 (see Fig. 3 in the main text as well as Fig. 6.9]. The larger f values (and therefore stronger flux focusing) are in fact expected due to the shorter JJ length and larger lead length of Dev 1 and Dev 2 compared to the values for the device JJ of the DC SQUID [24].

6.4.4. JOSEPHSON PENETRATION DEPTH

The Josephson penetration depth for a JJ with the thickness of the superconducting electrodes comparable or smaller than the penetration depth is dominated by the kinetic inductance contribution and is given as [29]: $\lambda_J = (\Phi_0 w/4\pi\mu_0 J_c \lambda^2)^{1/2}$, where $w = 5\,\mu\mathrm{m}$ is the junction width, J_c is the critical current density, and λ is the superconducting penetration depth of Al.

For our junctions, the thickness of the Al electrodes (7 nm) is much smaller compared to the previously reported value of $\lambda = 180$ nm for a similar heterostructure [24]. There-

fore we use the above expression to determine λ_J. Since the critical current cannot be measured for Dev 1 and Dev 2, we estimate it based on values obtained for the DC SQUID. The critical current of the device JJ with width $w = 2\,\mu$m is $I_c = 1.05\,\mu$A (see Fig. 6.8) and the thickness of 2DEG is $t = 30$ nm. Using these values we get $J_c = I_c/wt = 1.75\times10^7$A/m^2 and $\lambda_J = 34\,\mu$m, which is much larger than the width of the JJs ($w = 5\,\mu$m). This ensures that the gauge-invariant phase difference can be expressed as $\varphi(y) = \phi + \phi'$, with $\phi' = -2\pi\frac{fBly}{\Phi_0}$.

6.4.5. TUNNELING SPECTROSCOPY FOR DEV 2

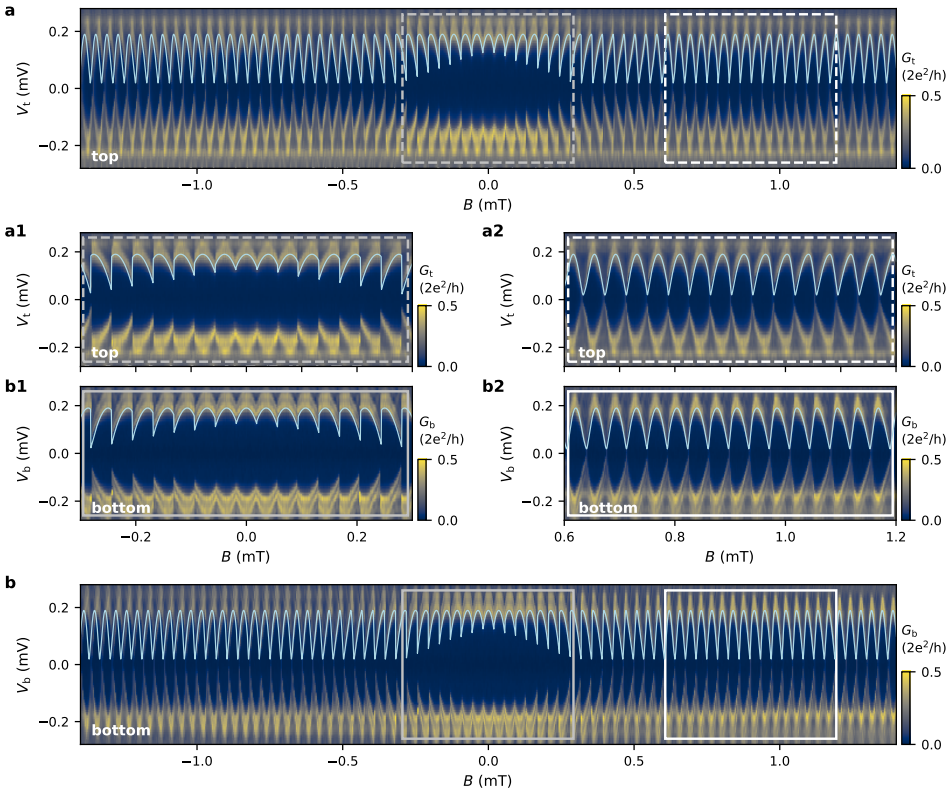

Figure 6.9: **a,** Spectroscopy map at the top end of Dev 2 with zoom-ins presented in **a1** and **a2**. The bottom spectroscopy map is shown in **b** with zoom-ins in **b1** and **b2**. Both measurements were obtained with $V_{g1} = -1.60$ V, $V_{g2} = -1.42$ V, $V_{g3} = -2.10$ V, $V_{g4} = -1.43$ V. The model (light blue line) assumes coupling to a single ABS ($\tau = 0.99$), taking into account the local phase difference in the JJ and the loop inductance ($L = 321$ pH) for the field-phase conversion.

6.4.6. TOY MODEL

This model is used to calculate the Andreev bound states (ABSs) energies of a Josephson junction embedded in a superconducting loop in the presence of a perpendicular magnetic field, as used to substantiate the measurement results shown in Fig. 3 and Fig. S5. The junction has a length l (the distance between the superconducting contacts) and a width w (the distance between the edges of the junction where the tunneling probes are connected).

We assume a homogeneous density of the supercurrent in the junction and that the current is carried by M ABSs uniformly distributed across the junction at positions $y_n = -w/2 + (n-1)\cdot w/(M-1)$ with integer $n \in [1, M]$.

The positive energies of the ABSs in the junction with the transmission coefficient τ are given by [2]:

$$E_n(\varphi_n) = \Delta\sqrt{1 - \tau\sin^2(\frac{\varphi_n}{2})}, \tag{6.3}$$

where, in the presence of the external perpendicular magnetic field, $\varphi_n = \phi + \frac{2\pi}{\Phi_0}\int_{(0,y_n)}^{(l,y_n)}\mathbf{A}\cdot d\mathbf{l}$ is the gauge-invariant phase drop across the junction for an ABS located at position y_n. ϕ is the superconducting phase difference. For the vector potential in the Landau gauge $\mathbf{A} = (-yB, 0, 0)$, the phase drop in the junction at y_n is $\varphi_n = \phi - (2\pi/\Phi_0)\cdot fBly_n$, where we included f as the magnetic field focusing factor. The latter equation gives the phase evolution of the ABS located at the edges of the junction as $\varphi_{t/b} = \phi \mp (\pi/\Phi_0)\cdot fBlw$ [30] with a minus (plus) sign for the upper (bottom) edge.

The zero-temperature supercurrent obtained from the positive-energy ABSs in the junction is given by:

$$I(\varphi) = \frac{e\Delta^2\tau}{2\hbar}\sum_n^M \frac{\sin(\varphi_n)}{E_n(\varphi_n)}. \tag{6.4}$$

In the experimental setup, the superconducting phase difference ϕ is induced by a flux $\Phi = B\pi R^2$ that threads a superconducting loop with radius R. The non-zero loop inductance L results in the following phase-flux relation [20]:

$$\phi = \frac{2\pi}{\Phi_0}(\Phi - LI(\varphi)). \tag{6.5}$$

We obtain the energies of the ABSs located at the edges of the junction versus B using the following procedure. In the first step, we solve Eq. 6.5 for a given B and obtain the ϕ value that minimizes the total energy of the system $E(\phi) = LI^2(\varphi)/2 - \sum_n^M E_n(\varphi_n)$ calculated as the sum of the energy contained in the superconducting loop and the free energy of the junction ($F = const - E_j = const - \sum E_n$). An example of a flux-to-phase conversion curve is shown in Fig. 6.10. Finally, we use the phase difference value to calculate E_n corresponding to the ABSs located at the outermost edges of the junction using Eq. 6.3.

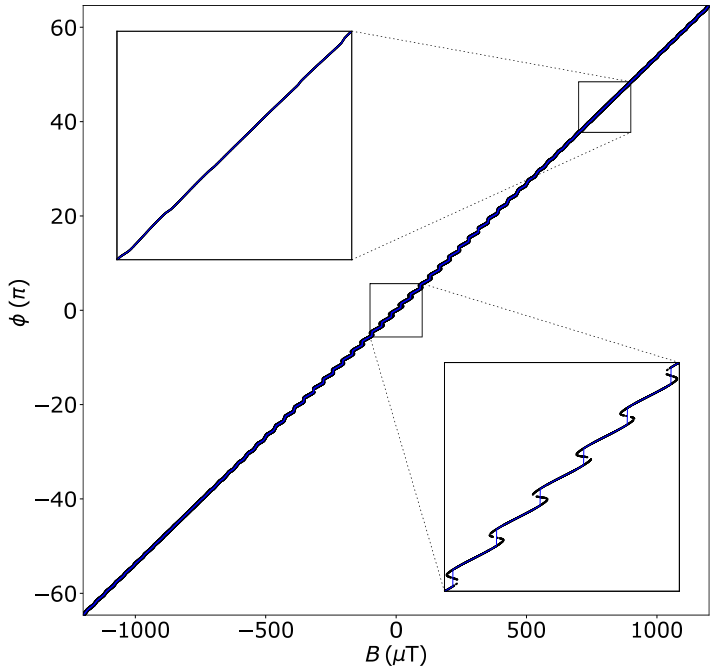

Figure 6.10: Superconducting phase difference versus applied magnetic field obtained for $L = 321$ pH, $l = 80$ nm, $w = 5000$ nm, $M = 35$, $\tau = 0.99$, $R = 4207$ nm, $\Delta = 0.2$ meV and $f = 6.2$. The black dots show possible phase values for a given B, while the blue curve shows the superconducting phase difference obtained by minimizing the total energy.

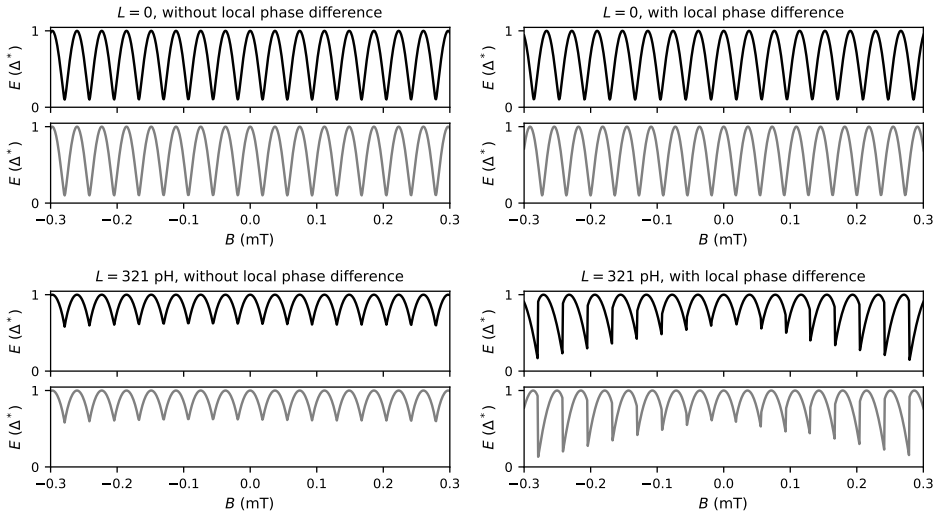

Figure 6.11: ABS energy versus magnetic field in the presence or absence of the loop inductance and local phase difference in the JJ as indicated. The top and bottom panels correspond to an ABS located at the top and bottom end of the JJ, respectively. For all plots, the following parameters are used: $l = 80$ nm, $w = 5000$ nm, $M = 35$, $\tau = 0.99$, $R = 4207$ nm, $\Delta = 0.2$ meV and $f = 6.2$.

Figure 6.11 shows an ABS located at the top (top panel) and bottom (bottom panel) end of the JJ in the presence and absence of the loop inductance and the local phase difference arising from the magnetic vector potential as indicated. The reversal of the skewness can only happen when both the loop inductance and the local phase difference are present.

Table 6.1 summarizes the parameters that are used for the overlays for Dev 1 (Fig. 3 of the main text) and Dev 2 (Fig. 6.9).

Parameter	Dev 1	Dev 2
l (nm)	80	80
w (μm)	5	5
R (nm)	4207	4190
L (pH)	321	321
Δ (meV)	0.2	0.19
f	6.2	7.2
M	35	45
τ	0.99	0.99

Table 6.1: Toy model parameters used for Dev 1 and Dev 2.

6.4.7. MICROSCOPIC MODEL

TUNNELING SPECTROSCOPY CALCULATIONS

We consider a four-terminal device, with two vertical superconducting leads separated by the normal region (which creates the superconductor-normal-superconductor junction) and two normal leads that are placed horizontally at the top and bottom as shown in Fig. 6.12. Between the horizontal leads and the normal scattering region, we introduce tunneling barriers that mimic the behavior of QPCs tuned into the tunneling regime.

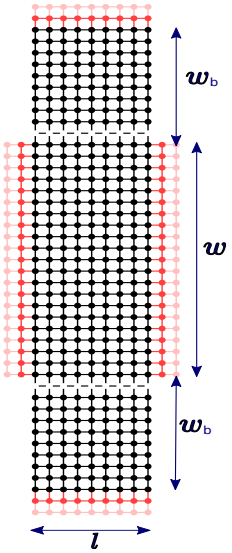

Figure 6.12: Schematic of the system considered for tunneling spectroscopy calculations. The dots denote the sites of the computational mesh. The black dots correspond to the scattering region, whereas the pink ones denote the semi-infinite leads. We use $l = 80$ nm (the distance between the superconducting contacts) and $w = 5000$ nm (the distance between the edges of the junction where the tunneling probes are connected). The barrier potential at the top and bottom is separated from the normal leads of width $w_b = 100$ nm. The vertical leads are superconducting, while the horizontal leads are normal.

The considered system is described by the Hamiltonian

$$\begin{bmatrix} H & \Delta \\ \Delta^* & -H \end{bmatrix}, \tag{6.6}$$

acting on a wave function in the basis $\Psi = (\Psi_e, \Psi_h)^T$. Here H is defined as

$$H = -\frac{\hbar^2}{2m^*}\nabla^2 + V(r) - \mu. \tag{6.7}$$

μ is the chemical potential, m^* is the effective electron mass and $V(r)$ is the rectangular potential barrier of height V_g placed just above and below the normal region of length

($l = 80$ nm).

In the presence of a magnetic field, the Hamiltonian H becomes

$$H^{'} = -\frac{\hbar^2}{2m^*}(\nabla - q\mathbf{A}/\hbar)^2 + V(r) - \mu, \tag{6.8}$$

with $q = -|e|$ for the electron and $q = |e|$ for the hole part of the Hamiltonian Eq. 6.6. We choose the vector potential in the Landau gauge with $\vec{B} = B\hat{z}$, so that $\vec{A} = -By\hat{x}$.

The superconducting pairing potential Δ varies spatially and is given by:

$$\Delta(x) = \begin{cases} \Delta_0 & \text{if } x < -l/2 \\ 0 & \text{if } -l/2 \leq x \leq l/2 \\ \Delta_0 e^{\iota\phi} & \text{if } x > l/2 \end{cases} \tag{6.9}$$

We discretize the Hamiltonian Eq. 6.6 on a square lattice with discretization constant $a = 10$ nm. We put the material parameters as $m^* = 0.016m_e$, $\mu = 5$ meV, $\Delta = 0.2$ meV. We introduce the anisotropic mass in the superconducting leads with the mass along the translation symmetry of the superconducting leads equal to $10m^*$ as appropriate for the description of transparent normal-superconductor interfaces in models where the chemical potential is kept constant [31]. Including a vector potential in this system is done using Peierls substitution as $t_{nm} \rightarrow t_{nm}\exp[\frac{-\iota e}{\hbar}\int \mathbf{A}d\mathbf{l}]$ [32, 33].

We exclude the magnetic field from the superconducting leads to account for the screening effect setting $\mathbf{A} = 0$ there. We also put zero vector potential in the top and bottom leads to maintain the translation invariance. This in turn introduces a delta peak in the magnetic field where the horizontal leads are attached (as calculated from $\mathbf{B} = \nabla \times \mathbf{A}$). We have, however, verified that for the considered small magnetic fields, this does not affect our results, as confirmed by replacing the vector potential by a position-dependent superconducting phase as $\phi \rightarrow \phi - \frac{2\pi Bly}{\Phi_0}$ and observing that both results match accurately.

The finite mean free path (l_e) is implemented by introducing a random on-site disorder potential $V_d(x, y)$ with the amplitude uniformly distributed between $-U_d/2$ and $U_d/2$ [34], where

$$U_d = \mu\sqrt{\frac{6\lambda_F^3}{\pi^3 a^2 l_e}}. \tag{6.10}$$

Here a, l_e, λ_F are the lattice constant, mean free path and the Fermi wavelength, respectively.

We calculate the conductance map with respect to the phase difference ϕ and energy using the scattering matrix approach implemented in the Kwant package [35], using the formula:

$$G_{t/b} = \frac{2e^2}{h}(N^e_{t/b} - T^{ee}_{t/b} + T^{he}_{t/b}), \tag{6.11}$$

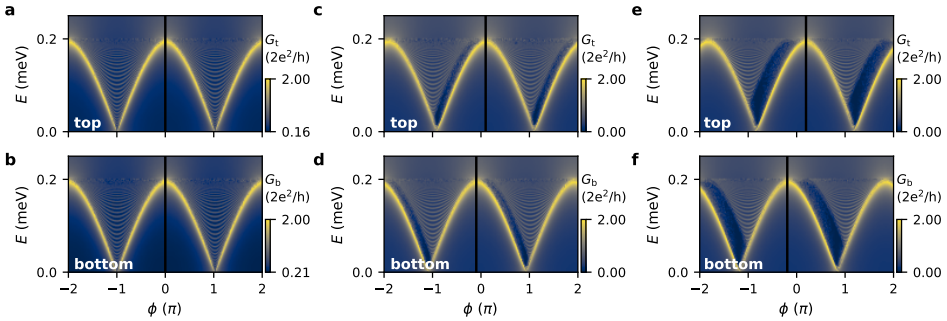

Figure 6.13: Conductance versus phase difference and energy calculated for quasiparticles injected from the top lead (upper row) and bottom lead (lower row) at $B = 0$ (**a**-**b**), $B = 0.5$ mT (**c**-**d**) and $B = 1$ mT (**e**-**f**). The vertical black lines denote the expected phase shift of the edge modes due to the magnetic field $\varphi_{t/b} = \phi \mp (\pi/\Phi_0) \cdot fBlw$.

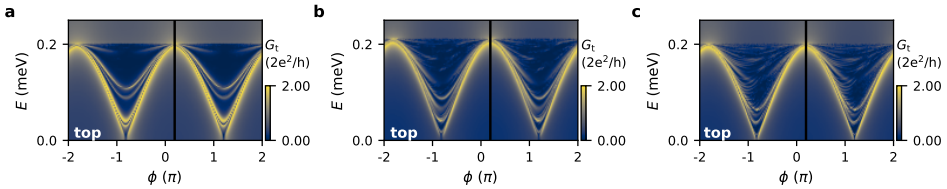

Figure 6.14: Conductance versus phase difference and energy calculated for quasiparticles injected from the top lead for $B = 1$ mT and different mean free paths $l_e = 150$ (**a**), 500 (**b**) and 1000 nm (**c**).

where t and b stand for top and bottom lead respectively and $N^e_{t/b}$ is the corresponding number of the electron modes. The energy dependent transmissions are evaluated as:

$$T^{\alpha\beta}_{t/b} = Tr([S^{\alpha\beta}_{t/b}]^\dagger S^{\alpha\beta}_{t/b}), \tag{6.12}$$

where $S^{\alpha\beta}_{t/b}$ is the block of scattering amplitudes of incident particle of type β in t (b) lead to a particle of type α in the lead t (b).

ABS CALCULATION

For the numerical calculation of ABSs spectra we consider a Josephson junction treated as a finite system consisting of a normal scattering region and two long superconducting segments. The two superconducting regions have a length of $l_{SC} = 2000$ nm (much larger than the coherence length $\xi = 1091.16$ nm, calculated using the formula, $\xi = \frac{\hbar v_F}{\Delta}$ where $v_F = \sqrt{2\mu/m^*}$), and they are separated by a normal region of length $l = 80$ nm. The width w of the entire system is taken as 1000 nm. The Hamiltonian remains the same as in equation 6.8 except for the tunneling barrier potentials (here we do not consider the

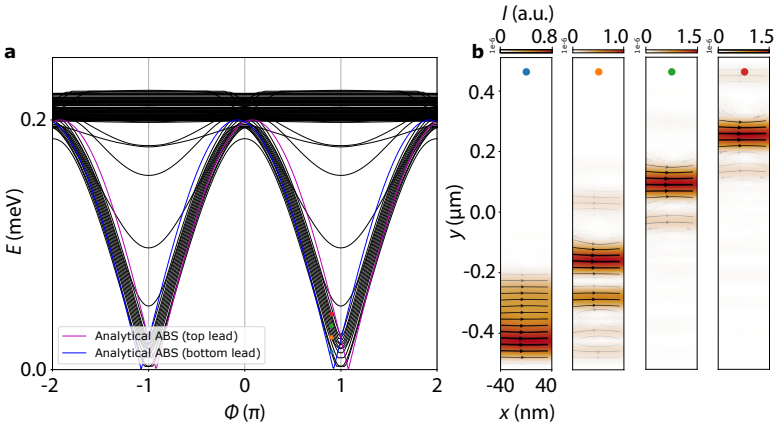

Figure 6.15: **a,** ABS spectrum of a SNS junction with two SC regions ($l_{SC} = 2000$ nm) separated by a normal region ($l = 80$ nm, $w = 1000$ nm) at $B = 2$ mT without disorder. The color curves denote analytically calculated ABS from Eq. 6.3 with $\tau = 1$. **b,** Supercurrent in the normal area of the junction calculated for the ABS whose energies are denoted by the color circles in **a**.

top and bottom electrode). The anisotropic mass and Peierls phase factor (for magnetic vector potential) are introduced as described above. We diagonalize the Hamiltonian and plot the energy with respect to the phase difference ϕ, and also the probability current in Fig. 6.15. In the probability current, we observe that in the presence of the perpendicular field each ABSs is localized in a separated region in the junction. The different spatial position of the ABSs is reflected by their different phase shifts in the spectrum plotted in Fig. 6.15 (a).

REFERENCES

1. Kulik, I. O. Macroscopic Quantization and the Proximity Effect in S-N-S Junctions. *Zh. Eksp. Teor. Fiz.* **57** (1969).
2. Beenakker, C. W. J. Universal limit of critical-current fluctuations in mesoscopic Josephson junctions. *Phys. Rev. Lett.* **67,** 3836–3839 (1991).
3. Wendin, G. & Shumeiko, V. S. Josephson transport in complex mesoscopic structures. *Superlattices Microstruct.* **20,** 569–573 (1996).
4. Su, Z., Tacla, A. B., Hocevar, M., Car, D., Plissard, S. R., Bakkers, E. P., Daley, A. J., Pekker, D. & Frolov, S. M. Andreev molecules in semiconductor nanowire double quantum dots. *Nat. Commun.* **8,** 1–6 (2017).
5. Pillet, J.-D., Benzoni, V., Griesmar, J., Smirr, J.-L. & Girit, Ç. Ö. Nonlocal Josephson effect in Andreev molecules. *Nano Lett.* **19,** 7138–7143 (2019).
6. Kürtössy, O., Scherübl, Z., Fülöp, G., Lukács, I. E., Kanne, T., Nygård, J., Makk, P. & Csonka, S. Andreev molecule in parallel InAs nanowires. *Nano Lett.* **21,** 7929–7937 (2021).
7. Jünger, C., Lehmann, S., Dick, K. A., Thelander, C., Schönenberger, C. & Baumgartner, A. Intermediate states in Andreev bound state fusion. `https://arxiv.org/abs/2111.00651` (2021).
8. Hays, M., de Lange, G., Serniak, K., van Woerkom, D. J., Bouman, D., Krogstrup, P., Nygård, J., Geresdi, A. & Devoret, M. H. Direct Microwave Measurement of Andreev-Bound-State Dynamics in a Semiconductor-Nanowire Josephson Junction. *Phys. Rev. Lett.* **121,** 047001 (2018).
9. Hays, M., Fatemi, V., Bouman, D., Cerrillo, J., Diamond, S., Serniak, K., Connolly, T., Krogstrup, P., Nygård, J., Yeyati, A. L., Geresdi, A. & Devoret, M. H. Coherent manipulation of an Andreev spin qubit. *Science* **373,** 430–433 (2021).
10. Tinkham, M. *Introduction to Superconductivity* 2nd ed. (Dover Publications, 1996).
11. Cuevas, J. C. & Bergeret, F. S. Magnetic Interference Patterns and Vortices in Diffusive SNS Junctions. *Phys. Rev. Lett.* **99,** 217002 (2007).
12. Kaperek, K., Heun, S., Carrega, M., Wójcik, P. & Nowak, M. P. Theory of scanning gate microscopy imaging of the supercurrent distribution in a planar Josephson junction. *Phys. Rev. B* **106,** 035432 (2022).
13. Hell, M., Leijnse, M. & Flensberg, K. Two-Dimensional Platform for Networks of Majorana Bound States. *Phys. Rev. Lett.* **118,** 107701 (2017).
14. Pientka, F., Keselman, A., Berg, E., Yacoby, A., Stern, A. & Halperin, B. I. Topological Superconductivity in a Planar Josephson Junction. *Phys. Rev. X* **7,** 021032 (2017).

15. Ren, H., Pientka, F., Hart, S., Pierce, A. T., Kosowsky, M., Lunczer, L., Schlereth, R., Scharf, B., Hankiewicz, E. M., Molenkamp, L. W., Halperin, B. I. & Yacoby, A. Topological superconductivity in a phase-controlled Josephson junction. *Nature* **569,** 93–98 (2019).

16. Fornieri, A., Whiticar, A. M., Setiawan, F., Portolés, E., Drachmann, A. C. C., Keselman, A., Gronin, S., Thomas, C., Wang, T., Kallaher, R., Gardner, G. C., Berg, E., Manfra, M. J., Stern, A., Marcus, C. M. & Nichele, F. Evidence of topological superconductivity in planar Josephson junctions. *Nature* **569,** 89–92 (2019).

17. Stern, A. & Berg, E. Fractional Josephson Vortices and Braiding of Majorana Zero Modes in Planar Superconductor-Semiconductor Heterostructures. *Phys. Rev. Lett.* **122,** 107701 (2019).

18. Le Sueur, H., Joyez, P., Pothier, H., Urbina, C. & Esteve, D. Phase Controlled Superconducting Proximity Effect Probed by Tunneling Spectroscopy. *Phys. Rev. Lett.* **100,** 197002 (2008).

19. Roditchev, D., Brun, C., Serrier-Garcia, L., Cuevas, J. C., Bessa, V. H. L., Milošević, M. V., Debontridder, F., Stolyarov, V. & Cren, T. Direct observation of Josephson vortex cores. *Nat. Phys.* **11,** 332–337 (2015).

20. Banerjee, A., Lesser, O., Rahman, M. A., Wang, H. .-., Li, M. .-., Kringhøj, A., Whiticar, A. M., Drachmann, A. C. C., Thomas, C., Wang, T., Manfra, M. J., Berg, E., Oreg, Y., Stern, A. & Marcus, C. M. Signatures of a topological phase transition in a planar Josephson junction. `https://arxiv.org/abs/2201.03453` (2022).

21. Banerjee, A., Lesser, O., Rahman, M. A., Thomas, C., Wang, T., Manfra, M. J., Berg, E., Oreg, Y., Stern, A. & Marcus, C. M. Local and Nonlocal Transport Spectroscopy in Planar Josephson Junctions. `https://arxiv.org/abs/2205.09419` (2022).

22. Moehle, C. M., Ke, C. T., Wang, Q., Thomas, C., Xiao, D., Karwal, S., Lodari, M., van de Kerkhof, V., Termaat, R., Gardner, G. C., Scappucci, G., Manfra, M. J. & Goswami, S. InSbAs Two-Dimensional Electron Gases as a Platform for Topological Superconductivity. *Nano Letters* **21,** 9990–9996 (2021).

23. Newrock, R., Lobb, C., Geigenmuller, U. & Octavio, M. The two-dimensional physics of Josephson junction arrays. *Solid State Physics* **54,** 263–512 (2000).

24. Suominen, H. J., Danon, J., Kjaergaard, M., Flensberg, K., Shabani, J., Palmstrøm, C. J., Nichele, F. & Marcus, C. M. Anomalous Fraunhofer interference in epitaxial superconductor-semiconductor Josephson junctions. *Phys. Rev. B* **95,** 035307 (2017).

25. Nichele, F., Portolés, E., Fornieri, A., Whiticar, A. M., Drachmann, A. C. C., Gronin, S., Wang, T., Gardner, G. C., Thomas, C., Hatke, A. T., Manfra, M. J. & Marcus, C. M. Relating Andreev Bound States and Supercurrents in Hybrid Josephson Junctions. *Phys. Rev. Lett.* **124,** 226801 (2020).

26. Banerjee, A., Geier, M., Rahman, M. A., Sanchez, D. S., Thomas, C., Wang, T., Manfra, M. J., Flensberg, K. & Marcus, C. M. Control of Andreev bound states using superconducting phase texture. `https://arxiv.org/abs/2205.15690` (2022).

27. Laeven, T., Nijholt, B., Wimmer, M. & Akhmerov, A. R. Enhanced Proximity Effect in Zigzag-Shaped Majorana Josephson Junctions. *Phys. Rev. Lett.* **125,** 086802 (2020).

28. Braginski, A. I. & Clarke, J. *The SQUID Handbook* (John Wiley and Sons, Ltd, 2004).

29. Tolpygo, S. K. & Gurvitch, M. Critical currents and Josephson penetration depth in planar thin-film high-Tc Josephson junctions. *Applied Physics Letters* **69,** 3914–3916 (1996).

30. Sticlet, D., Wójcik, P. & Nowak, M. P. SQUID pattern disruption in transition metal dichalcogenide Josephson junctions due to nonparabolic dispersion of the edge states. *Phys. Rev. B* **102,** 165407 (2020).

31. Sticlet, D., Nijholt, B. & Akhmerov, A. Robustness of Majorana bound states in the short-junction limit. *Phys. Rev. B* **95,** 115421 (2017).

32. Peierls, R. Zur Theorie des Diamagnetismus von Leitungselektronen. *Zeitschrift für Physik* **80** (1933).

33. Hofstadter, D. R. Energy levels and wave functions of Bloch electrons in rational and irrational magnetic fields. *Phys. Rev. B* **14,** 2239–2249 (1976).

34. Ando, T. Quantum point contacts in magnetic fields. *Phys. Rev. B* **44,** 8017–8027 (1991).

35. Groth, C. W., Wimmer, M., Akhmerov, A. R. & Waintal, X. Kwant: a software package for quantum transport. *New J. Phys.* **16,** 063065 (2014).

7

LOCAL AND NONLOCAL CONDUCTANCE MEASUREMENTS IN PLANAR, PHASE-BIASED JOSEPHSON JUNCTIONS

A topological phase in a one-dimensional semiconductor-superconductor hybrid is characterized by a zero-energy state at each end of the system as well as a gapped bulk. While many experiments have observed zero-bias peaks in tunneling spectroscopy measurements performed at one end of the sytem, a more reliable judgment about the realization of a topological phase can be made by simultaneously probing the ends and the bulk of the hybrid. In this chapter, we combine local tunneling spectroscopy at the two ends of planar, phase biased Josephson junctions (JJs) with nonlocal conductance measurements, which give information about the bulk of the system. We investigate the conductances as a function of superconducting phase difference across the JJ and for different Zeeman fields. At finite Zeeman fields, we observe zero-bias peaks in local spectroscopy, but do not find clear evidence of a re-opened bulk gap.

7.1. INTRODUCTION

Semiconductor-superconductor hybrids have attracted a lot of attention, among others for creating Majorana zero modes (MZMs) at the ends of a one-dimensional structure [1, 2]. These end modes have been probed most commonly by tunneling spectroscopy, and the characteristic zero-bias conductance peak (ZBP) was observed in many experiments [3–5]. However, alternative mechanisms such as disorder or a smooth potential at the ends of the structure can also cause zero-energy states mimicking the MZMs [6, 7]. This makes tunneling spectroscopy measurements hard to interpret, especially when conducted only at one end.

The nonlocal conductance in a three-terminal device was suggested as an alternative and by itself more reliable detection method for a topological phase transition [8], sparking additional theoretical investigations [9–12]. While tunneling spectroscopy is sensitive to the edge of the hybrid system, the nonlocal conductance probes the bulk, with an expected closure and reopening of the induced superconducting gap when the external magnetic field is swept across the topological phase transition. Besides, nonlocal conductance measurements can be combined with local tunneling spectroscopy at both ends, improving the reliability of the identification of a topological phase further [13]. So far, the full conductance matrix was measured on hybrid nanowire devices with no clear evidence of a gap reopening in the nonlocal signals [14–16].

Here, we use local and nonlocal conductance measurements in planar Josephson junctions (JJs), which can be used to create phase-tunable MZMs [17, 18]. When the phase difference between the two superconducting leads is tuned to π, the topological regime may be reached at a low in-plane magnetic field. These devices were previously studied by means of one-ended [19, 20] or two-ended [21] local spectroscopy. At zero in-plane magnetic field, we observe Andreev bound states in local spectroscopy and phase-dependent nonlocal signals. As the magnetic field is increased, ZBPs emerge in local spectroscopy (mostly at one end), but no gap reopening occurs in the nonlocal signals. These results show how nonlocal conductance measurements can complement traditional tunneling spectroscopy in order to differentiate between trivial and topological regimes.

7.2. BACKGROUND ABOUT NONLOCAL CONDUCTANCE

The nonlocal conductance was originally proposed in [8] as a reliable probe for a topological phase transition in a semiconductor-superconductor hybrid system. Figure 7.1a shows a schematic of the considered device, where a central semiconducting region is contacted by two normal metals (N_1, N_2) and a grounded superconductor (S). The superconductor induces a gap, Δ^*, in the semiconductor due to the proximity effect.

Different transport processes occur depending on the voltage bias applied to one of the normal leads (the other one is grounded). This is illustrated in the bottom panel of Fig. 7.1a when N_1 is energized. At $|E| < \Delta^*$, the quasiparticles propagate as evanescent waves

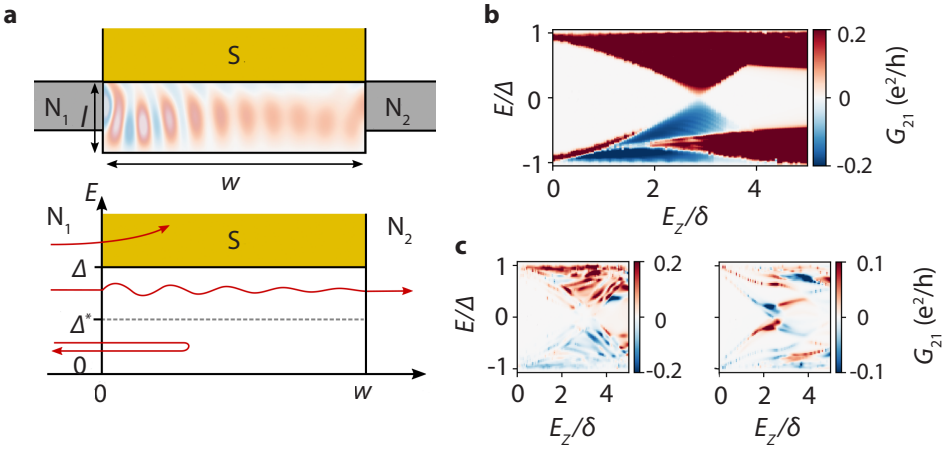

Figure 7.1: **a,** Schematic of the three-terminal hybrid device with two normal leads (N_1, N_2) and a grounded superconducting contact (S). The bottom panel illustrates the allowed transport processes depending on the voltage bias applied to N_1. **b,** Numerical calculation of the nonlocal conductance in the single-mode regime as a function of energy and applied magnetic field parallel to the S-N interface for a ballistic device with $l = 100\,\text{nm}$ and $w = 10\xi$ (see [8] for other parameters). The bulk induced gap closes and reopens when sweeping the magnetic field across the topological phase transition. **c,** Nonlocal conductance for a quasi-ballistic system with mean free path $l_e = 0.2w$ in the left panel ($l = 100\,\text{nm}$, $w = 8\xi$), and for a diffusive system in the right panel ($l = 100\,\text{nm}$, $w = 5\xi$, $l_e = 0.2w$, $l_e = 0.2l$). For the quasi-ballistic and diffusive system, the reopened gap vanishes for $l = 200\,\text{nm}$ (not shown here). The figures are adapted from [8].

7

through the central region with the induced coherence length, ξ, as the decay length. This leads to a suppression of the nonlocal conductance, $G_{21} = \mathrm{d}I_2/\mathrm{d}V_1$, with increasing width of the semiconductor, w. When the energy exceeds the bulk superconducting gap, the superconductor increasingly absorbs quasiparticles as w is expanded, and goes to zero for $w >> \xi$. Provided that the two normal contacts are sufficiently decoupled ($w \geq \xi$), transport is only possible in the energy window $\Delta^* < |E| < \Delta$. Here, two processes can constitute the nonlocal conductance: direct electron transfer of an electron from N_1 to N_2 (giving rise to a positive G_{21}), and transmission of an electron from N_1 to a hole in N_2 (leading to a negative G_{21}). All in all, this demonstrates that the nonlocal conductance is sensitive to three global properties of the system: the induced coherence length, the induced superconducting gap and the gap of the parent superconductor, which also remains valid when accounting for disorder (normal scattering) in the semiconductor.

Figure 7.1b shows a numerical calculation of the nonlocal conductance for a ballistic device with $l = 100\,\text{nm}$ when a magnetic field is applied parallel to the S-N interface to drive the system in the topological regime. In the vicinity of the topological phase tran-

sition, the bulk induced gap closes and reopens, and G_{21} is an odd function of bias close to $E = 0$. These features can also be observed in the quasi-ballistic and diffusive system (left and right panel of Fig. 7.1c, respectively), although the reopened gap is less prominent and vanishes when l is increased (the latter is not shown here).

7.3. METHODS

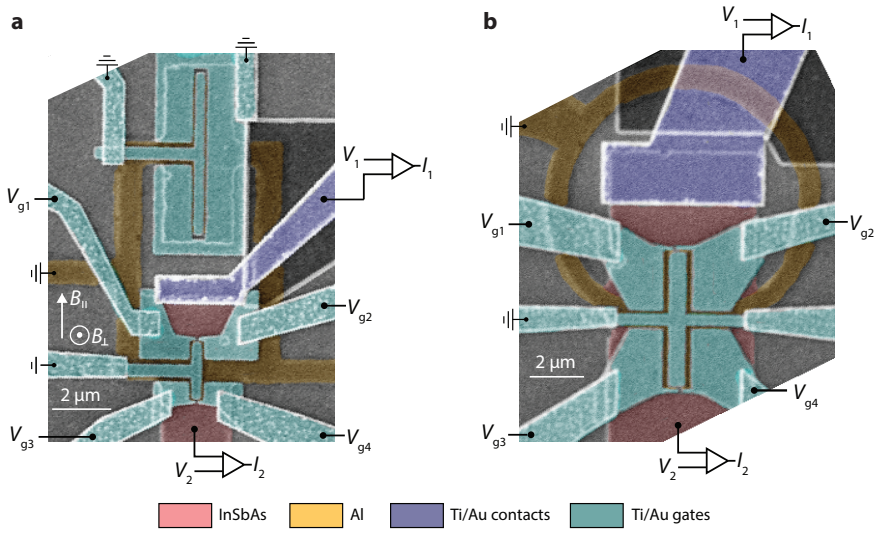

Figure 7.2: **a,** SEM of the DC SQUID. The device JJ, studied by the local and nonlocal conductance measurements, is situated on the bottom. The reference JJ is on the top. **b,** SEM of the phase-biased JJ. The circuits used for the three-terminal measurements are indicated.

We will investigate the local and nonlocal conductance in devices with two superconducting leads attached to the semiconducting region forming a JJ. Also, we embed the JJs in a superconducting loop, allowing to phase-bias them. We fabricate a DC SQUID (consisting of two JJs in the loop) and a phase-biased JJ (single JJ in the loop) using an InSbAs/Al hybrid two-dimensional electron gas (2DEG) [22] (see chapter 6 for fabrication details). A false-colored scanning electron micrograph (SEM) of both devices is shown in Fig. 7.2. The device JJ of the SQUID, which will be studied by the conductance measurements (bottom JJ in Fig. 7.2a), has a length (separation between the superconducting contacts) of $l = 120\,\text{nm}$ and a width of $w = 2\,\mu\text{m}$. The reference JJ (top JJ) has a length of 80 nm and a width of $5\,\mu\text{m}$. The phase-biased JJ (Fig. 7.2b) has dimensions $l = 80\,\text{nm}$ and $w = 5\,\mu\text{m}$.

Tuning the phase difference between the superconducting leads, φ, is achieved by applying a perpendicular magnetic field, $B_\perp$, that passes through the superconducting loop.

For the SQUID, there is also a phase drop across the reference JJ since its switching current is not much larger than the one for the device JJ (ratio 2:1, see Fig. 7.7 in the supplementary information (SI)). This complication is absent for the phase-biased JJ.

In order to perform local tunneling spectroscopy and measure the nonlocal conductances, we energize the splitgates that are deposited on the two ends of the JJ (for the SQUID on the device JJ) and apply voltages V_1 (V_2) to the top (bottom) normal lead while measuring the currents I_1 and I_2. To obtain the local conductance $G_{11} = \mathrm{d}I_1/\mathrm{d}V_1$ and the nonlocal conductance $G_{21} = \mathrm{d}I_2/\mathrm{d}V_1$ at a fixed $B_\perp$, we vary V_1 while measuring I_1 and I_2, keeping $V_2 = 0$. Then, to get the nonlocal conductance G_{12} and and the local conductance G_{22}, we vary V_2 and measure I_1 and I_2, setting $V_1 = 0$. This is repeated for all perpendicular magnetic fields. The superconducting loop is grounded at all times. After the measurements, circuit artifacts are corrected according to [23]. We will study the local and nonlocal conductances at different in-plane magnetic fields (Zeeman fields), $B_\parallel$. In the main text, we focus on results on the DC SQUID, and show data on the phase-biased JJ in the SI.

7.4. ZERO ZEEMAN FIELD RESULTS

In Fig. 7.3 we present local and nonlocal conductance measurements at $B_\parallel = 0$. Focusing on local spectroscopy (G_{11} and G_{22}) first, we see a phase-dependent modulation of the superconducting gap, indicating Andreev bound states (ABSs) in the JJ. For $B_\perp > 0.4\,\mathrm{mT}$, the oscillations become skewed - in opposite directions for top and bottom spectroscopy. This is also observed for the phase-biased JJ, and explained in detail in chapter 6. In brief, it results from the fact that the top and bottom splitgates probe different ABSs localized close to the respective gates, and that the phase difference on the two sides of the JJ is different due to the perpendicular magnetic field in the junction. The visibility of this effect is enhanced by the loop inductance, which also causes phase slips at $\varphi \sim \pi$, preventing the ABS levels to touch at zero energy.

Turning to the nonlocal conductances (G_{12} and G_{21}), we see that they are negligibly small at low energies and when $|eV|$ exceeds the size of the bulk superconducting gap ($\Delta \approx 220\,\mu\mathrm{eV}$). As discussed in section 7.2, in the first case, the injected quasiparticles travel as evanescent waves in the normal region of the JJ, and transport is suppressed exponentially with distance. In the second case, the quasiparticles are directly absorbed by the superconductor. A finite nonlocal conductance emerges when $|eV|$ matches the ABS energies. The signals are antisymmetric in bias, consistent with the numerical simulations including disorder (see Fig. 7.1c) and with the nanowire experiments [14–16]. The fact that the nonlocal conductances have a phase-dependence reinforce that they are carried across the JJ by the ABSs. It is curious that the skewness that is observed in the local signals at $B_\perp > 0.4\,\mathrm{mT}$ is not so clearly present in the nonlocal conductances. This is an indication that the nonlocal signals are indeed a measure of the entire bulk since one expects the skewness to gradually change across the JJ and thus average out. The same observation is made for the phase-biased JJ (see Fig. 7.11 in the SI). On the

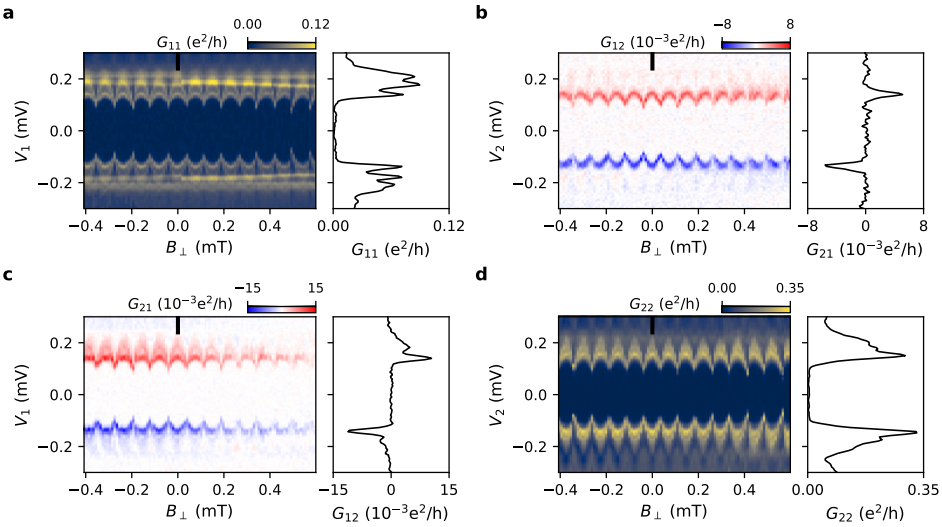

Figure 7.3: Local and nonlocal conductances at $B_\parallel = 0$. A phase-dependent modulation of the gap is visible in local spectroscopy from the top (**a**) and the bottom (**d**), indicating the presence of ABSs in the JJ. The nonlocal conductances (**b**-**c**) show a similar phase dependence (the skewness that is observed in the local conductances at $B_\perp > 0.4\,\mathrm{mT}$ is less prominent in G_{12} and G_{21}).

7

other hand, it should be pointed out that there are also differences between the two nonlocal signals, see for example the finite signal in G_{21} close to $V_1 = \pm 0.2\,\mathrm{mV}$ that is significantly smaller in G_{12}. This seems to be correlated with the additional discrete states being present (absent) in G_{11} (G_{22}). The same effect can also be seen in the phase-biased JJ, where we observe that the nonlocal gap sizes are slightly different, matching the gap size measured in local spectroscopy on the current-injecting side (see Fig. 7.11 in the SI).

7.5. FINITE ZEEMAN FIELD RESULTS

Next, we study the local and nonlocal conductances in the presence of an in-plane magnetic field. Due to a small sample tilt, the Zeeman field has a perpendicular component that we correct for by tracing the phase slips (see Fig. 7.8 in the SI). When applying the Zeeman field, a splitting of the ABS energy levels and a corresponding reduction of the gap size is expected. Figure 7.4 shows a measurement at $B_\parallel = 250\,\mathrm{mT}$, where the gap size is clearly reduced in the local and nonlocal signals. Also, more discrete levels become visible. Note that in G_{22} the lowest levels start to touch at $\varphi \sim \pi$, while in G_{11} this is not the case. This might be caused by disorder in the normal region of the JJ, resulting in spatially varying ABS transparencies. The different Zeeman field evolution of the ABSs measured by local spectroscopy on both sides becomes especially clear at $B_\parallel = 400\,\mathrm{mT}$, where the gap in G_{22} is closed in the whole phase range, while it remains open at $\varphi \sim 0$

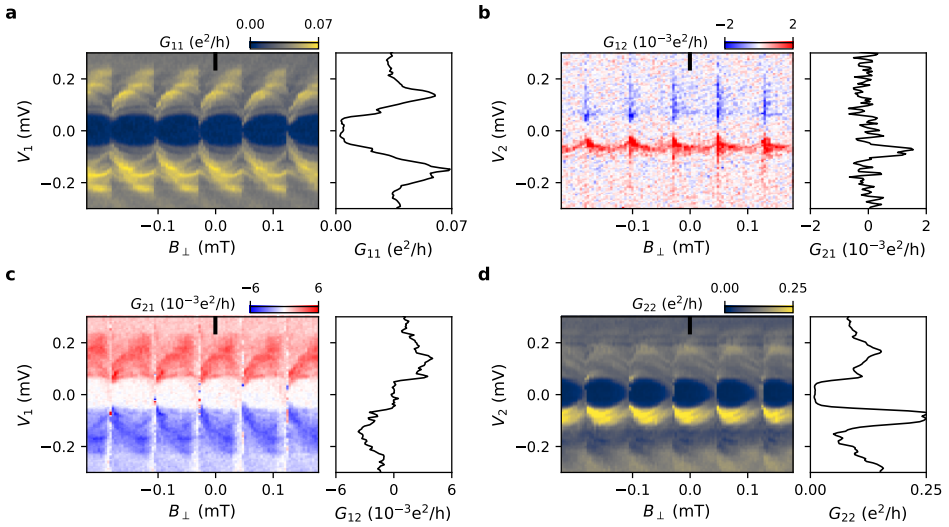

Figure 7.4: Local and nonlocal conductances at $B_\parallel = 250\,\text{mT}$. A gap reduction is visible in all four measurements, with a phase-dependent gap closure in G_{22} that is not present in G_{11}. The nonlocal signals differ in sign and for larger energies, but show a similar gap size without clear phase-dependent gap closure.

7

in G_{11} (see Fig. 7.9 in the SI). A similar phase-independent gap closure occurs in G_{11} around $B_\parallel = 550\,\text{mT}$ (bottom gap still closed), at which point the gap in the nonlocal signals also vanishes (see Fig. 7.10 in the SI).

An interesting situation arises at $B_\parallel = 650\,\text{mT}$ (see Fig. 7.5). The gap in G_{22} seems to have reopened slightly along with the emergence of a zero-energy state that is hardly phase-tunable. A similar observation can be made in G_{11}, however with a less clear separation of the zero-energy state from the next highest level. Phase-independent ZBPs were recently also seen in planar JJs based on an InAs 2DEG using two-ended local spectroscopy [21]. In the nonlocal signals there is no obvious gap visible, but a sign inversion in the phase ranges where the ZBPs occur in local spectroscopy. It would have been insightful to check the stability of these features when changing the splitgate voltages, but instead we focused on increasing the Zeeman field further.

At $B_\parallel = 700\,\text{mT}$ (see Fig. 7.6), the ZBP in G_{22} persists, while the one in G_{11} splits off from zero energy for the largest part of the phase range. Also, the sign inversion in the two nonlocal signals happens at opposing phase ranges now. The fact that the ZBP in G_{11} is not stable in Zeeman field and loses correlation to the one in G_{22} makes an interpretation in terms of a uniform topological regime across the JJ unlikely. Besides, no gap is observed in the nonlocal signals, only sign inversions that also lose correlation with each other.

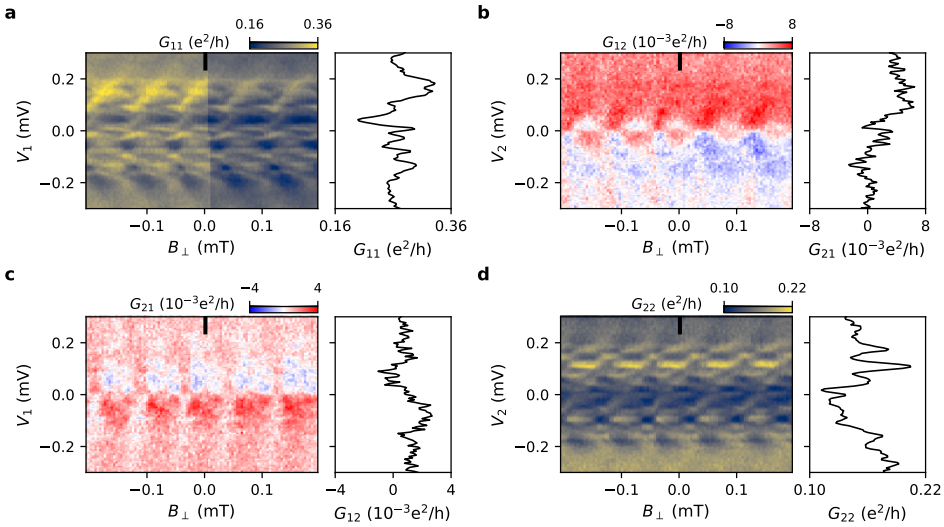

Figure 7.5: Local and nonlocal conductances at $B_\parallel = 650\,\mathrm{mT}$. A weak ZBP (hardly phase-tunable) emerges in G_{11} and G_{22}. No gap is visible in the nonlocal conductances, but sign inversions that happen at the phase ranges where the ZBPs occur in local spectrocopy.

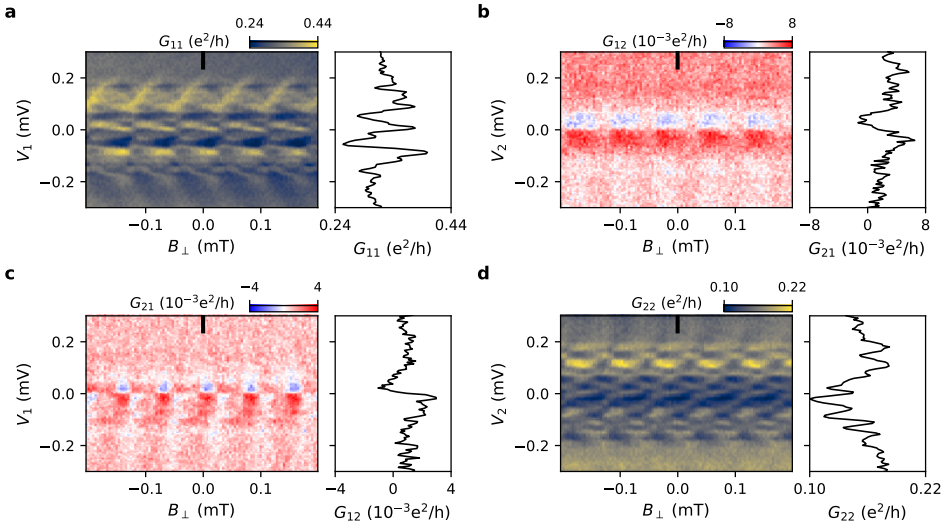

Figure 7.6: Local and nonlocal conductances at $B_\parallel = 700\,\mathrm{mT}$. The ZBP in G_{11} splits off from zero energy for the largest part of the phase range, while the one in G_{22} remains at zero energy. The sign inversions in the two nonlocal signals occur at opposing phase ranges.

Similar observations are made for the phase-biased JJ (see section 7.7.4 in the SI). At intermediate Zeeman fields, top and bottom local spectroscopy look increasingly different. After a gap closure, a phase-independent ZBP emerges in G_{11} but not in G_{22}. No gap is present in the nonlocal signals. A sign inversion in one of the nonlocal signals is observed, but cannot be correlated with the emergence of the ZBP. Sign inversions in the nonlocal signals as a function of gate voltages or Zeeman field have previously been related to either a change in the charge of an ABS [9, 14–16] or to a change in the charge preference of tunnel junctions [24].

7.6. CONCLUSION

In summary, we have performed local and nonlocal conductance measurements in planar, phase-biased JJs made in an InSbAs/Al 2DEG. As the Zeeman field is increased, the local and nonlocal signals become increasingly dissimilar. After a gap closure in local spectroscopy, we observe the emergence of phase-independent ZBPs, however mostly only at one end. Moreover, the nonlocal conductances show no gap reopening, only sign inversions that either start to appear at different phase ranges or cannot be correlated with the ZBP in local spectroscopy. The lack of stable, end-to-end correlated ZBPs and a bulk gap reopening suggest that a uniform topological regime is not reached within the investigated parameter space, most likely due to disorder in the JJs. Nevertheless, these measurements demonstrate how nonlocal conductance measurements in combination with two-ended local spectroscopy can help to distinguish between a trivial and a topological regime, and indicate a need for further material improvements.

Note added: During the preparation of this chapter, we became aware of a related work also addressing nonlocal conductance measurements in planar JJs [25].

7.7. SUPPLEMENTARY MATERIAL

7.7.1. INTERFERENCE PATTERNS FOR JJS IN SQUID

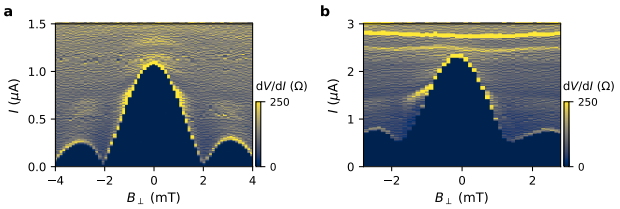

Figure 7.7: Fraunhofer interference pattern for the device JJ (**a**) and the reference JJ (**b**). In both measurements, the current bias, I, is applied to one of the contacts on the superconducting loop while the other is grounded, and the voltage drop between them, V, is measured. The contacts used for spectroscopy are floating. In **a** the supercurrent in the reference JJ is suppressed by applying $-2.5\,\mathrm{V}$ to the gate covering this JJ, in **b** there is no supercurrent flowing through the device JJ by applying $-2.0\,\mathrm{V}$ to the gate on the device JJ.

7.7.2. FIELD TRACKING FOR SQUID

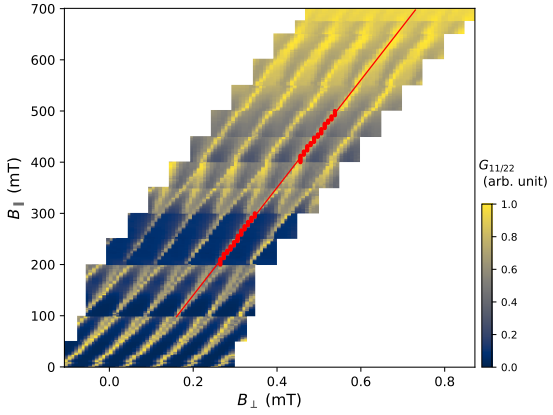

Figure 7.8: Phase slip tracing. The conductance maps up to $B_\parallel = 400\,\mathrm{mT}$ are obtained by applying a constant V_2 and measuring G_{22} as a function of $B_\perp$ and $B_\parallel$, keeping $V_1 = 0$. The maps for larger in-plane magnetic fields are obtained by applying a constant V_1 and measuring G_{11} as a function of $B_\perp$ and $B_\parallel$, keeping $V_2 = 0$. All conductances are normalized to their maximum value within each map. The red line is a fit to the extracted red maxima points. The effective $B_\perp = 0$ for $B_\parallel > 100\,\mathrm{mT}$ is defined as half of an oscillation period ($36.6\,\mu\mathrm{T}$) to the left of the red line.

7.7.3. ADDITIONAL ZEEMAN FIELDS FOR SQUID

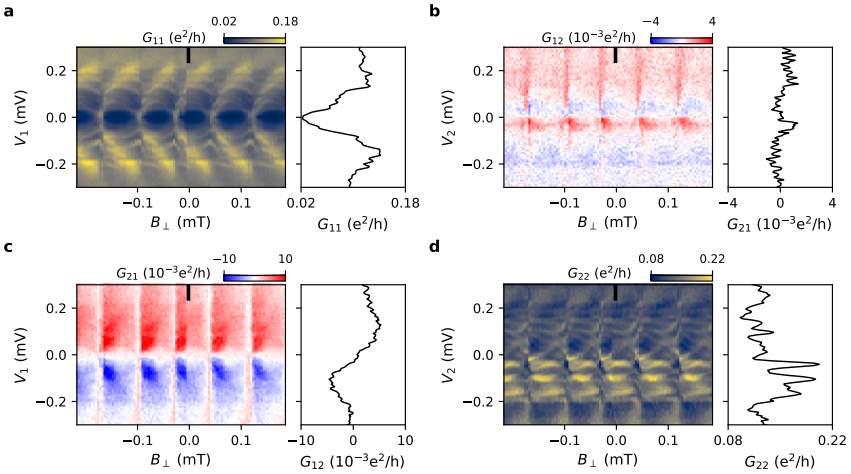

Figure 7.9: Local and nonlocal conductances at $B_\parallel = 400\,\mathrm{mT}$. A phase-independent gap closure occurs in G_{22}, while a gap remains in G_{11} and in the nonlocal signals.

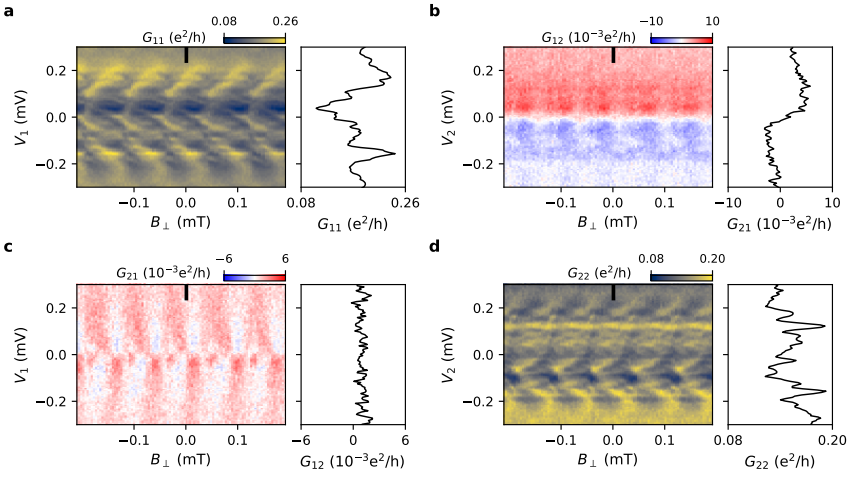

Figure 7.10: Local and nonlocal conductances at $B_\parallel = 550\,\mathrm{mT}$. A phase-independent gap closure happens in G_{11}, the gap in G_{22} is still closed. The gap vanishes in the nonlocal signals (weak sign inversions occur in G_{21}).

7.7.4. LOCAL AND NONLOCAL CONDUCTANCES FOR PHASE-BIASED JJ

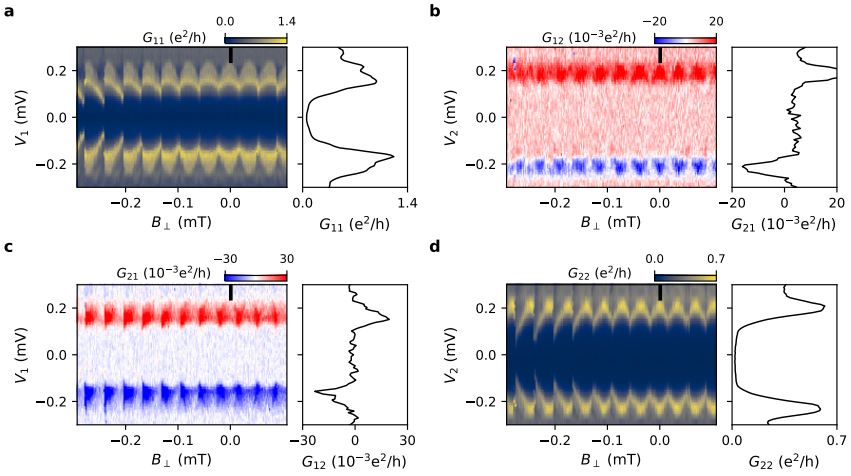

Figure 7.11: Local and nonlocal conductances at $B_\parallel = 0$. Local signals show phase-dependence with a slightly smaller gap in G_{11}. Nonlocal signals display a weak phase dependence with a smaller gap size in G_{21} as observed in local spectroscopy on the current-injecting side (G_{11}).

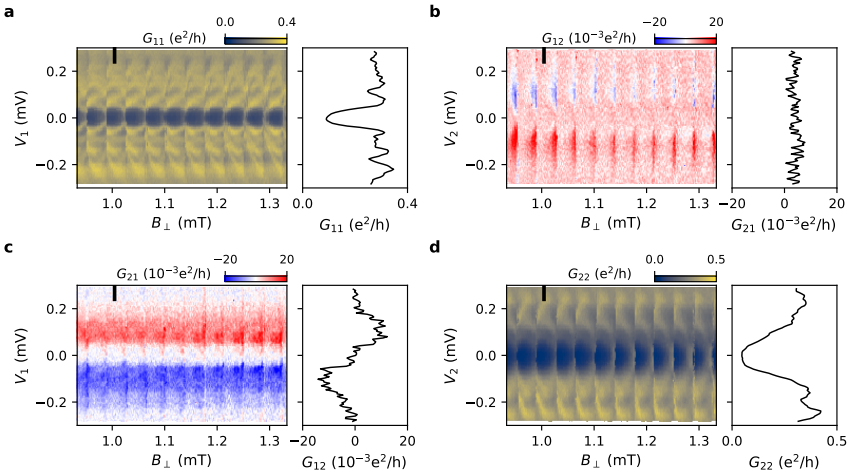

Figure 7.12: Local and nonlocal conductances at $B_\parallel = 250\,\mathrm{mT}$, no correction for the perpendicular component of the Zeeman is applied. The gap sizes shrink and more states become visible in local spectroscopy.

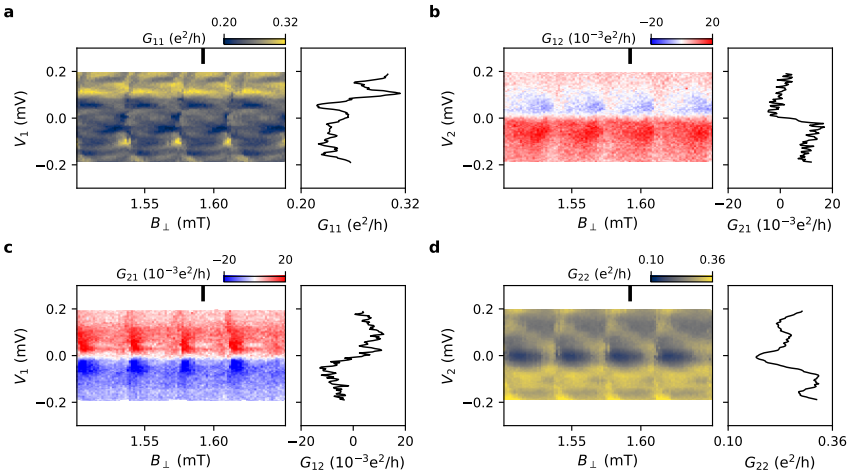

Figure 7.13: Local and nonlocal conductances at $B_\parallel = 400\,\mathrm{mT}$, no correction for the perpendicular component of the Zeeman is applied. Phase-independent gap closure in G_{11}, weak gap visible in G_{22}. No gaps in the nonlocal signals.

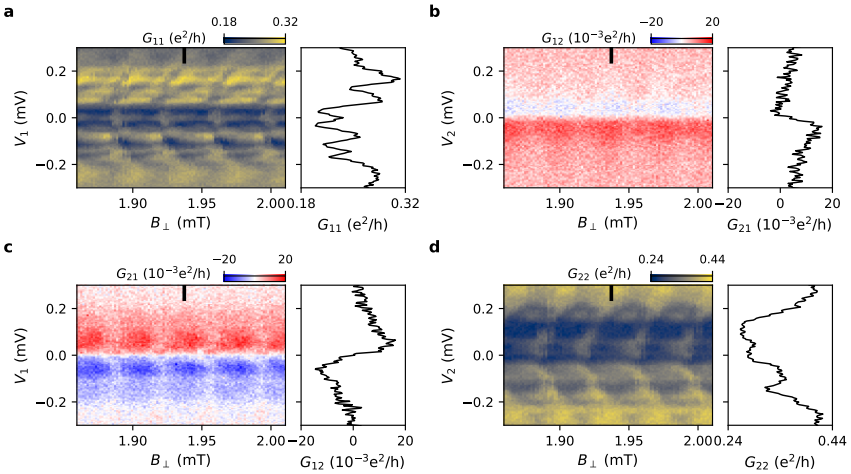

Figure 7.14: Local and nonlocal conductances at $B_\parallel = 500\,\mathrm{mT}$, no correction for the perpendicular component of the Zeeman is applied. Phase-independent ZBP emerges in G_{11}, but not in G_{22}. No gaps in the nonlocal signals.

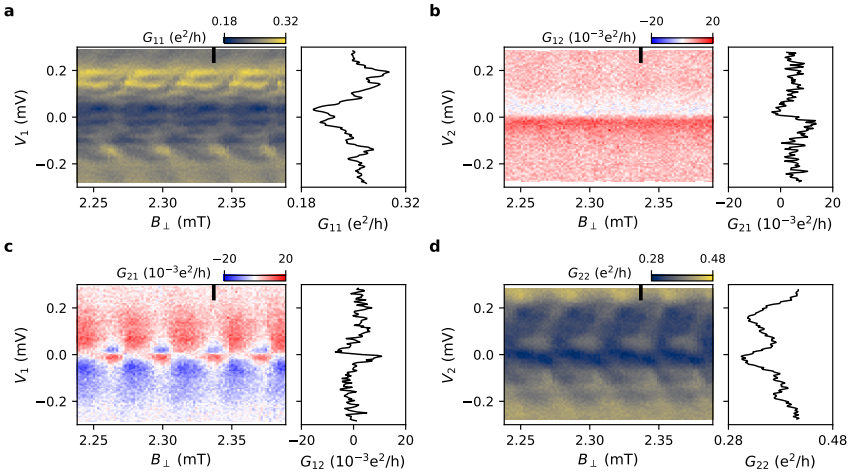

Figure 7.15: Local and nonlocal conductances at $B_\parallel = 600\,\mathrm{mT}$, no correction for the perpendicular component of the Zeeman is applied. Phase-independent ZBP remains in G_{11}, no zero-energy state in G_{22}. No gaps in the nonlocal signals, but sign inversions in G_{21}.

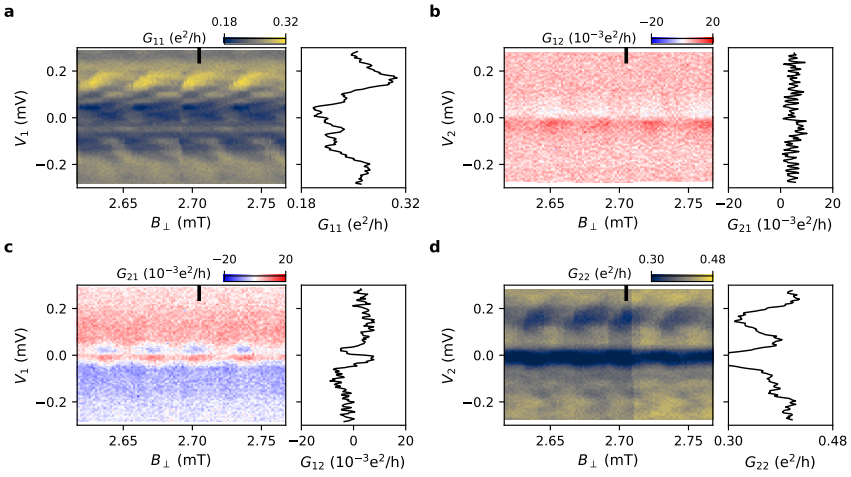

Figure 7.16: Local and nonlocal conductances at $B_\parallel = 700\,\mathrm{mT}$, no correction for the perpendicular component of the Zeeman is applied. Zero-energy state in G_{11} has disappeared, however the sign inversions in G_{21} remain.

REFERENCES

1. Lutchyn, R. M., Sau, J. D. & Das Sarma, S. Majorana Fermions and a Topological Phase Transition in Semiconductor-Superconductor Heterostructures. *Phys. Rev. Lett.* **105,** 077001 (2010).
2. Oreg, Y., Refael, G. & von Oppen, F. Helical Liquids and Majorana Bound States in Quantum Wires. *Phys. Rev. Lett.* **105,** 177002 (2010).
3. Aguado, R. Majorana quasiparticles in condensed matter. *La Rivista del Nuovo Cimento* **40,** 523–593 (2017).
4. Lutchyn, R. M., Bakkers, E. P. A. M., Kouwenhoven, L. P., Krogstrup, P., Marcus, C. M. & Oreg, Y. Majorana zero modes in superconductor–semiconductor heterostructures. *Nature Reviews Materials* **3,** 52–68 (2018).
5. Prada, E., San-Jose, P., de Moor, M. W. A., Geresdi, A., Lee, E. J. H., Klinovaja, J., Loss, D., Nygård, J., Aguado, R. & Kouwenhoven, L. P. From Andreev to Majorana bound states in hybrid superconductor–semiconductor nanowires. *Nature Reviews Physics* **2,** 575–594 (2020).
6. Pan, H. & Das Sarma, S. Physical mechanisms for zero-bias conductance peaks in Majorana nanowires. *Phys. Rev. Research* **2,** 013377 (2020).
7. Vuik, A., Nijholt, B., Akhmerov, A. R. & Wimmer, M. Reproducing topological properties with quasi-Majorana states. *SciPost Phys.* **7,** 61 (2019).
8. Rosdahl, T. Ö., Vuik, A., Kjaergaard, M. & Akhmerov, A. R. Andreev rectifier: A nonlocal conductance signature of topological phase transitions. *Phys. Rev. B* **97,** 045421 (2018).
9. Danon, J., Hellenes, A. B., Hansen, E. B., Casparis, L., Higginbotham, A. P. & Flensberg, K. Nonlocal Conductance Spectroscopy of Andreev Bound States: Symmetry Relations and BCS Charges. *Phys. Rev. Lett.* **124,** 036801 (2020).
10. Pan, H., Sau, J. D. & Das Sarma, S. Three-terminal nonlocal conductance in Majorana nanowires: Distinguishing topological and trivial in realistic systems with disorder and inhomogeneous potential. *Phys. Rev. B* **103,** 014513 (2021).
11. Hess, R., Legg, H. F., Loss, D. & Klinovaja, J. Local and nonlocal quantum transport due to Andreev bound states in finite Rashba nanowires with superconducting and normal sections. *Phys. Rev. B* **104,** 075405 (2021).
12. Maiani, A., Geier, M. & Flensberg, K. Conductance matrix symmetries of multiterminal semiconductor-superconductor devices. *Phys. Rev. B* **106,** 104516 (2022).

13. Pikulin, D. I., van Heck, B., Karzig, T., Martinez, E. A., Nijholt, B., Laeven, T., Winkler, G. W., Watson, J. D., Heedt, S., Temurhan, M., Svidenko, V., Lutchyn, R. M., Thomas, M., de Lange, G., Casparis, L. & Nayak, C. Protocol to identify a topological superconducting phase in a three-terminal device. https://arxiv.org/abs/2103.12217 (2021).

14. Ménard, G. C., Anselmetti, G. L. R., Martinez, E. A., Puglia, D., Malinowski, F. K., Lee, J. S., Choi, S., Pendharkar, M., Palmstrøm, C. J., Flensberg, K., Marcus, C. M., Casparis, L. & Higginbotham, A. P. Conductance-Matrix Symmetries of a Three-Terminal Hybrid Device. *Phys. Rev. Lett.* **124,** 036802 (2020).

15. Puglia, D., Martinez, E. A., Ménard, G. C., Pöschl, A., Gronin, S., Gardner, G. C., Kallaher, R., Manfra, M. J., Marcus, C. M., Higginbotham, A. P. & Casparis, L. Closing of the induced gap in a hybrid superconductor-semiconductor nanowire. *Phys. Rev. B* **103,** 235201 (2021).

16. Pöschl, A., Danilenko, A., Sabonis, D., Kristjuhan, K., Lindemann, T., Thomas, C., Manfra, M. J. & Marcus, C. M. Nonlocal conductance spectroscopy of Andreev bound states in gate-defined InAs/Al nanowires. https://arxiv.org/abs/2204.02430 (2022).

17. Hell, M., Leijnse, M. & Flensberg, K. Two-Dimensional Platform for Networks of Majorana Bound States. *Phys. Rev. Lett.* **118,** 107701 (2017).

18. Pientka, F., Keselman, A., Berg, E., Yacoby, A., Stern, A. & Halperin, B. I. Topological Superconductivity in a Planar Josephson Junction. *Phys. Rev. X* **7,** 021032 (2017).

19. Fornieri, A., Whiticar, A. M., Setiawan, F., Portolés, E., Drachmann, A. C. C., Keselman, A., Gronin, S., Thomas, C., Wang, T., Kallaher, R., Gardner, G. C., Berg, E., Manfra, M. J., Stern, A., Marcus, C. M. & Nichele, F. Evidence of topological superconductivity in planar Josephson junctions. *Nature* **569,** 89–92 (2019).

20. Ren, H., Pientka, F., Hart, S., Pierce, A. T., Kosowsky, M., Lunczer, L., Schlereth, R., Scharf, B., Hankiewicz, E. M., Molenkamp, L. W., Halperin, B. I. & Yacoby, A. Topological superconductivity in a phase-controlled Josephson junction. *Nature* **569,** 93–98 (2019).

21. Banerjee, A., Lesser, O., Rahman, M. A., Wang, H. .-., Li, M. .-., Kringhøj, A., Whiticar, A. M., Drachmann, A. C. C., Thomas, C., Wang, T., Manfra, M. J., Berg, E., Oreg, Y., Stern, A. & Marcus, C. M. Signatures of a topological phase transition in a planar Josephson junction. https://arxiv.org/abs/2201.03453 (2022).

22. Moehle, C. M., Ke, C. T., Wang, Q., Thomas, C., Xiao, D., Karwal, S., Lodari, M., van de Kerkhof, V., Termaat, R., Gardner, G. C., Scappucci, G., Manfra, M. J. & Goswami, S. InSbAs Two-Dimensional Electron Gases as a Platform for Topological Superconductivity. *Nano Letters* **21,** 9990–9996 (2021).

23. Martinez, E. A., Pöschl, A., Hansen, E. B., van de Poll, M. A. Y., Vaitiekėnas, S., Higginbotham, A. P. & Casparis, L. Measurement circuit effects in three-terminal electrical transport measurements. https://arxiv.org/abs/2104.02671 (2021).

24. Wang, G., Dvir, T., van Loo, N., Mazur, G. P., Gazibegovic, S., Badawy, G., Bakkers, E. P. A. M., Kouwenhoven, L. P. & de Lange, G. Nonlocal measurement of quasiparticle charge and energy relaxation in proximitized semiconductor nanowires using quantum dots. *Phys. Rev. B* **106,** 064503 (2022).

25. Banerjee, A., Lesser, O., Rahman, M. A., Thomas, C., Wang, T., Manfra, M. J., Berg, E., Oreg, Y., Stern, A. & Marcus, C. M. Local and Nonlocal Transport Spectroscopy in Planar Josephson Junctions. `https://arxiv.org/abs/2205.09419` (2022).

8

CONCLUSION AND OUTLOOK

8.1. CONCLUSIONS

CHAPTER 4

In chapter 4, we demonstrated for the first time induced superconductivity in InSb 2DEGs. This was done by contacting the buried 2DEG, having a peak mobility of more than 150 000 cm^2/Vs, by the ex-situ deposited superconductor NbTiN, forming planar JJs. We observed supercurrents in devices with a length of up to $L = 4.7\,\mu$m, with signatures of ballistic superconductivity (i.e., a $1/L$ scaling of the $I_s R_n$ product for $L < 2.7\,\mu$m). An in-plane magnetic field produced revivals of the supercurrent that we associated with $0-\pi$ transitions. We explicitly showed the tunability of the $0-\pi$ transition field with the junction length and the electron density in the semiconductor, in quantitative agreement with the theory of $0-\pi$ transitions in ballistic JJs. The electron density dependence allowed us to rapidly switch between the 0 and π-regime at a fixed magnetic field using gate voltages.

According to Pientka et al [1], the transition to the π-state in a planar JJ made in a 2DEG with strong Rashba spin-orbit coupling is accompanied by a topological phase transition, when the magnetic field is applied along the semiconductor-superconductor interfaces. However, this assumes a fully ballistic junction with Rashba SOC only, while InSb is known to also have a Dresselhaus contribution. Reaching the topological regime in the presence of Dresselhaus SOC requires a careful orientation of the magnetic field depending on the relative strength of the Rashba and Dresselhaus contributions [2]. Besides, making a more conclusive statement about a potential topological phase transition would require a direct detection mechanism. In this regard, tunneling spectroscopy can be performed at the two ends of the JJ, where one would expect to measure zero-bias peaks in the topological regime due to the MZMs. We fabricated new sets of JJs equipped with tunneling probes, but were unable to perform reliable spectroscopy measurements because of two main shortcomings: noisy dielectrics, and broken gates due to standing walls at the edges of the sputtered NbTiN contacts. Another important consideration is the size of the potential topological gap. For long junctions ($\hbar^2/m^*L^2 < \Delta$), the size of the topological gap can at most be on the order of $\hbar^2/m^*L^2$, amounting to $\sim 3\,\mu$eV for our 1.1 μm long junction (note that the actual value also depends strongly on parameters such as the strength of the spin-orbit coupling, and the magnitude and direction of the applied Zeeman field) [1, 3]. Hence, in order to obtain a more sizable topological gap, one should decrease the junction length, which would however also increase the $0-\pi$ transition field.

This tradeoff can be prevented by using phase-biased JJs instead, where the topological regime can be reached at a low magnetic field when the superconducting phase difference is tuned to π, provided that the JJ has a large transparency. Our JJs had only moderate transparencies in the range of $0.6-0.7$, so moving forward a better semiconductor-superconductor interface was required. Inspired by the results on InAs/Al and InSb/Al nanowires and InAs/Al 2DEGs, we grew a thin layer of the superconductor Al in-situ on the semiconductor hetereostructure. However, we did not observe induced superconductivity, even when removing the top-barrier completely and growing the Al directly on top of the InSb.

CHAPTER 5

In chapter 5, we demonstrated that in-situ grown Al proximitizes InSbAs surface 2DEGs. Using tunneling spectroscopy, we showed a hard induced superconducting gap in the semiconductor, indicative of the clean semiconductor-superconductor interface. Apart from the feasibility of induced superconductivity, we demonstrated that the bare ternary semiconductor InSbAs has other beneficial properties for the realization of topological superconductivity: strong Rashba spin-orbit coupling that is tunable by the As concentration, a large perpendicular effective g-factor (~ 55), and a low effective electron mass ($\sim 0.016 m_e$). However, the absence of the top-barrier comes at the price of a significantly reduced peak mobility ($\sim 25\,000\,\mathrm{cm}^2/\mathrm{Vs}$) compared to the buried InSb 2DEGs investigated in the previous chapter. Taking advantage of the design flexibility of this material system, we realized three prototypical device geometries to study MZMs: planar phase-biased JJs, superconducting islands and superconducting strips.

CHAPTER 6

Chapter 6 focused on tunneling spectroscopy measurements on both ends of planar phase-biased JJs in the absence of a Zeeman field. We found distinct differences between the tunneling maps obtained on both ends of the junctions, which could be explained by taking into account the local superconducting phase difference and the inductance of the superconducting loop. Numerical simulations confirmed that the tunneling current is only sensitive to Andreev bound states localized in the vicinity of the respective tunneling barrier, and that these states are affected differently by the local superconducting phase difference having an equal magnitude but opposite sign on the two ends of the JJs. Moreover, we used the resulting phase shifts to determine the relative positions of individual ABSs in the junctions.

CHAPTER 7

In chapter 7, we complemented tunneling spectroscopy measurements in planar phase-biased JJs with nonlocal conductance measurements, and obtained all four conductances at varying Zeeman fields. As the in-plane magnetic field was increased, the two local and nonlocal signals became increasingly dissimilar, likely due to disorder in the junctions. After a gap closure in local spectroscopy, zero-bias peaks emerged (hardly phase-tunable), however mostly at one end. Moreover, we found no clear evidence of a gap re-opening in the nonlocal signals. The lack of end-to-end correlated zero-energy states in local spectroscopy and the absence of a gap re-opening in the nonlocal signals suggest that further material improvements are required to realize a uniform, extended topological region.

8.2. HETEROSTRUCTURE OPTIMIZATIONS

In chapter 7, we encountered that the induced superconducting gap became soft in the presence of an in-plane magnetic field and that zero-bias peaks were weak and unstable, without clear end-to-end correlation. Furthermore, we did not find evidence for a re-opening of the bulk superconducting gap. These features are prevalent in experiments reported in the literature (across various material platforms), and are expected when disorder plays an important role in the hybrid devices [4]. Therefore, future heterostructures should be designed with the aim to reduce disorder as much as possible. Notably, the disorder may stem from the semiconductor heterostructure itself, the superconductor, the interface, or the device fabrication.

Insights into the cleanliness of the semiconductor heterostructure can be gained by measuring the mobility in a Hall bar geometry with the superconductor removed. In chapter 5, we have already noticed that the peak mobility is similar for all As concentrations, suggesting that alloy scattering is not the limiting factor at this point. Instead, it is likely the proximity to the surface (surface roughness scattering) that hampers the mobility. Therefore, one should incorporate a top-barrier in upcoming heterostructures. Apart from increasing the mobility, the top-barrier reduces the strength of the Rashba SOC and the coupling to the superconductor. This has to be taken into account when optimizing the mobility and one has to strike a balance.

In an attempt to improve the mobility, we grew an InSbAs/Al heterostructure with a 5 nm thick InSb top-barrier (see schematic of the layer stack in Fig. 8.1a). We observed an increase in the peak mobility by approximately a factor of two, to $\sim 43\,000\,\mathrm{cm}^2/\mathrm{Vs}$ (see Fig. 8.1b), while still being able to induce superconductivity as shown in Fig. 8.1c. To put this number into context, it corresponds to a level broadening ($\hbar e/2m^*\mu$) of about 1 meV, which is large compared to the expected size of the topological gap (< 0.1 meV). Similarly, reported fits to mobility-density curves for InAs and InSb 2DEGs with peak mobilities in the range of $12\,000\,\mathrm{cm}^2/\mathrm{Vs}$ to $45\,000\,\mathrm{cm}^2/\mathrm{Vs}$, yield charge impurity densities between $3.4\times10^{17}\,\mathrm{cm}^{-3}$ and $1.4\times10^{19}\,\mathrm{cm}^{-3}$, well above the limit of $1\times10^{15}\,\mathrm{cm}^{-3}$ that is necessary for the manifestation of topological superconductivity [4, 5]. Achieving a level broadening of 0.1 meV would require a mobility of $\sim 400\,000\,\mathrm{cm}^2/\mathrm{Vs}$. InSbAs 2DEGs with 40 nm AlInSb top-barrier have recently shown peak mobilities exceeding $200\,000\,\mathrm{cm}^2/\mathrm{Vs}$, but the ability to induce superconductivity was not demonstrated [6]. As a next step, it should be tested what mobilities can be achieved without sacrificing induced superconductivity.

Further mobility improvements might also be possible by using a different barrier material. One candidate is CdTe as it nearly matches the lattice constant of InSb and results in a type-I band alignment, with evidence of increased Rashba SOC [7, 8]. Additionally, one could try different substrate materials. It was for example shown that the peak mobility of near-surface InAs 2DEGs (20 – 25 nm deep) reached values in excess of $2\,000\,000\,\mathrm{cm}^2/\mathrm{Vs}$ by switching from an InP to a nearly lattice-matched GaSb substrate [9, 10].

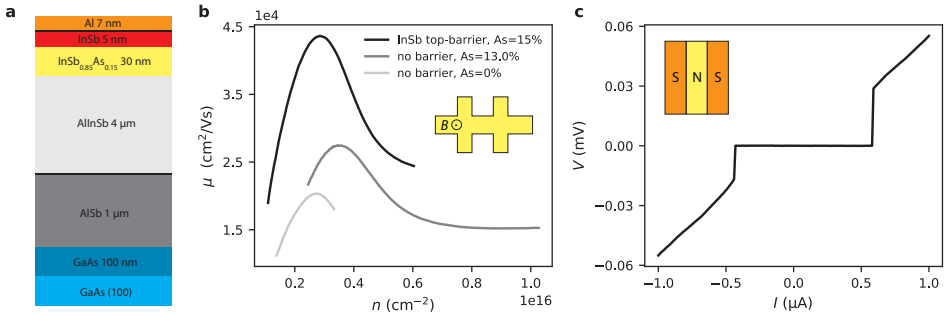

Figure 8.1: **a,** Schematic of an InSbAs/Al heterostructure with a 5 nm thick InSb top-barrier. **b,** Comparison of mobility vs. density curves for heterostructures with and without top-barrier, measured using gated Hall bars. **c,** V-I curve measured in a Josephson junction fabricated in the top-barrier wafer. The JJ is 10 μm wide with a separation of 500 nm between the superconducting contacts.

8.3. KITAEV CHAIN

Heterostructure optimizations are usually time-consuming and it is unclear if sufficient mobility values can be reached while preserving induced superconductivity. Therefore, in parallel, one should pursue an alternative approach to create MZMs that is less prone to disorder. This is the case for the so-called Kitaev chain, which can be realized by connecting spin-polarized quantum dots via s-wave superconductors [11, 12]. Under the appropriate conditions, one MZM forms at each end of the chain. The simplest version of this is a double quantum dot connected via a common superconducting lead (see Fig. 8.2a). The dots are coupled by elastic co-tunneling (ECT) where a single electron hops from one dot to the other via the superconductor, and by a coherent crossed Andreev reflection (CAR) process where an incoming electron from the right dot is reflected non-locally into a hole in the left dot. It was predicted that by changing the angle between the magnetic fields at the two quantum dots, the normal and superconducting coupling can be tuned to become equal, leading to the emergence of one poor man's Majorana (PMM) on each dot [13]. These states are not protected to the same degree but otherwise share the properties of regular MZMs. A more recent proposal shows that the couplings can also be mediated by Andreev bound states (ABSs) that reside in a semiconducting-superconducting hybrid section connecting the two dots. Moreover, it was predicted that the relative strength of the couplings is tunable by an electrostatic gate covering the hybrid section and controlling the charge and energy of the ABSs [14]. This eliminates the need for the two tilted fields, making this proposal experimentally feasible since the only required ingredients are spin-polarized quantum dots and a hybrid segment with spin-orbit coupling. In fact, by tuning the relative strength of ECT and CAR, a Cooper pair splitter with high efficiency and a Kitaev chain of two sites were realized using hybrid nanowire devices [15, 16].

Building upon this, and the material and fabrication developments in this thesis, one

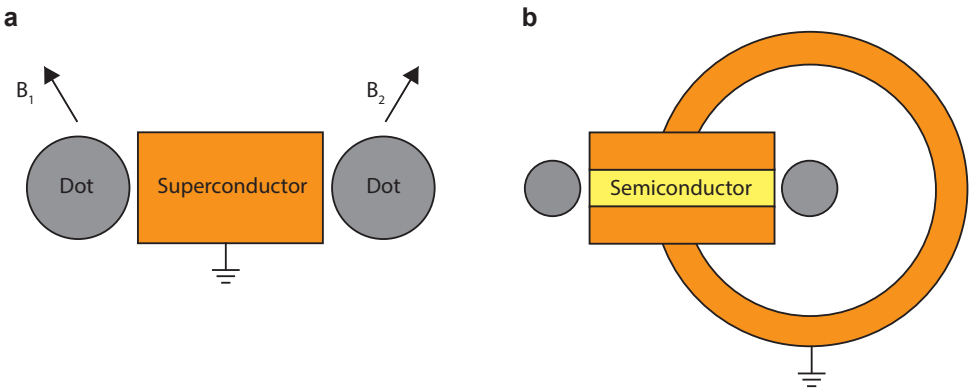

Figure 8.2: **a,** Schematic of a device consisting of two spin-polarized quantum dots coupled via an s-wave superconductor. Two tilted magnetic fields are used to change the spin polarization in different directions in the dots. **b,** Quantum dots connected via a phase-biased Josephson junction. The ABSs in the semiconducting region of the JJ mediate the normal and superconducting coupling between the dots.

could couple two quantum dots via ABSs hosted in a 2DEG-based phase-biased JJ (see Fig. 8.2b), where the ABS energy (and therefore the strength of CAR and ECT) can be controlled by the superconducting phase difference, φ. At $\varphi = \pi$ (ABS energy minimal) one would expect CAR to be the strongest, while at $\varphi = 0$ (ABS energy maximal) CAR should be weak. Hence, one can realize a phase-controllable Cooper-pair splitter.
Besides, the flexibility of the 2DEG platform should allow to manufacture more complex chains with a larger number of sites (in a non-phase-biased geometry), therefore creating MZMs instead of PMMs. While PMMs are not protected against deviations in the couplings (equal normal and superconducting coupling is strictly required) [13], one should see a growing tolerance against such fluctuations when increasing the number of quantum dots [11]. It was argued that 5 sites should already be sufficient for a protected Kitaev chain [11]. Promising steps towards a 2DEG-based Kitaev chain have recently been taken [17].

REFERENCES

1. Pientka, F., Keselman, A., Berg, E., Yacoby, A., Stern, A. & Halperin, B. I. Topological Superconductivity in a Planar Josephson Junction. *Phys. Rev. X* **7,** 021032 (2017).
2. Pekerten, B., Pakizer, J. D., Hawn, B. & Matos-Abiague, A. Anisotropic topological superconductivity in Josephson junctions. *Phys. Rev. B* **105,** 054504 (2022).
3. Scharf, B., Pientka, F., Ren, H., Yacoby, A. & Hankiewicz, E. M. Tuning topological superconductivity in phase-controlled Josephson junctions with Rashba and Dresselhaus spin-orbit coupling. *Phys. Rev. B* **99,** 214503 (2019).
4. Ahn, S., Pan, H., Woods, B., Stanescu, T. D. & Das Sarma, S. Estimating disorder and its adverse effects in semiconductor Majorana nanowires. *Phys. Rev. Materials* **5,** 124602 (2021).
5. Woods, B. D., Das Sarma, S. & Stanescu, T. D. Charge-Impurity Effects in Hybrid Majorana Nanowires. *Phys. Rev. Applied* **16,** 054053 (2021).
6. Metti, S., Thomas, C., Xiao, D. & Manfra, M. J. Spin-orbit coupling and electron scattering in high-quality $InSb_{1-x}As_x$ quantum wells. *Phys. Rev. B* **106,** 165304 (2022).
7. Badawy, G., Zhang, B., Rauch, T., Momand, J., Koelling, S., Jung, J., Gazibegovic, S., Moutanabbir, O., Kooi, B. J., Botti, S., Verheijen, M. A., Frolov, S. M. & Bakkers, E. P. A. M. Electronic Structure and Epitaxy of CdTe Shells on InSb Nanowires. *Advanced Science* **9,** 2105722 (2022).
8. Zhang, Y., Xue, F., Tang, C., Li, J., Liao, L., Li, L., Liu, X., Yang, Y., Song, C. & Kou, X. Highly Efficient Electric-Field Control of Giant Rashba Spin–Orbit Coupling in Lattice-Matched InSb/CdTe Heterostructures. *ACS Nano* **14,** 17396–17404 (2020).
9. Tschirky, T., Mueller, S., Lehner, C. A., Fält, S., Ihn, T., Ensslin, K. & Wegscheider, W. Scattering mechanisms of highest-mobility $InAs/Al_xGa_{1-x}Sb$ quantum wells. *Phys. Rev. B* **95,** 115304 (2017).
10. Thomas, C., Hatke, A. T., Tuaz, A., Kallaher, R., Wu, T., Wang, T., Diaz, R. E., Gardner, G. C., Capano, M. A. & Manfra, M. J. High-mobility InAs 2DEGs on GaSb substrates: A platform for mesoscopic quantum transport. *Phys. Rev. Materials* **2,** 104602 (2018).
11. Sau, J. D. & Sarma, S. D. Realizing a robust practical Majorana chain in a quantum-dot-superconductor linear array. *Nature Communications* **3,** 964 (2012).
12. Pan, H. & Das Sarma, S. Disorder effects on Majorana zero modes: Kitaev chain versus semiconductor nanowire. *Phys. Rev. B* **103,** 224505 (2021).
13. Leijnse, M. & Flensberg, K. Parity qubits and poor man's Majorana bound states in double quantum dots. *Phys. Rev. B* **86,** 134528 (2012).

14. Liu, C.-X., Wang, G., Dvir, T. & Wimmer, M. Tunable superconducting coupling of quantum dots via Andreev bound states in semiconductor-superconductor nanowires. https://arxiv.org/abs/2203.00107 (2022).

15. Wang, G., Dvir, T., Mazur, G. P., Liu, C.-X., van Loo, N., Haaf, S. L. D. t., Bordin, A., Gazibegovic, S., Badawy, G., Bakkers, E. P. A. M., Wimmer, M. & Kouwenhoven, L. P. Singlet and triplet Cooper pair splitting in superconducting-semiconducting hybrid nanowires. https://arxiv.org/abs/2205.03458 (2022).

16. Dvir, T., Wang, G., van Loo, N., Liu, C.-X., Mazur, G. P., Bordin, A., Haaf, S. L. D. t., Wang, J.-Y., van Driel, D., Zatelli, F., Li, X., Malinowski, F. K., Gazibegovic, S., Badawy, G., Bakkers, E. P. A. M., Wimmer, M. & Kouwenhoven, L. P. Realization of a minimal Kitaev chain in coupled quantum dots. https://arxiv.org/abs/2206.08045 (2022).

17. Wang, Q., Haaf, S. L. D. t., Kulesh, I., Xiao, D., Thomas, C., Manfra, M. J. & Goswami, S. Triplet Cooper pair splitting in a two-dimensional electron gas. https://arxiv.org/abs/2211.05763 (2022).

ACKNOWLEDGEMENTS

Doing my PhD at QuTech was a truly amazing experience and I am grateful for the support of many people.
Firstly, **Srijit**, thanks for taking me on as a PhD student in your back then brand new lab. You have been a great supervisor and guided me very well along this journey. I very much appreciated your hands-on supervision style and that your door was always open to discuss anything. All the friendly words aside, I have to say that I am not too impressed with your dart skills (as well as the fact that I wasn't allowed to measure those AB rings).
I would also like to thank **Leo** for being my promotor and providing important feedback over the years. Thanks to **Yuli**, **Lieven**, **Toeno**, **Klaus** and **Javad** for reviewing my thesis and being part of the committee.

Ting, I had the pleasure to share almost my entire PhD with you. You showed me the rope on essentially everything, from device fabrication to fridge operation. I will never forget how we accidentally discovered that NbTiN makes good contact to InSb 2DEGs and the excitement afterwards. Let me know if the Harry Potter chamber is still available in your house and I may join as your lab assistant. **Fokko**, due to your efforts Ting and I didn't have to start from square zero, and you taught us important experimental skills. Besides, you were always keen to discuss results and provided a critical eye. Having you around was a lot of fun. **Ivan**, I have been very impressed by how quickly you learn new things and how you constantly question the status quo to improve fabrication and measurement procedures. It was awesome hanging out after work, and I am glad to have you as my paranymph. **Qing**, thanks for numerous good discussions and lunch breaks. I am happy to hear that the new devices are working so well, good luck finishing your PhD. It's an honor having you as a paranymph. By the way, challenging you on the practice run was a big mistake. **Prasanna**, it was nice to collaborate on the phase-biased junctions for a bit. All the best with your new position in Munich. I (and the CCC truck) will miss you. I would also like to express my gratefulness to the other members of the 2D topo group (past or present): **Saurabh**, **Nikos**, **Vincent**, **Damien**, **Jakob**, **Yining**, **Christian P.** and **Bas**. I very much enjoyed the meetings, journal clubs and uitjes.

During my PhD I had the opportunity to supervise a few Master students. **Michael (SQUIDman)**, you became independent very quickly and worked extremely hard. There was a lot of blood, sweat and tears involved due to a misbehaving Super-AJA but you accepted the challenge and obtained great results, almost having to present in the SQUID costume. After-work activities with you were always a blast. **Ruben**, you joined when we just started with the ternary 2DEGs, and **Sander** when we were plagued by noisy dielectrics and the corona pandemic. Nevertheless, both of you did a great job and pushed the project forward. **Nayan**, I only supervised you in the beginning, but you put in an

enormous effort and it was fantastic to see how the spectroscopy maps (and memes) kept improving.

This thesis hadn't been possible without the excellent materials grown in **Michael Manfra**'s group at Purdue University. I would like to thank the whole team and especially **Candice**, **Di** and **Sara** for the good collaboration.
Moreover, I want to thank **Michał** and **Dibyendu** from AGH University of Science and Technology in Cracow. It was great collaborating with you and I learned a lot from our discussions.

I still remember when I first came to Delft for my interview, visiting the topo group. Apart from the cutting-edge research and impressive facilities it immediately felt like a place with a good working atmosphere where people also have fun outside of work. This turned out to be exactly true. **Michiel**, thanks for plenty of awesome nights at proofy, carrying team speed-dating and organizing various other events. **Alex**, you were the reason why my coffee consumption increased by a factor of 10. I very much enjoyed the obstacle runs, doing crossfit, and visiting the most beautiful stadium in the world so that you could finally become a supporter of the right team. **Luca**, my other ex-crossfit buddy, it was sad to see you and **Nicolò** go but I am glad that both of you are doing well back home. **Jasper**, playing football and darts with you was a lot of fun. **Damaz**, I have fond memories of the San Sebastian conference and drinking wine at unreasonably early times. You were also part of the Denver roadtrip gang along with **Arno**, **Willemijn**, **Marta** and **Lukas G.**. Too bad that the actual conference didn't happen but it was a true pleasure playing risk, snowboarding the Rocky mountains and going glamping. I am still a bit traumatized by that one song.
I would also like to thank **James**, **Jouri**, **Daniël**, **Elvedin**, **Amrita**, **Nicolai**, **Matt**, **Guan**, **Di**, **Lukas S.**, **Jaap**, **Nick**, **Greg**, **Cristina**, **Tom**, **David**, **Lin**, **Vukan**, **Filip**, **Michael C.** and all other members of the topo group for the nice atmosphere.

A very important reason why QuTech is such a special place is its excellent support staff and technicians. I would like to thank **Jenny** and **Csilla** for assistance with various administrative matters, all of the cleanroom staff for the hard work to keep this place in good shape, and **Olaf**, **Jason** and **Raymond** for support with the experimental setups.

Mondays were always my favorite days due to the football matches with the Kavli Warriors. It was great to see how we developed from a "bunch of random people playing soccer" to a real team. If corona hadn't stopped us we would have won the league a couple of times. But most importantly, it was fantastic to meet so many great people from different QuTech divisions that would have otherwise remained strangers. **Maarten**, aka the star of the team, I hope one day you will learn how to play football without getting your knees bloody. **Thijs**, it's been great having you in the team and hanging out outside of the pitch. Thank god we discovered your skills as a striker. Have you found the balls yet that you sent to the roof? **Stefano**, surrounded by quantum physicists you stood your man as a PhD student in ???. I greatly enjoyed playing football with you and the good vibes you brought to the Warriors. **Gustavo**, our de-facto captain, the above mentioned transfor-

mation of the team is largely thanks to you. With your charm and Brazilian temperament you keep the team together like glue. Also, you are my favorite drummer (as I might have mentioned before). **Francesco**, what Pirlo was to Italy you are to the Warriors. **Alberto**, the powerhouse, impressive how you can sprint non-stop, just to do the exact same thing in the directly following match as a guest player. **Jorge**, you give the opponents headache with your pace and dribblings. **Mark**, when you joined, the defense became much more solid while you constantly initiated great attacks as well. **Valentinho**, the name says it all, thanks also for bringing the sharp new outfit to the team. **Anta(aaa)**, it was always great fun having you on the field. Too bad we lost you so you can focus on your career as a professional kart driver. **Sword**, mostly present in the Whatsapp group (and on TV), but when you were in the goal you lifted the team to the next level. Thanks also to the past members **Luca P.**, **Kaushik**, **Constantijn**, **Tim**, **Sebastian**, and a shout-out to my second favorite team, **Brecht**'s team, for various fun practice matches during the summers.
Another great overarching QuTech event are the uitjes. **Victoria**, **Maarten**, **Sjaak** and **Marta**, I very much enjoyed organizing the Texel one with you, going on the pre-uitje and flipping a few mattresses.

I had the pleasure to know **Prof. Yuki** and **Dr. Dong van Delft** since the beginning of my PhD time. It was awesome playing all sorts of games and cooking delicious meals. Moreover, I feel that I now know practically all good Chinese restaurants in the area.

Wanneer ik niet in Delft was, bracht ik talloze weekenden door in Heemskerk. **Lida** en **Ron**, **Sanne** en **Luke**, **Jack**, **Polly** en **Snoes**, bedankt voor de gezelligheid. Ik heb altijd erg genoten van de bezoeken.

Auf Besuche in der Heimat habe ich mich immer besonders gefreut, auch wenn sie leider nicht so zahlreich ausgefallen sind wie erhofft. Ich bin unfassbar stolz einen Freund wie dich, **Enrico**, seit der Grundschule an meiner Seite zu haben. Gleiches gilt für die Heistmer Jungs **Termin**, **Willy** und **Kalla**. Hoffentlich bin ich bald wieder in der Nähe.
Philippo Gonzalez Dani Dani Alvez, **Henne**, **Sven**, **Robyn**, **Anni**, **Didi** und **Franzi**, seit der guten alten LMG-Zeit schweißt uns unsere Liebe für Korn, Busfahren, Festivals und Dänemark zusammen. Ich freue mich schon aufs nächste Event. Nicht zu vergessen auch die Electro-Swing-Partys mit **Agnes** und **Anna**.
Gevin, **Leon** und **Felix**, an die Bachelorzeit in Göttingen denke ich immer gerne zurück, auch wenn sie oft sehr stressig war. Ohne unsere Lerngruppe, die Tiefseetaucher und die Nordmensa wäre ich heute nicht hier.
Andreas, **Hampus** och **George**, det var fantastiskt att plugga med er i Lund. Jag har goda minnen av allt det galna vi gjorde utanför universitetet, särskilt Greklandsresorna och att campa utan sovsäck.

Ein besonderer Dank gebührt meiner Familie. **Elisabeth** und **Uwe**, **Rebecca** und **Dennis**, **Leonie** und **Patrick**, Treffen mit euch sind immer großartig, besonders wenn die Spiele-Hölle eröffnet wird. Einen großen Dank auch an **Helena** und **Jörn**, **Nelson** und Fußballstar **Leonel**, sowie an die Familie in Grieben.
Ganz besonders bedanken möchte ich mich auch bei der **Frau aus Osnabrück** und **Opa**

für die anhaltende Unterstützung, das große Interesse an meinem Werdegang und dafür, dass die Tür für Besuche immer offen steht.
Flo, Bruderherz, ich bin unfassbar stolz auf dich und wünsche dir und **Agnes** nur das Beste. Ich freue mich schon aufs Surfen in Down Under. **Mama** und **Papa**, danke, dass ihr immer an mich glaubt und immer für mich da seid. Eure Unterstützung ist fantastisch.

Last but not least, **Elly**, we hebben een geweldige tijd samen. Bedankt dat je me in soms moeilijke tijden steunt en me altijd aan het lachen maakt. Ik ben benieuwd wat de toekomst ons brengt.

CURRICULUM VITÆ

Christian Mario MÖHLE

22-12-1991	Born in Münster, Germany.
2002 – 2011	Secondary school, Ludwig-Meyn-Gynasium Uetersen, Germany.
2012 – 2015	Bachelor of Science in Physics, University of Göttingen, Germany. *Supervisor:* Prof. Dr. Martin Wenderoth
2015 – 2017	Master of Science in Physics, Lund University, Sweden. *Supervisor:* Prof. Erik Lind
2017 – 2022	PhD in Physics, Delft University of Technology, the Netherlands. *Supervisors:* Prof. dr. ir. Leo P. Kouwenhoven and Dr. Srijit Goswami

List of Publications

6. *Controlling Andreev bound states with the magnetic vector potential*
Christian M. Moehle*, Prasanna K. Rout*, Nayan A. Jainandunsing, Dibyendu Kuiri, Chung Ting Ke, Di Xiao, Candice Thomas, Michael J. Manfra, Michal P. Nowak, Srijit Goswami
Nano Letters 22, 8601–8607 (2022)

5. *InSbAs two-dimensional electron gases as a platform for topological superconductivity*
Christian M. Moehle*, Chung Ting Ke*, Qingzhen Wang, Candice Thomas, Di Xiao, Saurabh Karwal, Mario Lodari, Vincent van de Kerkhof, Ruben Termaat, Geoffrey C. Gardner, Giordano Scappucci, Michael J. Manfra, Srijit Goswami
Nano Letters 21, 9990-9996 (2021)

4. *Quantum Dots in an InSb Two-Dimensional Electron Gas*
Ivan Kulesh, Chung Ting Ke, Candice Thomas, Saurabh Karwal, **Christian M. Moehle**, Sara Metti, Ray Kallaher, Geoffrey C. Gardner, Michael J. Manfra, Srijit Goswami
Physical Review Applied 13, 041003 (2020)

3. *Ballistic superconductivity and tunable π-junctions in InSb quantum wells*
Chung Ting Ke*, **Christian M. Moehle***, Folkert K. de Vries, Candice Thomas, Sara Metti, Charles R. Guinn, Ray Kallaher, Mario Lodari, Giordano Scappucci, Tiantian Wang, Rosa E. Diaz, Geoffrey C. Gardner, Michael J. Manfra, Srijit Goswami
Nature Communications 10, 3764 (2019)

2. *$1/f$ and RTS noise in InGaAs nanowire MOSFETs*
C. Möhle, C.B. Zota, M. Hellenbrand, E. Lind
Microelectronic Engineering 178, 52-55 (2017)

1. *Local transport measurements in graphene on SiO_2 using Kelvin probe force microscopy*
Philip Willke, **Christian Möhle**, Anna Sinterhauf, Thomas Kotzott, Hak Ki Yu, Alec Wodtke, Martin Wenderoth
Carbon 102, 470-476 (2016)